Review article **Open Access**

Alberto Escudero*, Ana I. Becerro, Carolina Carrillo-Carrión, Nuria O. Núñez, Mikhail V. Zyuzin, Mariano Laguna, Daniel González-Mancebo, Manuel Ocaña and Wolfgang J. Parak

Rare earth based nanostructured materials: synthesis, functionalization, properties and bioimaging and biosensing applications

DOI 10.1515/nanoph-2017-0007
Received January 13, 2017; revised February 27, 2017; accepted March 16, 2017

Abstract: Rare earth based nanostructures constitute a type of functional materials widely used and studied in the recent literature. The purpose of this review is to provide a general and comprehensive overview of the current state of the art, with special focus on the commonly employed synthesis methods and functionalization strategies of rare earth based nanoparticles and on their different bioimaging and biosensing applications. The luminescent (including downconversion, upconversion and permanent luminescence) and magnetic properties of rare earth based nanoparticles, as well as their ability to absorb X-rays, will also be explained and connected with their luminescent, magnetic resonance and X-ray computed tomography bioimaging applications, respectively. This review is not only restricted to nanoparticles, and recent advances reported for in other nanostructures containing rare earths, such as metal organic frameworks and lanthanide complexes conjugated with biological structures, will also be commented on.

***Corresponding author: Alberto Escudero,** Instituto de Ciencia de Materiales de Sevilla, CSIC, Universidad de Sevilla, C. Américo Vespucio 49, E-41092, Seville, Spain; and AG Biophotonik, Fachbereich Physik, Philipps-Universität Marburg, Renthof 7, D-35037 Marburg, Germany, e-mail: alberto.escudero@csic.es
Ana I. Becerro, Nuria O. Núñez, Mariano Laguna, Daniel González-Mancebo and Manuel Ocaña: Instituto de Ciencia de Materiales de Sevilla, CSIC, Universidad de Sevilla, C. Américo Vespucio 49, E-41092 Seville, Spain
Carolina Carrillo-Carrión: CIC biomaGUNE, Paseo Miramón 182, E-20009 San Sebastian, Spain
Mikhail V. Zyuzin: AG Biophotonik, Fachbereich Physik, Philipps-Universität Marburg, Renthof 7, D-35037 Marburg, Germany
Wolfgang J. Parak: AG Biophotonik, Fachbereich Physik, Philipps-Universität Marburg, Renthof 7, D-35037 Marburg, Germany; and CIC biomaGUNE, Paseo Miramón 182, E-20009 San Sebastian, Spain

Keywords: rare earths; nanoparticles; synthesis; imaging; sensing.

1 Introduction

Rare earth (RE) elements, consisting of yttrium, scandium and the 14 elements of the lanthanide (Ln) series, have attracted huge interest in both academic research and in the industry during the last decades, due to their unique physical and chemical properties [1]. This is reflected in a growing number of applications, and in fact, they have become indispensable for a number of critical technologies, which explains their increasing demand [2, 3]. Most of these elements are not actually rare in terms of abundance, and the term "rare" should be more connected with their difficult process of extraction, because such elements tend to occur together in nature and are difficult to separate from one another [4].

Recently, the design of nanostructured materials containing RE elements, either as major components or as dopants, has paved the way for the development of new applications. In particular, nanoparticles (NPs) possess the size (ranging from 1 to 100 nm) in which most of the biomolecular interactions take place [5–7], so the incorporation of RE into NPs allows their use in many different biomedical applications, including bioimaging, biosensing, targeting, drug delivery and other therapies [8].

There are some desirable requirements that the NPs intended for biomedical applications should fulfill. Thus, uniform size, shape, composition and surface chemistry are essential [9], since these parameters may have a strong effect on their physicochemical properties [10–13]. The particle geometry specifically has been reported to play an important role in cell-material interactions, affecting cellular uptake and cell functioning [14, 15]. Moreover, *in vivo* assays normally demand controlled particle size, for example, in order to make use of the enhanced permeation

and retention effect [16], as well as high colloidal stability and low toxicity. *In vitro* applications, on the other hand, do not require such a level of requirements, especially those related with the NPs size and shape and toxicity.

RE-based NPs show some advantages when compared with other available materials used for biomedical applications. As a general trend, RE-based NPs show low toxicity and high thermal and chemical stability. In addition, when compared with other luminescent NPs, such as nanostructures functionalized with dyes and quantum dots (QDs), frequently used in bioapplications such as luminescent imaging (LI), RE-based NPs exhibit high photostability, high luminescence quantum yield and sharp emission bands [17], the latter providing more selectivity for bioassays.

Focusing on the bioimaging applications of RE-based NPs, different imaging approaches can be found in the literature, most of them based on LI and, to a lesser extent, on magnetic resonance imaging (MRI) and X-ray computed tomography (CT). The use of RE-based NPs for LI is based on the luminescent properties of Ln cations, which are included as dopants in a large variety of inorganic matrices such as oxides, fluorides, phosphates, vanadates, molybdates and wolframates. Such inorganic matrices do not necessarily have to be based on RE, although RE compounds normally facilitate the doping process, since the incorporation of the doping Ln cations with the same charge and very similar size is favored [18]. Two great groups of luminescent RE-based NPs can be established according with the selected dopant cations. On the one hand, downconversion nanoparticles (DCNPs) convert higher-energy photons into photons with lower energy (i.e. conventional Stokes luminescence) and often contain Eu^{3+}, Tb^{3+} (codoped with Ce^{3+}) and Dy^{3+}, which are excited by ultraviolet (UV) radiation and emit in the visible region, and Nd^{3+}, which is excited and emits in the near infrared (NIR) region. On the other hand, upconversion nanoparticles (UCNPs), mostly containing Er^{3+} or Tm^{3+} codoped with Yb^{3+}, are able to emit shorter wavelength light after having been excited by long wavelength radiation (i.e. anti-Stokes luminescence). Both UCNPs and Nd^{3+} doped DCNPs have attracted high research interest, since they are excited by NIR radiation, avoiding thus photodamage and background fluorescence of biological systems and enabling a higher penetration depth into biological tissues [19].

Of remarkable interest are persistent luminescent nanoparticles (PLNPs), most of them showing DC luminescence, which are able to emit light for minutes, hours or even days after ceasing the excitation irradiation. The applications of PLNPs in biomedical assays are relatively recent, and the fact that they can be excited in advance makes them of especial interest, since the irradiation of both cells and animals is avoided, which is especially favorable in case UV radiations are demanded. Silicate, aluminosilicate, germanate, gallate and gallogermanate are typical matrices for persistent luminescent materials, while transition metals ions such as Cr^{3+}, Mn^{2+}, Mn^{4+} and Ti^{4+}, main group metals ions such as Bi^{3+} and Ln cations such as Eu^{2+}, Ce^{3+}, Dy^{3+} and Pr^{3+} act as dopants, often combined with one another [20]. In this review we will focus on the latter.

The magnetic properties of some Ln cations such as Gd^{3+}, Ho^{3+} and Dy^{3+} make RE-based NPs of these cations very useful in MRI because they are able to induce additional contrast between normal and abnormal regions, which is otherwise very poor. This type of MRI contrast agents (CA) complements classical CAs available in the literature like Gd chelates or superparamagnetic iron oxide NPs (SPIONs). Likewise, the high atomic number (Z) of the Ln elements confers the RE-based NPs a high capacity to absorb X-rays and make them therefore suitable CAs for CT. CT CAs consisting of RE-based NPs show less toxicity and higher circulation times than the widely used barium and iodine-based compounds.

RE-based NPs are also used for the detection and analysis of ions and molecules of biomedical interest, such as DNA and proteins. In this case, the biosensing assays are based on the variation of the luminescent properties of the NPs in the presence of the analytes.

It should also be mentioned that one general advantage of RE-based NPs is the possibility of combination of several Ln ions in one NP, which can provide multifunctionality, as it is the case of NPs for multimodal imaging and theranostics [21, 22].

In most of the cases, a functionalization process, consisting of the attachment of functional groups to the NP surface, is demanded if the NPs are to be used in biomedical applications. This step can reduce toxicity and provide colloidal stability to the NPs [23, 24]. In addition, the reactive groups can be used as anchors for further conjugation of the NPs with different molecules of biomedical interest, such as antibodies, peptides, proteins and drugs [25].

Metal-organic framework NPs (MOF NPs or nanoMOFs) are a new class of hybrid nanomaterials consisting of inorganic building units coordinatively connected by organic building units at the nanometer level. Ln-containing luminescent MOFs have been recently the subject of much attention because of their promising applications in several fields, including biotechnology. They can either be built from Ln cations or serve as host structures, in which the Ln cations can be incorporated into the

connectivity centers or inside the pores of the MOF [26, 27]. Their highly porous and oriented structures, which allow them to accommodate many different cargoes, and their intrinsic biodegradability make them interesting materials for biomedical applications, especially for sensing and delivery [28].

This review will be focused on the properties and applications of RE-based NPs and MOFs for bioimaging (LI, MRI and CT) and biosensing, as well as on the most commonly used strategies for their synthesis and functionalization. For a deeper and more detailed description of these matters, some excellent reviews can be found in the recent literature [19, 29–40].

2 Synthesis and functionalization of RE-based nanostructures

2.1 Synthesis of RE-based DCNPs and UCNPs

Traditional synthesis methods such as solid state synthesis can be used to produce RE-based materials, but given the high temperature annealing processes that are involved, they normally yield irregular particles with broad size distribution that are thus not suitable for most bioapplications. For this reason, wet chemical methods have attracted much research attention for the synthesis of RE-based NPs for biomedical applications. Most of these strategies, based on precipitation reactions, are described below. The general requirement to obtain uniform NPs is the slow and controlled release or cations or/and anions, followed by an appropriate reaction kinetics, which in some cases can be achieved after a careful experimental optimization of all the synthesis variables [41]. This controlled release can be produced by starting from appropriate precursors that release cations or anions by hydrolysis or by thermal decomposition. Additives that form complexes with the cations, which can be further decomposed on heating thus liberating the cations in a controlled way, are also commonly used. In these cases, such additives may act as also capping and/or dispersing agents. As previously mentioned, the kinetics of the reaction has to be experimentally optimized for each reaction, which is normally achieved through a systematic analysis of the effects of the reagent concentrations, synthesis temperature, solvent composition, and nature and concentration of additives on the morphological characteristics of the precipitated particles.

The synthesis methods of RE-based NPs based on the above strategy can be divided into two general groups, according to the pressure at which the reaction takes place: reactions carried out at atmospheric pressure and hydrothermal or solvothermal methods. Some representative examples are shown in Table 1.

Table 1: Synthesis conditions for some RE-based NPs.

Composition	Solvent	Additives	Temperature (°C)	Time	Morphology	Reference
$LiYF_4:Nd^{3+}$	1-Octadecene	Oleic acid	300 (N_2)	90 min	Octahedral	[42]
α-$NaHoF_4$	1-Octadecene	Oleic acid Oleylamine	250–330 (Ar)	15–45 min	Nanopolyhedra	[13]
$NaYF_4:Yb^{3+}$, Er^{3+}, Tm^{3+}	1-Octadecene	Oleic acid TOPO	300 (Ar)	1 h	Nanoplates, nanospheres Nanoellipses	[43]
$GdPO_4$	Butylene glycol		120	1 h (MW)	Nanocubes	[44]
YF_3	Ethylene glycol	–	120	15 h	Rhombic	[45]
$Ca_5(PO_4)_3)(OH):Eu^{3+}$	Water	PAA	180	1 h (MW)	Nanospindles	[46]
$ZnGa_2O_4:Eu^{3+}$, Cr^{3+}	Ethylenediamine	–	200	48 h	Spherical	[47]
$NaGdF_4$	Water	Sodium citrate	180	24 h	Nanorods	[48]
$BaGdF_5$	Water	EDTA	180	24 h	Nanospheres	[49]
REF_3	Water/ethanol	Sodium linoleate Linoleic acid	100–200	8–10 h	Diverse morphologies	[50]
$BiPO_4:Eu^{3+}$	Ethylene glycol/glycerol	Sodium citrate	120	20 h	Nanostars	[51]
$YVO_4:Eu^{3+}:Bi^{3+}$	Ethylene glycol/water	PAA	120	5 h	Quasispheres	[52]
$BaGdF_5:Yb^{3+}$, Er^{3+}	Ethylene glycol	PEI	190	24 h	Nanospheres	[53]
GdF_3	Diethylene glycol	–	120	15 h	Quasispheres	[54]
$CePO_4:Tb^{3+}$	Water	β-Cyclodextrin	Room temperature	30 min	Nanowires	[55]

TOPO, Trioctylphosphine oxide; PAA, poly(acrylic acid); EDTA, ethylenediaminetetraacetic acid; PEI, polyethylenimine; (N_2) and (Ar) refer to the used atmosphere; MW, microwave-assisted.

2.1.1 Precipitation at atmospheric pressure

Precipitation reactions at atmospheric pressure can be carried out in water or in organic solvents such as alcohols, polyols and solvents of higher boiling point.

2.1.1.1 Aqueous solutions

Some examples of the synthesis of RE-based NPs in water at temperatures <100°C can be found in the literature. However, such strategies do not normally produce uniform NPs, except when capping or dispersing agents are added. For example, LaF_3:Eu^{3+} NPs with a size around 25 nm have been synthesized at 75°C in the presence of chitosan from aqueous $LaCl_3$, $EuCl_3$ and NH_4F solutions [56] and LaF_3:Ln^{3+} (Ln = Eu, Eu, Nd, Ho) NPs of smaller size (5–10 nm) have been obtained by precipitation at 75°C in water solutions containing ethanol, from Ln nitrates and NaF precursors using *n*-octadecyldithioposhate as additive [57]. Uniform $REPO_4$-based nanophosphors have also been synthesized in aqueous solutions. Thus, $CePO_4$:Tb^{3+} nanocrystals have been obtained at 80°C from $Ce(NO_3)_3$, $Tb(NO_3)_3$ and $NH_4H_2PO_4$ solutions in the presence of poly(ethylene glycol) (PEG) bis(carboxymethyl) ether [58]. β-Cyclodextrin has been also used as additive for the synthesis of $CePO_4$:Tb^{3+} nanowires at room temperature from $Ce(NO_3)_3$, $TbCl_3$ and NaH_2PO_4 [55]. Finally, $LaPO_4$:Ln^{3+} (Ln = Ce, Tb, Eu) NPs with sizes below 10 nm have been synthesized at 90°C from $La(NO_3)_3$ and sodium-polyphosphate ($Na_5P_3O_{10}$) precursors [59], which also act as stabilizing agents.

2.1.1.2 Organic solutions

Synthesis in high boiling point solvents

Precipitation reactions at high temperatures (200–400°C) can be carried out by using solvents of high boiling point, as octadecene, eicosene, and trioctylamine. In these cases, the reactions must be conducted in an inert atmosphere (Ar, N_2) under reflux, and capping and/or complexing agents are also usually required to obtain uniform NPs. Among them, oleic acid (OA), linoleic acid, stearic acid and their salts are widely used, since they are able to form very stable complexes with the RE [60]. Some amines (mostly oleylamine) and phosphines (trioctylphosphine oxide, TOPO) have also been employed.

Common RE salts (nitrates and chlorides) are frequently used as precursors, and methanol is sometimes employed to favor precursor dissolution. Many systems have been prepared by using this procedure, mostly Ln phosphates and different Ln fluorides. For example, $REPO_4$ (RE = La, Y, Eu, Tb and Ho) NPs with different morphology (polyhedral and wires) have been synthesized from the corresponding RE nitrates or hydroxides in an oleic acid/oleylamine/octadecene mixture at 180°C [61]. In this work, particle size and shape were found to depend on the nature of the RE cation and/or the oleic acid/oleylamine ratio. Ultra-small $LaPO_4$:Eu^{2+} NP of 3.5 nm have been also synthesized at 240°C from solutions of the RE chlorides and Na_3PO_4 in oleic acid and octadecene [62]. By far, the majority of RE-based NPs synthesized by this method consist of different fluoride phases. To mention a few, uniform ultra-small (4 nm) $KGdF_4$:Yb^{3+}, Tm^{3+} NPs [63], $LiYF_4$:Nd^{3+} NPs with an octahedral shape (24 nm length ×20 nm width) [42] (Figure 1A), $NaYF_4$:Yb^{3+}, Er^{3+} nanospheres (around 23 nm diameter) [67] and $NaLuF_4$:Gd^{3+}, Yb^{3+}, Er^{3+} nanospheres (around 27 nm diameter) [68] have been synthesized at 300°C from the corresponding RE chlorides, alkaline hydroxides and NH_4F solutions in octadecene, using oleic acid as capping agent. A slight modification of this method, basically consisting in the addition of TOPO as an additional capping agent, has been used for the synthesis of $NaYF_4$:Yb^{3+}, Er^{3+}, Tm^{3+} NPs with different morphologies (nanoplates, nanospheres and nanoellipses, all of them showing an average size of around 20 nm). In this case the concentration of the capping agents had a big influence on the final morphology of the NPs [43]. Another additional capping agent is oleylamine, which has been used for the synthesis of YF_3:Yb^{3+}, Er^{3+} nanoplates with thickness ranging from 13 to 17 nm [69] and $NaLuF_4$:Yb^{3+}, Er^{3+} nanospheres (40 nm diameter) [70]. In these two last examples, the relative amount of oleic acid/oleylamine had a strong influence in the final morphology of the NPs.

This synthesis route has been also conducted using RE oleates and stearates as RE precursors. For example, ultra-small $NaGdF_4$ NPs (3–4 nm) have been produced from sodium and Gd oleates and $N(CH_3)_4F$ in a mixture of octadecene, oleic acid and oleylamine at 220°C [71], and $NaGdF_4$:Yb^{3+}, Er^{3+} nanospheres (from 15 to 25 nm) have been synthesized from the corresponding RE oleates and NaF in octadecene and oleic acid at 320°C. The synthesis of ultra-small $BaLuF_5$:Yb^{3+}, Er^{3+} NPs with sizes below 10 nm in octadecene/oleic acid solutions at 300°C from RE stearates has also been reported [72].

Finally, RE trifluoroacetates are a special kind of RE precursors used for the synthesis of many fluoride-based NPs in organic high boiling point solvents. Their main advantage is that the trifluoroacetate anions decompose on heating at about 300°C, thus liberating the F^- anions required for solid phase formation in a controlled manner. This method is known as thermolysis and has been used for the synthesis of highly uniform RE trifluoride (REF_3)

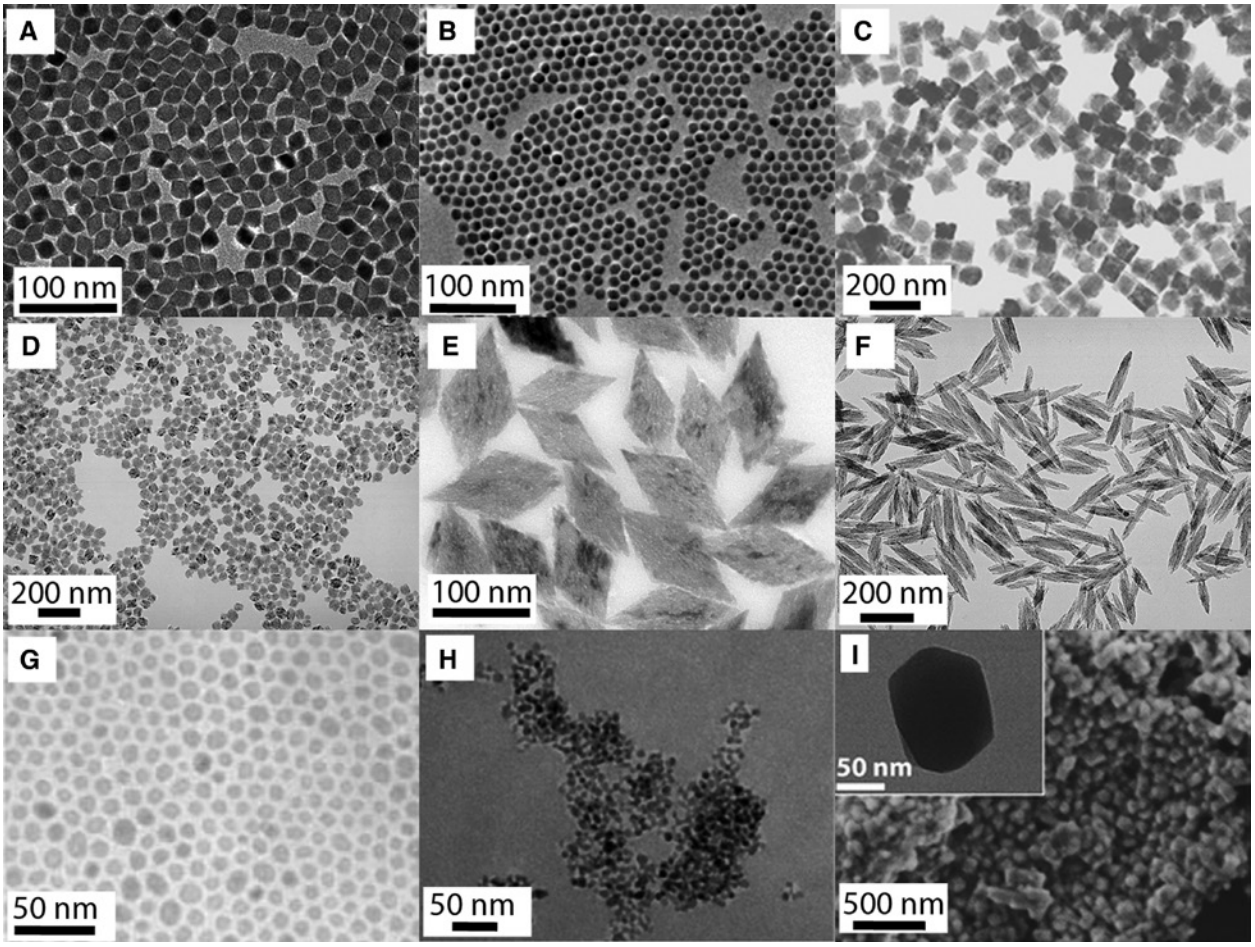

Figure 1: (A) $LiYF_4:Nd^{3+}$ NPs synthesized from RE chlorides in ODE/OA at 300°C. Taken from [42]. Reproduced with permission of The Royal Society of Chemistry. Copyright © 2016. (B) α-$NaHoF_4$ NPs synthesized from RE trifluoroacetates in ODE/OA at 330°C. Taken from [13]. Reproduced with permission of the American Chemical Society. Copyright © 2006. (C) $GdPO_4$ nanocubes synthesized from $Gd(acac)_3$ and H_3PO_4 in BG at 120°C. Taken from [44]. Reproduced with permission of the American Chemical Society. Copyright © 2013. (D) $GdVO_4:Eu^{3+}$ NPs synthesized from $Gd(NO_3)_3$ and Na_3VO_4 in an ethylene glycol/water mixture in the presence of PAA at 120°C. Taken from [64]. Reproduced with permission of The Royal Society of Chemistry. Copyright © 2013. (E) YF_3 NPs synthesized from yttrium acetylacetonate and the IL $[BMIM]BF_4$ in ethylene glycol at 120°C [45]. (F) $Ca_5(PO_4)_3)(OH):Eu^{3+}$ nanospindles synthesized through a microwave-assisted hydrothermal method at 180°C in the presence of PAA. Taken from [46]. Reproduced with permission of the American Chemical Society. Copyright © 2013. (G) $NaYF_4$ NPs synthesized through a solvothermal method in ethanol with linoleic acid and sodium linoleate as additives. Taken from [65]. Reproduced with permission of Nature Publishing Group. Copyright © 2005. (H) $ZnGa_2O_4:Eu^{3+}$, Cr^{3+} PLNPs synthesized in EDA at 200°C. Taken from [47]. Reproduced with permission of The Royal Society of Chemistry. Copyright © 2016. (I) $[(Tb_{0.914}Eu_{0.086})_2(PDA)_3(H_2O)] \cdot 2H_2O$ MOF NPs synthesized by spray-drying at 180°C. The inset depicts a TEM image of a crystal isolated from the aggregate by sonication. Taken from [66]. Reproduced with permission of John Wiley and Sons. Copyright © 2015.

and mixed RE-alkaline (A) or RE-alkaline earth (M) fluorides (mostly, with $AREF_4$ and $MREF_5$ stoichiometry) NPs. For example, triangular LaF_3 nanoplates with dimensions 2×16 nm were produced from the decomposition of lanthanum trifluoroacetate in oleic acid and octadecene at 280°C [73]. Mixtures of oleic acid and octadecene have also been employed for the synthesis of hexagonal-shaped $NaGdF_4:Yb^{3+}$, Ho^{3+} NPs (15 nm) [74] and of roughly spherical $NaYF_4:Yb^{3+}$, Er^{3+}, Tm^{3+} NPs (15–30 nm) [75] from RE and Na trifluoroacetates. Likewise, ultra-small $BaLuF_5:Yb^{3+}$, Tm^{3+} NPs (<5 nm) were obtained from lutetium trifluoroacetate and barium acetylacetonate [76]. In some cases, oleylamine was added as an additional capping agent. Thus, $NaREF_4$ (RE = Pr to Lu, and Y) NPs of different morphologies (nanopolyhedra ranging from 6 to 15 nm, nanorods of around 25×45 nm, nanoplates with dimensions of 155×76 nm and nanospheres around 20 nm) have been obtained from sodium and RE trifluoroacetates in oleic acid/oleylamine/octadecene mixtures at high temperature (250–330°C). An example of these systems is

illustrated in Figure 1B, which corresponds to $NaHoF_4$. In these cases, the Na/RE ratio, the solvent, the synthesis temperature and the reaction time had a great influence on the final morphology of the NPs [13]. An oleic acid/oleylamine/octadecene mixture was also used for the synthesis of ultra-small $BaGdF_5$:Yb^{3+}, Tm^{3+} NPs (<5 nm) from the corresponding RE and Ba trifluoroacetates at 300°C [77]. It must be mentioned that this method also works using liquid capping compounds as solvents. For example, cubic and hexagonal-like β-$NaYF_4$:Eu^{3+} NPs (from 10 to 20 nm) [78] and $NaYF_4$:Yb^{3+}, Ln^{3+} (Ln = Er, Ho and Tm) nanospheres (10 nm) [79] have been synthesized at 330–350°C from sodium and RE trifluoroacetates dissolved in TOPO, not needing any additional solvent. The Na/Y ratio was also found to play a key role in the final morphology of the NPs [78]. $NaYF_4$:Yb^{3+}, Er^{3+}, Tm^{3+} NPs (10 nm) [80] and $NaLuF_4$:Yb^{3+}, Er^{3+} nanospheres (19 nm) [81] have also been produced from the thermal decomposition of sodium and RE trifluroacetates in oleylamine at 300°C. A similar strategy has been used to obtain GdF_3:Nd^{3+} nanospheres of sizes ranging from 3 to 13 nm at 340°C [82].

Synthesis in polyols

It has to be mentioned that the use of hydrophobic organic solvents and additives gives rise to hydrophobic NPs, and further steps of functionalization are demanded in order to make them water-dispersible [83], as it will be commented on in following sections. Moreover, the toxicity that in most of the cases is shown by such solvents and additives demands in some ways the design of more environmental-friendly synthesis strategies. Among them are those using polyol (ethylene glycol, EG; butylene glycol, BG; diethylene glycol, DEG; glycerol, GLY)-based solvents whose boiling point is much higher (from 197 to 290°C) than that of water, although lower than that of the above mentioned solvents.

Typical advantages of homogeneous precipitation synthesis in glycol media are the capping abilities of the glycols [84] and their lower toxicity, when compared with other organic solvents. However, in general terms, larger NP sizes are also obtained. By using this kind of solvents, a large variety of RE-based NPs with different shapes and sizes, including fluorides, phosphates, vanadates and molybdates have been synthesized. In most cases, a controlled release of cations is involved in the synthesis process. Analogously to the aforementioned examples of synthesis at higher temperatures, the slow and controlled release of the RE cations can be achieved by selecting organic precursors of RE and/or by the use of additives, which can form stable complexes with the RE cations. RE acetylacetonates [$RE(acac)_3$] have been reported to be appropriate precursors, since they release the RE cations upon heating. Uniform $NaYF_4$:Ln^{3+} (Ln = Eu, Tb, and Yb + Er) nanospheres of around 50 nm [85] and YVO_4:Eu^{3+} nanoellipsoids of 130 × 60 nm and quasispheres of around 90 nm [86] have been obtained at 120°C from $Y(acac)_3$ and Na_3VO_4 after the optimization of the reaction kinetics, which was carried out by adjusting the viscosity and dielectric constant of the solvent (a mixture of EG and water). Similar strategy was applied for the synthesis at 120°C of YPO_4:Ln^{3+} (Ln = Eu, Ce, Tb, and Ce + Tb) NPs with lenticular shape (60 nm diameter) in EG at 120°C [87] and of $GdPO_4$:Eu^{3+}nanocubes (70 nm edge dimension) in BG (Figure 1C) [44]. In the last two examples, a microwave oven was used instead of a regular oven. This heating source has been proved to reduce the reaction times and increase the reaction yield. RE acetates have also been used as RE precursors as in the case of the synthesis of $LuPO_4$ nanospindles of 130 × 62 nm in BG at 120°C [88].

Sodium citrate is frequently used as additive for the synthesis of uniform RE-based NPs in glycol media. These anions form a citrate-Ln^{3+} complex which acts as a reservoir for the controlled release of the RE cations to the reaction medium. This procedure has been employed for the synthesis of uniform 150 nm diameter $BiPO_4$:Eu^{3+} nanostars in EG/GLY mixed solvent at 120°C [51] and of $(NaGd(MoO_4)_2)$ 70 × 35 nm nanospindles, which were synthesized in an EG/H_2O mixed solvent at 120°C [89].

Poly(acrylic acid) (PAA) has also been frequently used as a capping agent for the synthesis of RE-based NPs through the polyol method. Thus, uniform $GdVO_4$ nanocubes (Figure 1D) [64] and $LaVO_4$ [90] nanospheres have been synthesized at 120°C from $Ln(NO_3)_3$ solutions in EG/H_2O mixtures, using Na_3VO_4 as vanadate source. Interestingly, the size of the NPs could be adjusted by changing the amount of PAA added. Similarly, ultra-small $NaCeF_4$:Tb^{3+} NPs of 3.8 nm were obtained in DEG from the corresponding RE nitrate, NH_4F and PAA at 200°C [91]. Polyethylenimine (PEI) is another common additive, used for example for the synthesis of $BaGdF_5$:Yb^{3+}, Er^{3+} sphere-like NPs of around 10 nm, which were obtained from RE nitrate, $BaCl_2$, NH_4F and PEI solutions in EG at 190°C [53].

Slow release of anions has also been used to obtain RE-based NPs in polyol solutions. This is the case of the synthesis at 120°C of octahedral BiF_3:Eu^{3+} NPs in a DEG/water mixture using $NaBF_4$ as fluoride source, which liberates F^- anions after hydrolysis of the BF_4^- anion [92]. GdF_3 nanocubes have been synthesized in a similar way from gadolinium chloride and the ionic liquid (IL) [BMIM]BF_4 in DEG [54]. In this case [BMIM]BF_4 slowly releases fluoride anions by hydrolysis [93]. It is important to mention that the use of ILs has been suggested as a green alternative to the conventional organic solvents for the synthesis of

inorganic compounds [94, 95], because they are non-volatile, non-flammable and thermally stable organic salts with low melting point, and they can also act as capping agents or surfactants. Other REF_3-based NPs synthesized from ILs are EuF_3 rodlike NPs, obtained from europium acetate and the IL (2-hydroxyethyl)-trimethylammoniumtetrafluoroborate ([choline] [BF_4]) in ethyleneglycol at 120°C [96], and rhombic-like LuF_3 NPs, obtained after a solvothermal process at 150°C of ethanolic solutions containing the corresponding RE nitrates and 1-octyl-3-methylimidazolium hexafluorophosphate (OmimPF$_6$) [97].

In some cases, the controlled release of both cations and anions is required to obtain uniform NPs. For example, rhombic YF_3:Ln^{3+} (Ln = Eu, Tb) NPs (Figure 1E) [45] can be obtained at 120°C from EG solutions containing yttrium acetylacetonate and [BMIM]BF_4. Another example is the synthesis of $BaGdF_5$ nanospheres of around 40 nm using a similar procedure in GLY solutions at 120°C containing gadolinium acetylacetonate, barium chloride and [BMIM] BF_4 as precursors [98].

2.1.2 Hydro(solvo)thermal methods

Solvothermal-based methods are those carried out in closed vessels under autogenous pressure above the boiling point of the solvent [99]. They have been applied for the synthesis of many different nanomaterials [100]. RE chlorides and nitrates are normally used as precursors.

When using water as solvent (hydrothermal synthesis), in some cases, no additives are required to control particle size and shape, as in the synthesis of $NaREF_4$ (RE = Pr, Sm, Gd, Tb, Dy, Er) nanotubes, which were obtained using a two-step procedure. Firstly, $RE(OH)_3$ nanotubes of dimensions of 300 × 50 nm were synthesized after submitting at 120°C an aqueous solution of the corresponding RE nitrates at pH 14. Such $RE(OH)_3$ nanotubes were then treated at 120°C with aqueous solutions containing HF and NaF to obtain $NaREF_4$ nanotubes [101]. $CePO_4$ nanotubes were also prepared without additives after hydrothermal reaction of $Ce(NO_3)_3 \cdot 6H_2O$ and $(NH_4)_2HPO_4$ solutions at pH 1 and 180°C [102]. Likewise, $REPO_4$ (RE = La, Ce, Pr, Nd, Sm, Eu, Gd, Tb, Dy, Ho, Er, Tm, Yb, Lu, Y) nanotubes with diameters ranging from 5 to 120 nm were obtained after treatment at 150°C of aqueous basic solutions containing the corresponding RE nitrates and $NH_4H_2PO_4$ [103]. Finally, $CePO_4$:Tb^{3+} and $LaPO_4$:Eu^{3+} nanorods were also synthesized in a water/ethanol mixture at 120°C from the lanthanide chloride and H_3PO_4 [104]. In all these examples, an optimization of the reaction pH was carried out.

In most hydrothermal syntheses, however, hydrophilic additives are needed to produce uniform NPs. Among them, the most common is sodium citrate, which is able to form strong complexes with the REs [105], as previously commented. Several examples can be cited in which these complexes have been used in aqueous solutions such as the synthesis of $NaGdF_4$ nanorods (100 nm) at 180°C from solutions containing $Gd(NO_3)_3$ and NaF [48], and the synthesis of $BaGdF_5$ porous nanospheres of sizes ranging from 65 to 119 nm from solutions containing gadolinium and barium nitrate and $NaBF_4$ at 180°C in butyl amine, which was used to increase the pH [106]. Some RE phosphates have been also synthesized in this way as it is the case of YPO_4:Ln^{3+} (Ln = Tb, Eu, Dy) nanorods (60 × 35 nm), synthesized at 180°C from acid aqueous solutions of the corresponding RE chloride, sodium citrate and $Na_5P_3O_{10}$ [107], and YPO_4:Ln^{3+} (Ln = Tb, Eu) spherical-like NPs obtained after hydrothermal treatment at 180°C of basic aqueous solutions of $Y(NO_3)_3$, sodium citrate and Na_3PO_4 [108]. Other hydrophilic additives used for the hydrothermal synthesis of RE-based NPs are PEG, ethylenediaminetetraacetic acid (EDTA), PEI, PAA and polyvinylpyrrolidone (PVP). PEG has been used, for example, for the hydrothermal synthesis at 190°C of $BaLuF_5$ NPs (24 nm) from solutions containing PEG, $BaCl_2$, $Lu(NO_3)_3$ and NH_4F [109]. Likewise, $BaGdF_5$ nanospheres have been synthesized from aqueous basic solutions containing EDTA $BaCl_2$, $GdCl_3$ and $NaBF_4$ at 180°C [49]. PEI has been used for the solvothermal synthesis in EG at 200°C of $NaGdF_4$:Yb^{3+}, Ln^{3+} (Ln = Er, Tm, Ho) cubic NPs (40 nm) from the corresponding RE chloride, NH_4F and PEI [110]; $KGdF_4$:Ln^{3+} (Ln = Gd, Eu, Tb, Dy) roughly spherical NPs (25 nm) were obtained from KCl, RE chloride and NH_4F solutions in EG at 200°C [111]). Eu^{3+}-doped calcium apatite 191 × 40 nm nanospindles have been synthesized in water at 180°C from calcium nitrate, sodium phosphate monobasic and PAA at basic pH (Figure 1F) [46]. Finally, PVP has been used for the synthesis of 50 × 10 nm $GdPO_4$:Ln^{3+} (Ln = Ce + Tb, Eu, Yb + Er) nanorods by treatment at 180°C of aqueous solutions of $Gd(NO_3)_3$ and Na_2HPO_4 [112].

Organic hydrophobic additives such as linoleic or oleic acid, often in presence of sodium linoleate or oleate, are also frequently used for the solvothermal synthesis of highly uniform RE-based NPs in organic media, mostly in alcohol and in alcohol/water solutions. Typical examples are the synthesis of highly uniform REF_3 and $NaREF_4$ fluorides from the corresponding RE acetate and NaF in water/ethanol-containing linoleic acid or sodium linoleate solutions at temperatures ranging from 100 to 200°C [65]. This procedure yields rounded NPs of $NaYF_4$ (Figure 1G), YbF_3 and LaF_3 of around 4–12 nm diameter

and rice-like YF_3 NPs of 500 × 100 nm. Other RE fluoride systems synthesized following this strategy are LaF_3:Ln^{3+} (Ln = Ce/Tb and Yb/Er) and $NaLaF_4$ nanorods, obtained from the corresponding RE nitrate, NaOH, NaF and oleic acid in a water/ethanol solution treated at 190°C [113] and $NaYb_{1-x}Gd_xF_4$:Ln^{3+} (Ln = Eu^{3+}, Tb^{3+}, Ce^{3+}/Eu^{3+}, Ce^{3+}/Tb^{3+}, Ce^{3+}/Eu^{3+}/Tb^{3+}, Ho^{3+}, Er^{3+}, Tm^{3+} and Er^{3+}/Tm^{3+}) NPs obtained from the corresponding RE nitrate, NaOH and NH_4F at temperatures ranging from 130 to 230°C. In the last case the Gd content played a key role in the final morphology of the NPs, which ranged from $NaYbF_4$ nanocubes to $NaYb_{1-x}Gd_xF_4$ nanorods [114]. Round-shaped NPs for REF_3 (RE = La to Eu) and rice-like NPs for REF_3 (RE = Gd to Yb) have also been obtained at temperatures ranging from 100 to 200°C from solutions of RE nitrates in water and ethanol with sodium linoleate and linoleic acid as additives [50]. Some amines have also been employed instead of fatty acid derivatives. For example, GdF_3 nanowires (length ≤ 40 nm) were synthesized at 240°C from a solution of $Gd(NO_3)_3 \cdot xH_2O$ and HF in octylamine/ethanol [115], and rice-like YF_3 and YbF_3 NPs have been obtained from ethanol/water solutions of RE nitrates, linoleate acid, octadecylamine and NH_4HF_2 treated at 100–200°C [50]. Other RE-based phases have also been synthesized following this method. For example, YPO_4:Eu^{3+} hexagonal-like NPs of around 16 nm were obtained from the RE nitrates, NaH_2PO_4, NaOH and oleic acid in a water/ethanol solution at temperatures ranging from 100 to 140°C [116]. Likewise, $REPO_4 \cdot H_2O$ (RE = Y, La-Nd, Sm-Lu) of different morphologies (sphere-like, rod-like and polygon-like, with sizes ranging from 8 to 60 nm, depending on the RE) were synthesized from RE nitrate, NaH_2PO_4, oleic acid, and NaOH solutions in water and ethanol treated at 140°C [117]. However, the use of hydrophobic additives finally produces hydrophobic NPs, thus demanding further functionalization treatments.

The main advantages of hydrothermal methods with or without hydrophilic additives over the solvothermal method using hydrophobic additives are the final hydrophilic character of the NPs, their high level of crystallinity and the fact that in contrast to most organic solvents water is not toxic. However, these methods also presents some drawbacks such as the larger particle size that usually results in comparison with that produced by the organic solvent-based methods.

2.2 Synthesis of PLNPs

An annealing treatment at high temperatures is usually required to obtain phosphors with persistent luminescence. For this reason, most systems have been prepared by using the conventional solid-state synthesis method, which usually results in heterogeneous microparticles. Some authors have also reported the synthesis of persistent phosphors by using wet chemistry techniques followed by the appropriate annealing process, which sometimes produce particles within the nanometer size range. This is the case, for example, of $Ca_{0.2}Zn_{0.9}Mg_{0.9}Si_2O_6$:$Eu^{2+}$, Dy^{3+}, Mn^{2+} PLNPs, which were synthesized by a sol-gel route followed by calcination at 1050°C [118]. In this case, a size selection by selective centrifugation was needed to narrow the PLNPs size distribution. $Zn_{2.94}Ga_{1.96}Ge_2O_{10}$:$Cr^{3+}$, Pr^{3+} PLNPs, have been produced by a citrate sol-gel method with a subsequent calcination process [119]. Nevertheless, in general terms, such methods do not allow a fine control of the NPs morphology, yielding irregular and aggregated particles, with rather heterogeneous size which limit their potential bioapplications.

Other synthesis strategies have been employed to prepare persistent luminescent nanostructures with a higher degree of uniformity. For example, homogeneous $BaAl_2O_4$:Eu^{2+}, Dy^{3+} nanotubes have been prepared by a hydrothermal procedure in the presence of cetyl trimethylammonium bromide (CTAB) followed by annealing at 1300°C [120]. Uniform $SrAl_2O_4$:Eu^{2+}, Dy^{3+} nanotubes have also been prepared by precipitation templated by surfactant assemblies, and the subsequent high temperature (1300°C) calcination [121]. In some cases, the solvent also acts as capping agent, as it is the case of $ZnGa_2O_4$:Eu^{3+}, Cr^{3+}PLNPs synthesized in ethylenediamine (EDA) through a solvothermal method. In this case, metal acetylacetonates were dissolved in EDA and treated at 200°C, yielding relatively homogeneous ultra-small (5–7 nm) PLNPs functionalized with amino groups (Figure 1H) [47].

An interesting strategy yielding homogeneous PLNPs consists of the deposit of a persistent luminescent phosphor layer on the surface of mesoporous silica nanospheres (MSNs) by ionic impregnation, followed by calcination at high temperature. This method results in the formation of a MSNs@PLNPs composite material, as it is the case of SiO_2@$SrMgSi_2O_6$:Eu^{3+}, Dy^{3+} [122] and SiO_2@$Zn_{1.1}Ga_{1.8}Ge_{0.1}O_4Cr^{3+}$, Eu^{3+} [123] uniform nanospheres.

Physical techniques, mainly laser-based strategies, have also been reported for the preparation of PLNPs. In particular, pulsed laser ablation in liquid, which consists of focusing laser pulses on a bulk target (either a single piece or pressed powder) immersed in a liquid solution [124], has shown to be an efficient and versatile technique to produce highly pure $Sr_2MgSi_2O_7$:Eu^{2+}, Dy^{3+} [125] and relatively homogeneous $Ca_2Si_5N_8$:Eu^{2+}, Tm^{3+} [126] PLNPs.

2.3 Synthesis of RE-based metal organic frameworks

MOFs are a new class of hybrid nanomaterials consisting of inorganic building units coordinatively connected by organic building units at the nanometer level. Some of the organic ligands most frequently used are shown in Figure 2. A more extended and comprehensive list of the different organic ligands used for the synthesis of RE-based MOFs can be found in a review by Chen and Ma [27]. MOFs can either be based on RE cations or serve as host structures, in which the RE cations can be incorporated into the connectivity centers or inside the pores of the MOF. The former are conventionally synthesized by precipitation reactions from RE and organic ligand precursors in water, alcohols and other organic solvents in sealed vessels [128]. Synthesis temperatures range from room temperature to hydro(solvo)thermal conditions, and in most of the cases several days of reaction are demanded. Some examples are the synthesis of $Tb(BTB)(H_2O)\cdot 2(C_6H_{12}O)$ (BTB = 1,3,5-benzenetrisbenzoate) [129], MOFs based on different Ln with tritopic organic linkers of variable size [130] and $([Tb(BTB)(DMF)]\cdot 1.5DMF\cdot 2.5H_2O)_n$ (DMF = *N*,*N*-dimethylformamide) [131]. MOFs can also contain two different cations, as it is the case of Eu-Cu and Dy-Cu 4-pyridin-3-yl-benzoic acid, and H_2BPDC = 4,4′-biphenyldicarboxylic acid [132], respectively. Sr-Eu^{2+} imidazolate frameworks have been also reported. In this case, the RE and Sr precursors are added to a melt of the organic ligands [133].

One of the main concerns regarding the synthesis of MOFs is the large-scale homogeneous production. This is partly overcome by using microwave-assisted reactors, which allow an important reduction of the reaction times. For example, Ln-based MOFs with general formula $[RE(TTTPC)(NO_2)_2(Cl)]\cdot(H_2O)_{10}$ (RE = La, Ce, Pr, Nd, Eu, Tb, Dy

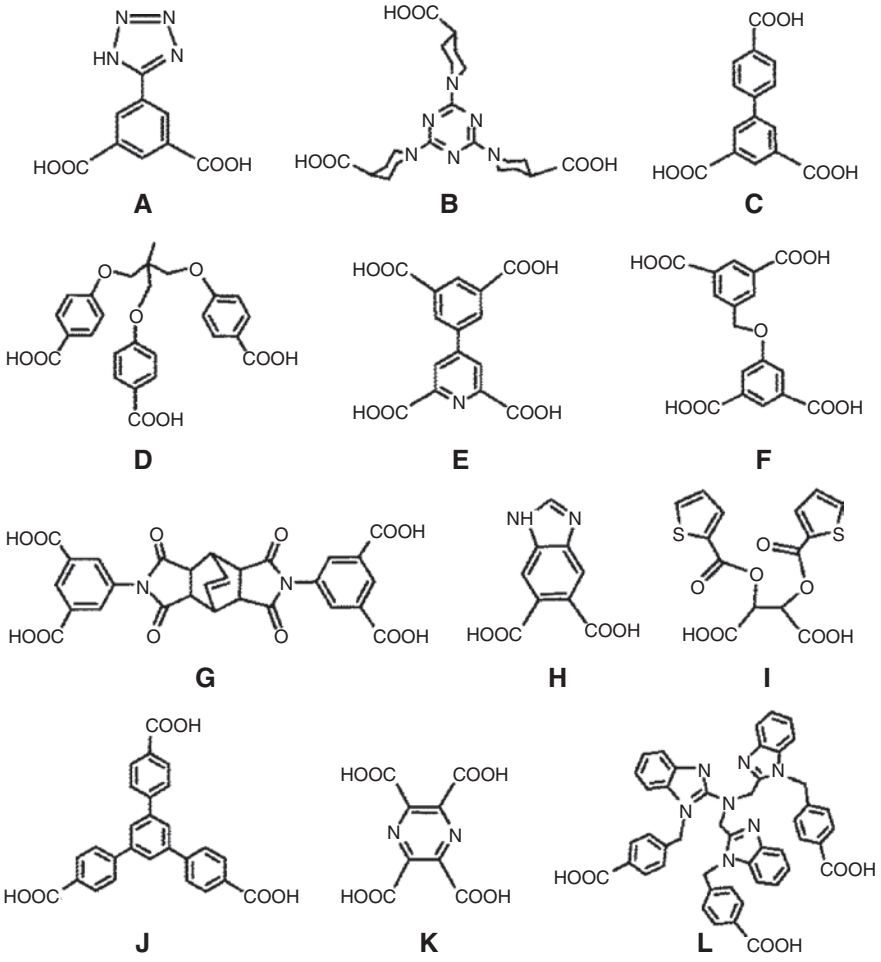

Figure 2: Some aromatic polycarboxylate ligands.
(A) H_2TIPA; (B) H_3BTPCA; (C) H_3bpt; (D) H_3L1; (E) H_4dpda; (F) H_4L2; (G) H_4L3; (H) H_2bidc; (I) H_2L4; (J) H_3btb; (K) H_4pztc; and (L) H_3L5. Taken from [127]. Reproduced with permission of The Royal Society of Chemistry. Copyright © 2016.

Ho, and Yb; and H_3TTTPC = 1,1′,1″-tris(2,4,6-trimethylbenzene-1,3,5-triyl)-tris(methylene)-tris(pyridine-4-carboxylic acid)) have been synthesized in a microwave oven at 85°C for 5 min from lanthanide nitrate and the organic ligand in a water-ethanol mixture [134].

Template-assisted MOF synthesis methods are of special interest since they allow tailoring the porous structures. Such is the case of praseodymium-adipate frameworks, which were synthesized in the presence of different dipyridyl guest molecules yielding different final structures [135].

Other alternative synthesis routes have been reported in the literature [128]. One of them is the sonochemical synthesis, which consists of the application of high-energy ultrasound to a reaction mixture. Bubbles are formed in solution, and after their collapse, local points of very high temperature and pressure can be produced [136]. Sonochemical synthesis can be carried out at room conditions, as it was reported for a series of RE-benzenetricarboxylates MOFs (RE = Ce, Tb, Y) [137]. Spray-based methods have also been reported in the literature. For example, $[(Tb_{0.914}Eu_{0.086})_2(PDA)_3(H_2O)] \cdot 2H_2O$ (PDA = 1,4-phenylenediacetic acid) metal organic framework NPs have been obtained from RE nitrate and PDA solutions in dimethylformamide and water spray-dried at 180°C (Figure 1I) [66]. Other examples are mechanochemical syntheses, which imply the mechanical breakage of intramolecular bonds, which is followed by a chemical transformation. Such reactions can be carried out at room temperature and do not necessarily require the use of organic solvents. For example, RE((BTC)(H_2O)) (RE = Sm, Gd, Tb, Dy, Y) has been synthesized from RE carbonate and benzene-1,3,5-tricarboxylic acid (H_3BTC) by ball milling during 20 min [138].

Finally, in the case of MOFs consisting of non-lanthanide elements with Ln cations accommodated in their pores, the Ln ions are introduced into the pores by immersing the non Ln-based MOFs in solutions containing the respective Ln salts. Zinc-based MOFs doped with Eu^{3+} and Tb^{3+} have been prepared by following this methodology soaking the zinc-based MOFs for 2 days with DMF solutions containing Eu^{3+} and Tb^{3+} cations [139].

2.4 Functionalization strategies

Functionalization strategies imply changes in the surface chemistry of the NP with three main objectives: (i) make them water dispersible (in case of hydrophobic NPs [140]), (ii) prevent agglomeration in biological media by introducing electrostatic and/or steric repulsions [23], and (iii) provide specific and reactive groups that can be used as anchors (mostly amino or carboxylic groups) for further conjugation of the NPs with different molecules of biomedical interest, such as antibodies, peptides, proteins and drugs [25]. Frequently used additives for the functionalization of RE-based NPs are sodium citrate, PAA, PEG and derivate, poly(allylamine hydrochloride) (PAH), poly(sodium 4-styrenesulfonate) (PSS), 1,2-distearoyl-*sn*-glycero-3-phospho-ethanolamine-*N*-[methoxy(poly-ethyleneglycol)-2000] (ammonium salt) and the amphiphilic polymer poly(isobutylene-*alt*-maleic anhydride) modified with dodecylamine (PMA) and its derivate [74, 141].

A functionalization step is mandatory for hydrophobic NPs synthesized in organic media [83]. Their hydrophobic coating can be removed by acid treatment [142] or by ultrasonication in ethanol [143], but in general terms such strategies should be avoided, since the removal of the coating does not allow or makes it difficult for further processes of conjugation and can produce aggregation. This is why in other cases the hydrophobic coating has been oxidized with the Lemieux-von Rudloff reagent, yielding water-dispersible carboxylic acid-functionalized NPs [144]. Apart from these strategies, two general types of functionalization of hydrophobic NPs are normally used, namely, ligand exchange and polymer coating. The ligand exchange consists of the replacement of the original hydrophobic NP coating by hydrophilic species such as PEG, other polymeric ligands, or citrate [67, 145]. With the polymer coating an overcoating of the hydrophobic NPs by amphiphilic polymers is carried out, mostly with PMA and its modifications. In this case the functionalization takes place via hydrophobic interactions between the hydrophobic coating of the NPs and the hydrophobic part or the polymers [67, 146–149]. Ligand exchange methods typically offer NPs with smaller hydrodynamic diameters but suffer (for most NP materials) from limited colloidal stability. Polymer coating yields NPs that are very colloidally stable but that normally show larger hydrodynamic radii [150]. A scheme of these functionalization strategies of hydrophobic NPs is shown in Figure 3.

For NPs synthesized in water or in other hydrophilic solvents, one-pot synthesis (i.e., synthesis and functionalization take place at the same time by using additives) has demonstrated to be the most convenient strategy, yielding NPs with high colloidal stability in aqueous media. An example of this is the one-pot synthesis of $NaGdF_4$@PAA NPs of spherical shape of 60 nm from gadolinium acetylacetonate, NaF and PAA solutions in an EG and water mixture treated at 120°C [151]. The one-pot strategy does not work for all systems, and other functionalization procedures carried out as a second step following the NPs synthesis have been developed. These procedures take

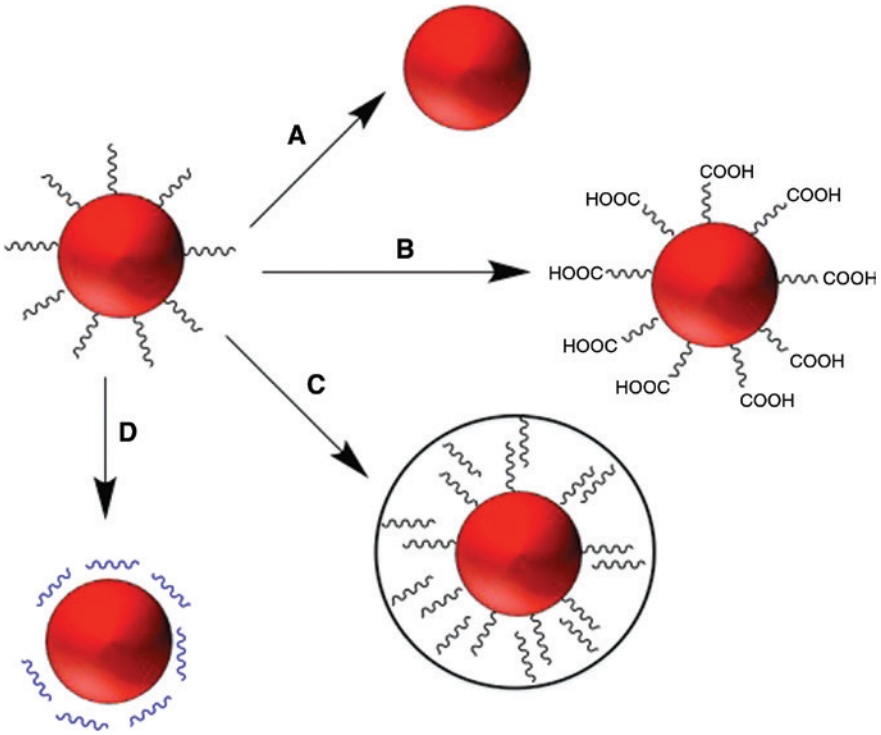

Figure 3: Scheme with some functionalization strategies used for hydrophobic NPs.
(A) Removal of the hydrophobic layer; (B) oxidation of the hydrophobic layer; (C) polymer coating; and (D) ligand exchange.

place via electrostatic or chemical interactions and have been used to functionalize GdF_3:Eu^{3+}, $GdVO_4$:Eu^{3+} and $NaGd(MoO_4)_2$:Eu^{3+} NPs with aspartic-dextran [54], amino-dextran [64] and poly(L-lysine) [89], respectively. An interesting method for the functionalization of previously synthesized NPs is the layer-by-layer (LbL) technique. This involves the subsequent deposition of polyelectrolytes with alternating charges such as PAH (positive charge), PSS (negative charge) and PAA (negative charge) onto the surface of hydrophilic NPs. In this case, the polyelectrolyte stoichiometric excess, the NP concentration, the size and degree of polymerization of the polyelectrolyte chains and the salt concentration are the variables to be adjusted in order to avoid NP agglomeration [31, 152]. This strategy has been applied to $Na(Y_{1.5}Na_{0.5})F_6$:Yb^{3+}, Er^{3+} [153] and $REVO_4$:Eu^{3+}, Bi^{3+} NPs [52]. The LbL approach has also been applied to hydrophobic $NaYF_4$:Yb^{3+}, Eu^{3+} NPs after a previous ligand exchange with citrate anions [67]. Nevertheless, the final functionalized NPs showed worse colloidal stability than those functionalized by other strategies.

Another frequently used approach for the functionalization of both hydrophilic and hydrophobic NPs is the silica encapsulation, in which a layer of amorphous silica, in most of the cases functionalized with reactive groups (i.e. organosilica), is deposited onto the NP surface [154, 155]. The encapsulation with silica shows some advantages when compared to other functionalization strategies, mostly related to its biocompatibility and the possibility of subsequent functionalization [156], as well as the high colloidal stability of the final products. The nature of the original NPs surface (hydrophilic or hydrophobic) determines the methodology to be followed, and a careful optimization of the different coating variables has to be made in order to avoid NP agglomeration. Thus, the well-known Stöber process is used to deposit a SiO_2 layer on hydrophilic NPs. This method is based on the hydrolysis of a Si alcoxide (often tetraethylorthosilicate or modifications) in ethanolic solutions, normally in the presence of ammonia [157]. For this, the NPs have to be stabilized in ethanol media with agents such as PVP of PEG-based ligands [158, 159]. This is by far the most commonly used strategy for the functionalization of PLNPs with silica that is used in bioassays [118, 119, 123, 160]. For the silica encapsulation of hydrophobic NPs, a reverse microemulsion strategy is commonly used. In this case water droplets are dispersed in a bulk oil phase, with the help of surfactants. The droplets act as nanoreactors for the confined synthesis and silica coating of nanometer-sized particles. Typical oil phases are hydrocarbons and chloroform, and CTAB, Triton X-100 and sodium decylbenzenesulfate are often used as surfactants. The selection of an appropriate surfactant is a key factor, since it determines the size of the

reverse nanodroplets and the homogeneity of the coating [161]. Hydrophobic YF_3 [162] and $NaYF_4$:Yb^{3+}, Tb^{3+} [163] NPs coated with SiO_2 are examples of this last strategy.

In addition to the amorphous silica coatings described above, mesoporous silica layers have also been deposited onto hydrophobic β-$NaYF_4$:Yb^{3+}, Er^{3+}@β-$NaGdF_4$:Yb^{3+} [164] and β-$NaYF_4$:Yb^{3+}, Er^{3+} [165] NPs by using CTAB as a secondary surfactant. This additive is not only used as a capping and phase-transfer agent but also as a structure-directing agent for the formation of mesoporous silica coatings.

3 Luminescent bioimaging

This section of the review starts with a brief, basic description of the luminescent properties of Ln-doped nanophosphors. Likewise, the strategies used to overcome the relatively low intensity of the Ln luminescence, namely, energy transfer (ET) processes, antennas and core-shell architectures are subsequently delineated, and several recent examples of the use of Ln-doped nanophosphors as bioprobes for LI are provided. Finally, given that the research on persistent luminescent nanophosphors for bioimaging has recently attracted a considerable interest, the last part of this section has been devoted to explaining the peculiarities of this type of nanophosphors, as well as their potential for use in LI.

3.1 Luminescent properties of Ln-doped nanophosphors: downconversion and upconversion luminescence

The luminescent properties of the Ln cations have their origin in their electronic configuration $[Xe]4f^n$, n = 0–14. Such 4f electronic levels are highly shielded by the $5s^25p^6$ shells and in general terms are almost not affected by the chemical environment of the Ln [166]. This means that excitation and emission bands of the luminescent Ln cations are very sharp and they appear at a similar wavelength for each Ln ion, whichever the matrix in which they are located. However, the host matrix may have an important effect on the intensity of the emissions as it will be described below.

As mentioned in Section 1, through the selection of the dopants cations, downconverting (DC) and upconverting (UC) phosphors can be obtained. Downconversion is a conventional Stokes luminescence process in which higher-energy photons are converted into lower-energy photons. Although DC luminescence is expected for most of the Ln cations, the majority of the luminescent DCNPs used for biomedical applications contain Eu^{3+}, Tb^{3+} (often codoped with Ce^{3+}) and Dy^{3+}, which produce red, green and yellow luminescence, respectively [167–171]. The large energy difference between the lowest lying excited (emissive) state and the highest sublevel of the ground multiplet of these Ln ions minimize non-radiative (NR) processes and thus make them very appropriate for luminescent applications [172]. $Nd^{3+}$is a DC ion of especial interest since it produces NIR luminescence after NIR excitation and has also been often employed. UC luminescence is a nonlinear optical process that converts two or more low-energy pump photons into a higher-energy output photon [34, 35, 173]. Several upconversion mechanisms have been reported in the literature, including excited-state absorption, energy transfer UC (ETU), photon avalanche, cooperative UC and energy migration-mediated UC. The mechanism mainly involved in the development of luminescent NPs for bioapplications is ETU, which will be described later. Readers interested in the other mechanisms may refer to more specialized reviews on this topic [31, 174, 175]. The most important Ln cations for UCNPs are Ho^{3+}, Er^{3+} and Tm^{3+}, in most cases codoped with Yb^{3+}. Typical concentrations used to optimize brightness by increasing photon absorption and minimizing luminescence quenching are ~2% mol active lanthanide cation (Eu^{3+}, Ho^{3+}, Tm^{3+}) and ~20% mol of the sensitizer cation (Yb^{3+}) [19, 80, 176].

Regarding the matrices of Ln-based luminescent materials, a wide variety of inorganic structures for both DC and UC materials have been proposed in the literature. Fluorides are used for their low phonon energy (<400 cm^{-1}), which involves a low probability of NR relaxation and therefore provides improved quantum efficiency [177, 178], while phosphates are interesting for their biocompatibility and biodegradability [179]. Other matrices based on vanadates [86, 180], oxyfluorides [92], wolframates [181–183] and molybdates [184, 185] are employed to enhance the global luminescent emission of the DC materials, as it will be detailed later.

The main disadvantage of the Ln-doped nanophosphors is the relatively low intensity of their luminescence. The most important reason of the low intensity of luminescence of Ln-doped NPs relies on the nature of the electronic transitions of the Ln^{3+} ions. Most of them involve a redistribution of electrons within the 4f sub-shell, and electric dipole selection rules forbid such transitions. Although these rules are relaxed by several mechanisms, the lanthanides luminescence is usually weak. There are other factors that may reduce the luminescence intensity

of the nanophosphors through quenching processes. Among them, two are of special relevance in Ln-doped NPs. One of them is surface quenching, which is associated with the NP surfaces. In general terms, surface defects, impurities and the presence of ligands or solvent molecules on the NP surface give rise to a decrease in the fluorescence emission of the Ln cations located near the NP surface, due to the presence of NR deexcitation processes via multiphononic processes [186–188]. In connection with this explanation, NPs size also affects the luminescent efficiency. Thus, considering that the global emission consists of the sum of contributions from the dopant ions at the surface and in the interior of the particles, and that a decrease in the NP size gives rise to an increase of the surface dopant ion concentration, a decrease in the luminescence emission is normally expected when reducing the NP size [189, 190].

The interaction of the Ln cations with the matrix itself can also lead to a decrease of the fluorescence emission. Matrices with high phonon/vibrational energies increase the probabilities of NR relaxations. This quenching is proportional to the number of vibrational quanta of the matrix that are needed to bridge the gap between the lowest emitting level and the highest non-emitting level of the lanthanide ion and decreases rapidly as the number of vibrational quanta increases [191]. As previously mentioned, fluoride-based matrices normally possess low phonon energies (<400 cm^{-1}) which leads to the low probability of NR decays, and consequently the luminescence quantum yields are usually higher than in oxide hosts and in most inorganic matrices [178, 192]. For example, $NaREF_4$ (RE = Pr to Lu and Y, in particular the β polymorph) and CaF_2 matrices are commonly employed for UCNPs, due to their higher upconversion efficiencies [81, 193–195].

Another relevant quenching mechanism is connected with the concentration of the active luminescence cations. In general, the increase in the concentration of the dopant cation results in an enhancement of the luminescence, since more emitting centers are available. However, given the similar electronic energy levels of the Ln^{3+}, ETs between the same type of Ln dopant cations can take place at a certain level of doping, and such processes may increase the possibility of NR relaxation events leading to a decrease of the emission intensity. This quenching mechanism is connected with the concentration of the active luminescence cations, and it is therefore known as concentration quenching. It is influenced by the nature of the material, the nature of the dopant and its distribution and by the NP morphology [196, 197]. An optimization of the doping level is therefore required in order to obtain the nanophosphor with the highest emission intensity.

3.2 Strategies for the enhancement of the luminescence in Ln-doped NPs

The low emission intensity of RE-based NPs constitute a serious limitation for most of the applications of these materials [198], and many different strategies have been employed in the literature to overcome this disadvantage. This is especially severe in UCNPs [199], in which quantum yield values range from 0.005% to 0.3% in $NaYF_4$:Er^{3+}, Yb^{3+} NPs [190]. The strategies used to enhance the luminescence of both DC and UCNPs can be grouped in two main groups: those that are focused on the enhancement of the absorption (energy/charge transfer) and those more connected with the minimization of the quenching effects (core-shell architectures). The most frequently used are described in this section.

3.2.1 Energy transfers in DC nanophosphors

The most used strategies to enhance the luminescence of DCNPs are based on energy and charge transfers from the matrix or from other dopants. Excitation of the doping Ln ion (acceptor or activator) via energy transfer from certain neighboring ions (donor or sensitizer) can be used to enhance the luminescence of Ln-doped NPs. This process turns out to be much more efficient than the direct excitation of the Ln electronic levels and results, therefore, in a higher luminescence. Readers may refer to the recent publication by Li et al. [200] on the development in phosphors with different emitting colors via ET for more detailed information on ET mechanisms. ET processes have been described in the literature from different types of donors to the lanthanide acceptors. Donors range from complex anion groups of the matrix such as vanadate, molybdate and wolframate groups, to individual lanthanide ions such as Ce^{3+}, Gd^{3+} and Bi^{3+}, and also interesting in this context is the well-known O^{2-} to Eu^{3+} charge transfer process, which is widely used to significantly increase the intensity of the Eu^{3+} emissions.

The ET from different anion groups of the matrix, such as vanadate [201], molybdate [202] and wolframate [203] groups, are among the most efficient ways of sensitizing the active lanthanide ions and obtaining optimum luminescence. As an example, a scheme showing the ET mechanism from the molybdate group to the Eu^{3+} ion is shown in Figure 4A. The material absorbs UV light due to an electron transfer process from the oxygen to the metal within the MO_4 group. Following the excitation in the UV region, the material undergoes a NR decay to lower energy levels of the anion group after which the energy

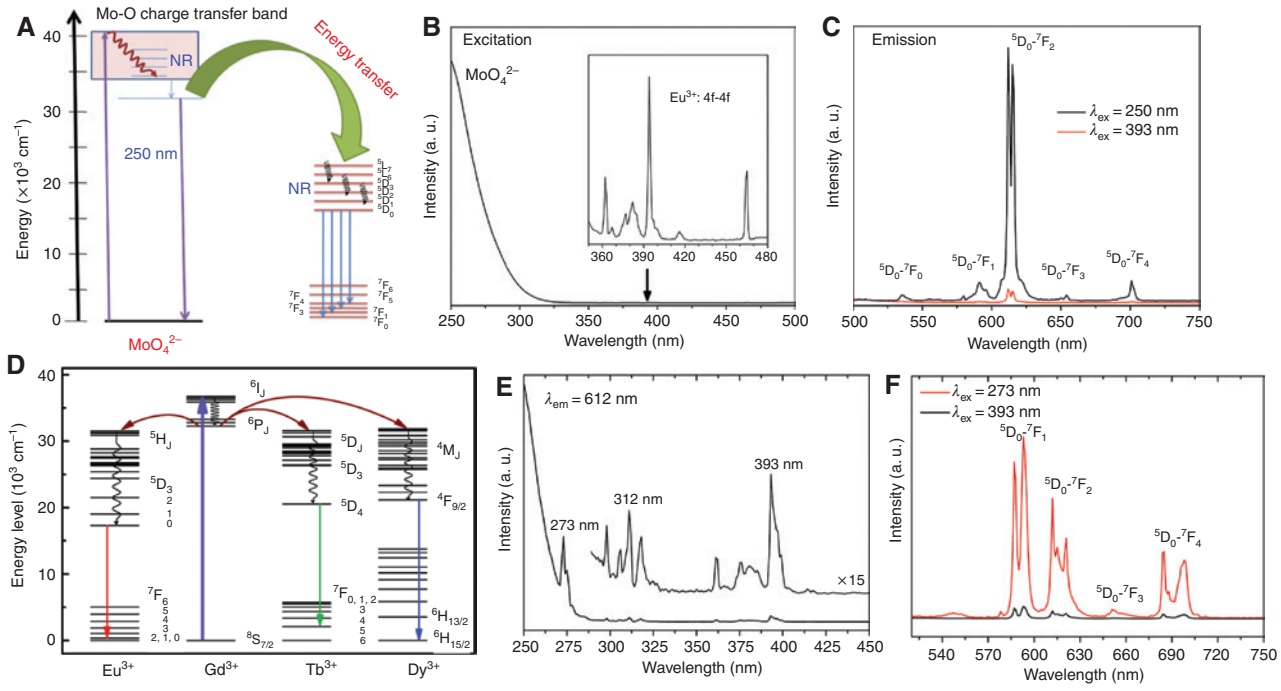

Figure 4: (A) ET mechanism between the MoO_4^{2-} and Eu^{3+} energy levels. (NR = non-radiative) Taken from [204]. Reproduced with permission of The Royal Society of Chemistry. Copyright © 2015. (B) Excitation and (C) emission spectra of Eu^{3+}-doped $NaGd(MoO_4)_2$ NPs. Adapted from [89]. Published by The Royal Society of Chemistry. (D) Schematic energy levels of Ln^{3+} ions describing the sensitized luminescence of Eu^{3+}, Tb^{3+} and Dy^{3+} ions from Gd^{3+}. The curly arrows denote multiphonon NR transitions, and the straight ones denote radiative transitions. Taken from [111]. Reproduced with permission of the American Chemical Society. Copyright © 2012. (E) Excitation and (F) emission spectra of Eu^{3+}-doped $GdPO_4$ NPs. Taken from [205]. Reproduced with permission of the American Chemical Society. Copyright © 2013.

is transferred, also non-radiatively, to the activator ions (Ln) [206]. Although a number of molybdate-based polycrystalline materials doped with Ln^{3+} ions have been reported in the literature ([204] and references therein), where the mentioned ET process has been used to enhance the Ln^{3+} emission, the study of molybdate-based NPs is really scarce. Only very recently, $NaGd(MO_4)$:Eu^{3+} NPs have been synthesized, which showed much more intense red emission after excitation through the molybdate ET band (250 nm) than after direct excitation of the Eu^{3+} ions (393 nm) (Figure 4B and C) [89]. In spite of the increased Ln emission, ET from matrix groups presents a serious disadvantage because the absorption band of vanadate, molybdate and wolframate anion groups is located in the UV region, with the consequent inconveniences for bioimaging applications, especially for *in vivo* assays. Some strategies have been proposed to overcome such limitation. It is well known that for ABO_4 crystals doped with metal ions having ns^2 electronic configurations, such as Sn^{2+}, Pb^{2+}, Sb^{3+} and Bi^{3+}, the absorption bands can be extended to the near ultraviolet region (NUV) region due to the metal-metal charge transfer in which the electrons are transferred from the ns^2 metal levels to the nd^0 ones [207]. This fact has been recently used by Escudero et al. [52] to obtain Eu, Bi-codoped $REVO_4$ (RE = Y, Gd) NPs in which the original excitation band of the vanadate anions at 275 nm shifted towards longer wavelengths (maximum of excitation 342 nm), giving rise to nanophosphors that are thus suitable for luminescent bioimaging applications.

Efficient ETs from individual Ln ions like Gd^{3+}, Ce^{3+} or Bi^{3+} to various Ln^{3+} ions have also been widely reported, as commented above. Gd^{3+} is known to absorb energy in the UV region (273 nm) of the electromagnetic spectrum, and it can efficiently transfer it to most Ln ions except Pr^{3+} and Tm^{3+}, since these two ions do not have energy levels at the same energy as the $^6P_{7/2}$ level, which is the excited state of Gd^{3+} ions [206]. Figure 4D, shows the energy levels of Eu^{3+}, Tb^{3+} and Dy^{3+} ions describing their sensitized luminescence from Gd^{3+}. Following the excitation in the UV region, the Gd^{3+} ion undergoes a NR decay to the ^6P_J energy level after which the energy is transferred, also non-radiatively, to the lanthanide ions. As in the previous cases, the excitation of the doping Ln^{3+} cation through the ET from the Gd^{3+} ion (at 273 nm) is much more efficient than the direct excitation of the Ln^{3+} electronic levels (at 393 nm for Eu^{3+}) and results in a higher luminescence [44] (Figure 4E and F). Based on the fact that Gd^{3+} ions are able

to simultaneously excite several active lanthanide ions, Becerro et al. [205] fabricated a single-phase white light emitting nanophosphor consisting in triply doped Eu^{3+}, Tb^{3+}, Dy^{3+}:$GdPO_4$ NPs. Finally, it is important to point out that Gd^{3+} ions show an added value due to their paramagnetic nature, which makes Gd^{3+}-bearing nanomaterials adequate bifunctional agents to be used as both magnetic and luminescent bioprobes [98], as will be described later in this review.

The Ce^{3+} ion is also an excellent donor due to its allowed *f-d* absorption and its broad emission band which overlaps with several Ln^{3+} as well as Mn^{2+} excitation bands, resulting in very efficient ET processes. Wang et al. [208] synthesized well-crystallized CeF_3:Tb^{3+} and CeF_3:Tb^{3+}@LaF_3 (core-shell) spherical NPs ranging from 7 to 11 nm, which showed an intense green emission after excitation at 254 nm due to the effective $Ce^{3+} \rightarrow Tb^{3+}$ ET. To confirm the ET process from Ce^{3+} to Tb^{3+}, the lifetimes of Ce^{3+} in the colloidal solution of $Ce_{1-x}Tb_xF_3$ ($x = 0-0.20$) NPs were measured. The Ce^{3+} lifetime decreased with increasing the Tb^{3+} concentrations, which indicated that an ET from Ce^{3+} to Tb^{3+} occurred in the CeF_3:Tb^{3+} NPs. The $Ce^{3+} \rightarrow Ln^{3+}$ ET has been mainly used to fabricate single-phase white light emitting LEDs [205, 209–211].

Bi^{3+} is also a common sensitizer, and there is a vast literature on Eu^{3+} red luminescence enhancement via ET from Bi^{3+} in a variety of hosts, although the nanostructuration of such materials is still not reported ([212–215] and references therein).

Finally, it is worth mentioning another interesting way of enhancing the emission intensity in lanthanides and more specifically in Eu^{3+}-activated systems. Since Eu^{3+} has a $4f^6$ configuration, it needs to gain one more electron to achieve the half-filled $4f^7$ configuration, which is relatively stable compared to partially filled configurations. When Eu^{3+} is linked to the O^{2-} ligand, there is a chance of electron transfer from the fully occupied 2*p* orbital of the O^{2-} ion to the partially filled 4f orbitals of Eu^{3+} to form Eu^{2+}-O^- (simply Eu-O). During this process, there is a broad absorption of energy in the UV range between 240 nm and 270 nm that can then be non-radiatively transferred into the Eu^{3+} energy levels. The corresponding band in the excitation spectrum is known as the Eu-O charge transfer band (CTB), and the position of this band changes depending on the particle size of the host and the environment of Eu^{3+} ions [216]. Indirect Eu^{3+} excitation through the Eu-O CTB results in much higher luminescence intensity than the direct Eu^{3+} excitation. For example, Rodríguez-Liviano et al. [87] synthesized Eu^{3+}-doped YPO_4 lenticular NPs that showed, as observed in Figure 5, a considerably higher

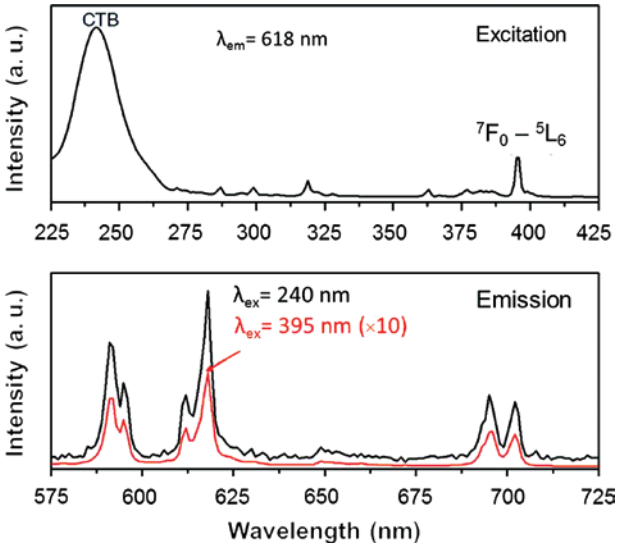

Figure 5: Excitation (top) and emission (bottom) spectra obtained for the $Eu_{0.25}Y_{0.75}PO_4$ nanophosphor.
Taken with modifications from [87]. Reproduced with permission of the American Chemical Society. Copyright © 2012.

Eu^{3+} emission intensity after excitation through the CTB at 240 nm band than by direct excitation of the Eu^{3+} electronic levels at 395 nm. However, unfortunately up to now no strategies for the shifting of the excitation of CTB toward the visible range have been reported in the literature.

3.2.2 Energy transfers in UC phosphors

The use of a sensitizer ion which allows energy transfer (ETU) to the active UC cations is required for the development of UC nanophosphors. The most used sensitizer is Yb^{3+}, which has a large absorption cross section at around 980 nm and is able to transfer the infrared absorbed energy to Er^{3+}, Ho^{3+} and Tm^{3+}, the most commonly used Ln cations in UCNPs. A schematic representation of such ET processes for UC materials is shown in Figure 6. Under excitation at 980 nm, an electron of Yb^{3+} is excited from the $^2F_{7/2}$ to the $^2F_{5/2}$ level, and the energy is transferred to the Er^{3+}, Tm^{3+} or Ho^{3+} cations, which are able to emit visible and NIR light of different wavelengths [218]. The introduction of Nd^{3+} as an extra cation permits the excitation of the UCNPs at larger wavelengths, and thus minimizes the overheating of the samples and improves the penetration depth, since this Ln absorbs NIR light at 800 nm, a region where the absorbance of biomolecules is minimized [219]. After absorbing NIR light, an ET from Nd^{3+} to Yb^{3+} takes place, and finally

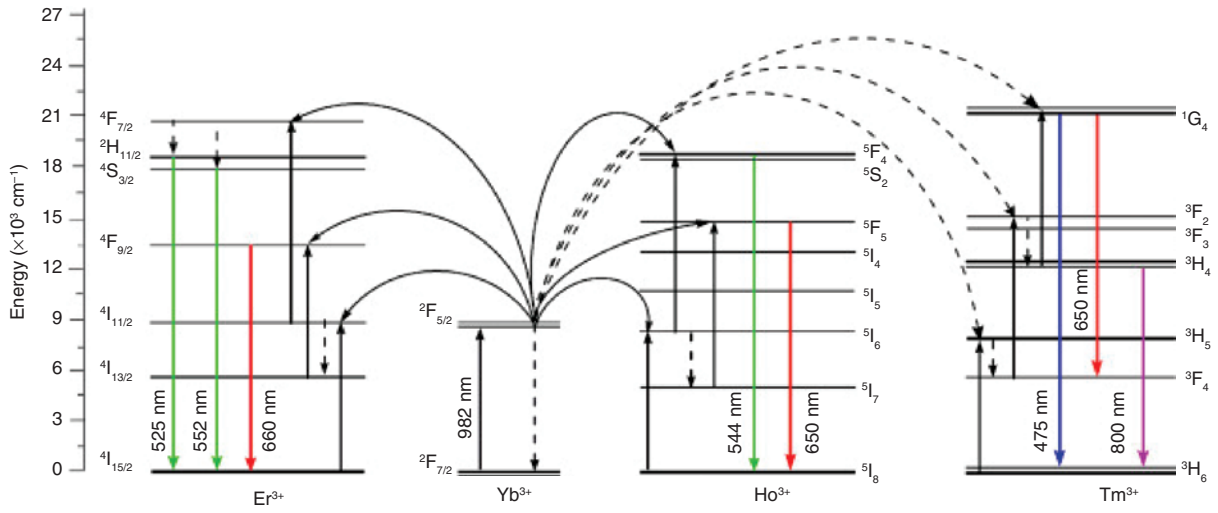

Figure 6: Energy diagrams of Yb^{3+}, Er^{3+}, Ho^{3+}, and Tm^{3+} and ETs involved in their UC luminescence.
Taken from [217]. Reproduced with permission of Elsevier. Copyright © 2016.

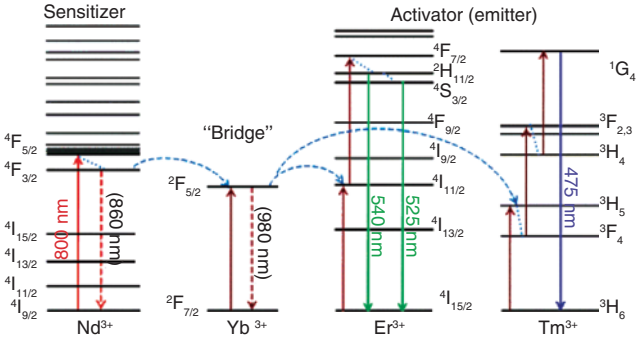

Figure 7: Upconversion process of $Nd^{3+} \rightarrow Yb^{3+} \rightarrow Er^{3+}(Tm^{3+})$ tridopants system with 800 nm excitation.
Taken from [220]. Reproduced with permission of John Wiley and Sons. Copyright © 2013.

the energy is transferred to the active emitter Ln cations ($Nd^{3+} \rightarrow Yb^{3+} \rightarrow$ active emitter), as illustrated in Figure 7 [221–224]. To minimize quenching effects, low concentrations of Nd^{3+} are used (<1%), and this cation is physically separated from the emitters by designing core-shell structures, as described later on.

3.2.3 Antenna effects

A common strategy used to enhance the luminescence in Ln-doped NPs and in Ln-based MOFs is the antenna effect. It consists of the absorption of light by a fluorophore attached to the luminescent nanostructure, which is transferred to the emitting Ln cations and results in an increase and spectral broadening of the absorption [26]. This strategy has been used for both DCNPs and UCNPs.

For example, the 3,4,3-LI(1,2-HOPO) dye attached to $NaGdF_4$:Eu^{3+} NPs is able to absorb UV light and transfer it to the Eu^{3+} emitting cations, resulting in an enhancement of their luminescence [225]. A similar strategy was used for LaF_3:Tb^{3+} NPs coated with different photosensitizing ligands, resulting in ultra-bright NPs that can be excited at 337 nm [226]. Antennas are especially relevant

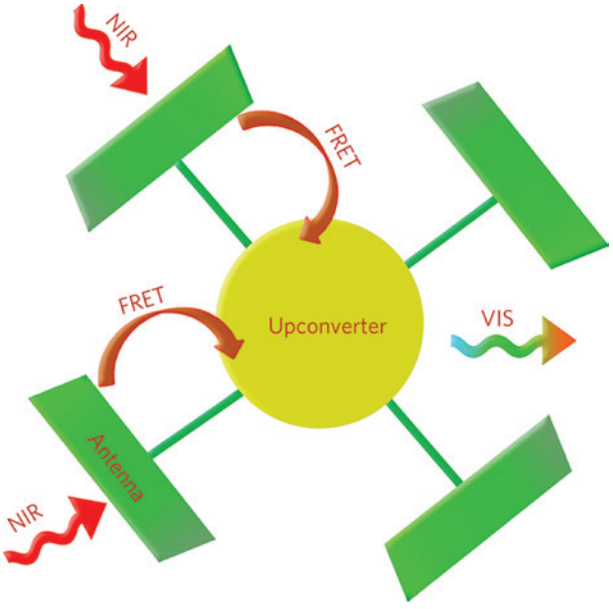

Figure 8: Schematic illustration of a dye-sensitized UCNP. The "antenna" (organic dye) absorbs NIR light and transfers it to the NP core, where upconversion emission occurs.
A detailed description of the FRET process will be given in Section 6.
Taken from [227]. Reproduced with permission of Nature Publishing Group. Copyright © 2012.

in the case of UCNPs, which can be conjugated with NIR organic dyes, as it is schematized in Figure 8. In this case, the organic infrared dyes transfer the energy to the Ln sensitizer cation (usually, Yb^{3+}). β-$NaYF_4$:Yb^{3+}, Er^{3+} NPs conjugated with a modified cyanine dye, IR-806, were reported to show an increase of 3300 times of the upconversion emission luminescence, when compared with the non-dye sensitized NPs [227]. Higher emission intensity can even be obtained by optimizing the ETs from the dyes to the Nd^{3+} and Yb^{3+} sensitizer cations with an energy-cascade mechanism, in which the dye, the sensitizers, and their location within the NP (shell, interface or core) are optimized, as it is the case of $NaYbF_4$:Tm^{3+}@$NaYF_4$:Nd^{3+} NPs conjugated with the dye IR-808. In this case, the proposed ET scheme is dye →Nd^{3+} (in the shell) →Yb^{3+} (in the core) →Tm^{3+} (in the core), the final upconverting luminescence being produced via the classical ETU mechanism [228].

In the case of MOFs, the fluorophores can be part of the MOF structure, as it is the case of benzodinitrile-based MOF [229], or can be introduced as a guest, as in carboxylate-based Ln MOF loaded with *trans*-4-styryl-1-methylpyridiniumiodide and methylene blue [230].

3.2.4 Core-shell architectures

Core-shell architectures are used to minimize the quenching by physically separating the surface defects and the surface-associated ligands from the Ln emitters. The core/shell strategy is especially relevant for UCNPs. A summary of some core-shell structures is shown in Figure 9A–D. Ln-doped NPs can be coated with a layer of an amorphous material, mostly silica-based (Figure 9B), which is a common procedure not only for functionalization but also to reduce surface quenching effects [155, 232]. A second core-shell architecture is that obtained using an inert shell of the same material as that of the core ($NaGdF_4$:Nd^{3+}@$NaGdF_4$ [233] and $NaGdF_4$:Er^{3+}, Yb^{3+}@$NaGdF_4$ [234]) (Figure 9C). The inert shell can also be fabricated with a material different to that of the core but showing similar lattice parameters ($NaEuF_4$@$NaGdF_4$ [235] and $NaYF_4$:Tm^{3+}@CaF_2 [236]). Finally, the shell can also be doped with the sensitizer cation ($KMnF_3$:Yb^{3+}, Er^{3+}@$KMnF_3$:Yb^{3+} [237]), which is then called an "active shell" (Figure 9D). This last strategy gives rise to even better results in terms of emitted luminescence. The spatial distributions and the local relative concentrations of the dopants within both the NPs core and shell have also been demonstrated to play a key role in the quenching of the luminescence of the UCNPs. Such variables can also be optimized by using strategies such as the LbL doping, as it is the case of homogeneously doped core-shell $NaGdF_4$:Yb^{3+}, Tm^{3+}@$NaGdF_4$:Ln (Ln = Tb^{3+}, Eu^{3+}) NPs, showing multicolor emission with a 20%–30% improvement in their luminescence when compared to their heterogeneously doped counterpart [238]. In some cases, the appropriate selection of the core and shell can provide nanophosphors with both UC and NIR to NIR DC luminescence, as it is the case of $NaGdF_4$:Yb^{3+}, Er^{3+}, Nd^{3+}@$NaGdF_4$:Nd^{3+} NPs [239] and other analogous core-shell structures [240, 241].

The coating with silica or silica-based materials (Figure 9E) is also a common procedure not only for functionalization but also to reduce surface quenching effects [155, 232]. Details on the silica coating were already commented on in Section 2.4. Finally, plasmonic materials such as gold and silver can also be used as coating materials providing the Ln-doped NPs with plasmonic properties and enhanced luminescence. This is attributed to the influence of the plasmonic electric fields on the local electric field (dipole moment), which can change the crystal field around the sensitizer and activator ions [242–246]. Examples of such core-shell architectures are

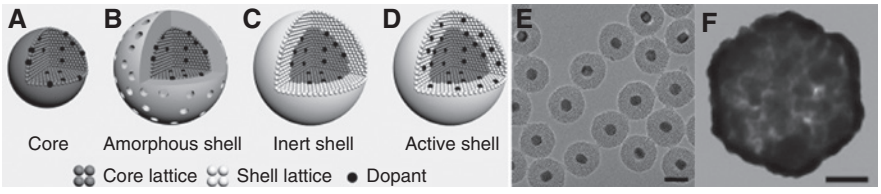

Figure 9: Different strategies to enhance the luminescence of UCNPs: Schematic illustration of a dye-sensitized UCNP: (A) Lanthanide-doped core NP. (B) Amorphous shell coating. (C) Inert crystalline shell coating. (D) Active-shell design with sensitizers or activators doped in the shell layer. Taken from [199]. Reproduced with permission of John Wiley and Sons. Copyright © 2014. (E) Porous silica coating on $NaYF_4$:Yb^{3+}, Er^{3+}@$NaGdF_4$:Yb^{3+} NPs. Bar = 50 nm. Taken from [164]. Reproduced with permission of John Wiley and Sons. Copyright © 2013. (F) $NaYF_4$:Yb^{3+}, Tm^{3+} nanocrystals coated with a Au nanoshell. Bar = 50 nm. Taken from [231]. Reproduced with permission of John Wiley and Sons. Copyright © 2010.

$NaYF_4$:Yb^{3+}, Er^{3+}, Tm^{3+}@Au [247], $NaYF_4$:Yb^{3+}, Tm^{3+}@Au (Figure 9F) [231], $NaYF_4$:Yb^{3+}, Tm^{3+} NPs decorated with Au nanorods [248], $NaScF_4$:Yb^{3+}, Eu^{3+}, Gd^{3+}@Au [249], $NaYF_4$:Yb^{3+}, Er^{3+}/Tm^{3+}@Au/Ag [250] and $NaYF_4$:Yb^{3+}, Er^{3+}@Ag [251]. In other cases, the plasmonic NP is coated with the luminescent material, as it has been reported for Au@$GdVO_4$:Eu^{3+} NPs [252]. For upconverting materials, this strategy has been demonstrated to have a positive effect on the UC luminescence [253]. Core-shell nanostructures with a combination of different shell materials have also been reported, as it is the case of $NaYF_4$@SiO_2@Au [254], $NaGdF_4$:Yb^{3+}/Er^{3+}@$NaGdF_4$@Ag [255] and $NaYF_4$:Yb, Er@$NaYF_4$@SiO_2@Au [256].

3.3 Downconverting nanophosphors for luminescent bioimaging

Two different types of DC luminescent bioprobes based on Ln ions can be distinguished, those excited by UV radiation and emitting visible light (Ln = Eu^{3+}, Tb^{3+}, Dy^{3+}) and those doped with Nd^{3+}, which are excited and emit in the NIR region. The number of studies reporting the use of visible emitting DCNPs for luminescent bioimaging is relatively low in the literature when compared with those related to UCNPs, because the UV radiation required for the excitation can be harmful for the cells and also produces a strong self-fluorescence. Nevertheless, NUV and visible excitable $REVO_4$:Eu^{3+}, Bi^{3+} NPs have been recently used for *in vitro* luminescent bioimaging assessments. In this case, the codoping with Bi^{3+} shifts the original absorption band of the VO_4^{3-} anions (originally centered at 275 nm) toward the visible, with a maximum around 342 nm. These NPs can be excited with a fluorescence microscope (around 340 nm) or with a confocal laser scanning microscope (cLSM) at 405 nm [52] (Figure 10).

NIR to NIR emitting NPs based on Nd^{3+} overcome most of the limitations of the UV excited DCNPs and currently attract wide research interest. As mentioned above, excitation and emissions in the NIR are of particular interest, since they are located in the biological windows in which the absorption and self-fluorescence of many biological tissues are avoided [257]. Moreover, deeper penetration depth into biological tissues, better image contrast and reduced phototoxicity and photobleaching are observed [258]. For example, $NaGdF_4$:Nd^{3+}@$NaGdF_4$ NPs have been used for both *in vitro* and *in vivo* luminescent bioimaging applications (Figure 11) [233], $LiYF_4$:Nd^{3+} NPs have been employed for *in vivo* imaging of the lymphatic and blood vessel systems of mice [42], and ultra-small $NdVO_4$ NPs have been proposed for both *in vivo* imaging and photothermal therapy applications [259].

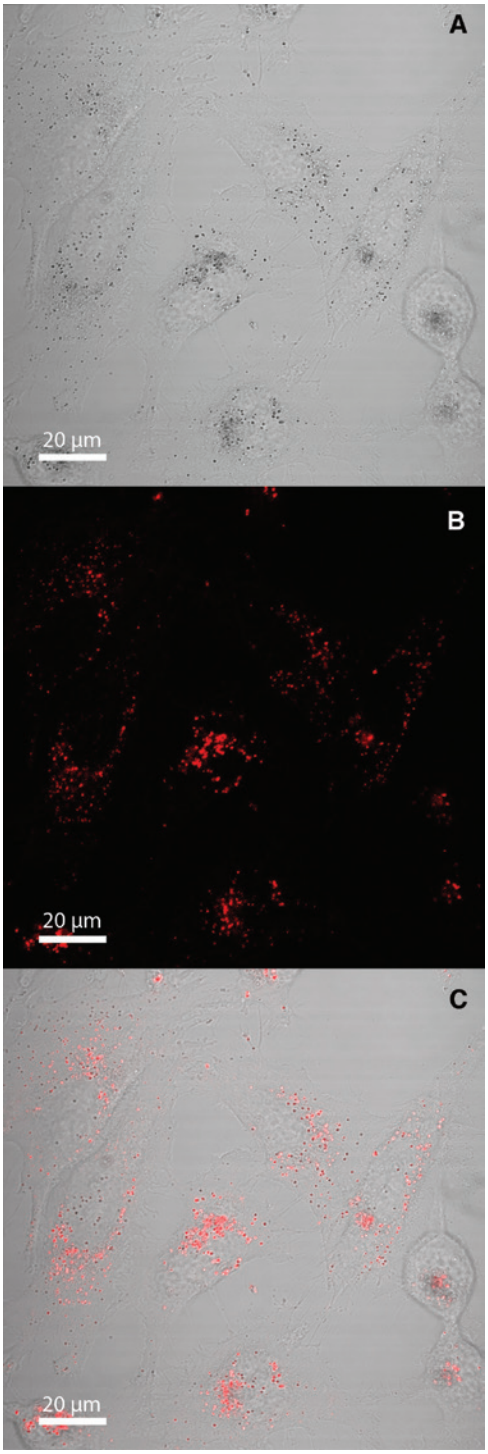

Figure 10: Confocal microscopy images of HeLa cells incubated with YVO_4:Eu^{3+}, Bi^{3+} NPs for 24 h.
(A) Transmission channel, (B) fluorescence channel (λ_{exc} = 405 nm, λ_{em} > 600 nm), (C) merged image. Taken from [52]. Published by The Royal Society of Chemistry.

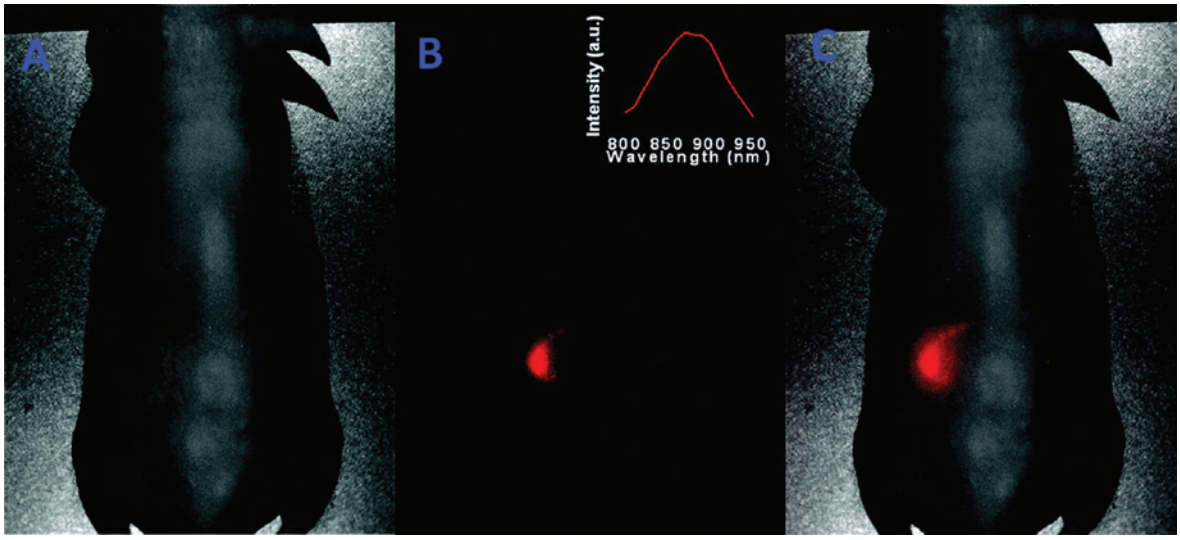

Figure 11: *In vivo* whole-body image of a nude mouse subcutaneously injected with NIR to NIR downconversion $NaGdF_4:Nd^{3+}@NaGdF_4$ nanocrystals: (A) bright field image, (B) PL image, and (C) superimposed image. Inset in panel B is the spectra of the NIR PL signals with a background taken from the injection site and noninjected area.
Taken from [233]. Reproduced with permission of American Chemical Society. Copyright © 2012.

3.4 Upconverting nanophosphors for luminescent bioimaging

UCNPs are extensively used in the literature for luminescent bioimaging due to the reasons given above. Thus, UCNPs, in many cases based on the $NaREF_4$ and REF_3 (RE = Y, La, Lu, Gd) phases codoped with Er^{3+}/Yb^{3+} and Tm^{3+}/Yb^{3+}, often silica-coated, have been used to *in vitro* image cells [260–262]. The appropriate functionalization of the NP surface and the introduction of targeting molecules such as folic acid, some peptides, specific antibodies and growth factors permits in some cases a cellular targeting imaging [263–265]. *In vivo* luminescent bioimaging of bacteria [266, 267], small animals (mostly mice) [268, 269] and plants [262, 270] with UCNPs has also been widely reported in the literature. Different processes of biomedical interest can be also studied *in vivo* by using UCNPs, as it is the case of the biodistribution of the NPs [271] and targeting [272–275].

UC NIR emission from Tm^{3+}/Yb^{3+} codoped UCNPs provide extra sensibility and penetration depth since both the excitation (980 nm) and at least one emission (800 nm) are in the NIR I window. *In vivo* images of small animals have been obtained with different $NaREF_4:Yb^{3+}$, Tm^{3+} UCNPs [276–278].

The use of both of Nd^{3+} and Yb^{3+} as sensitizers allows the *in vivo* imaging with two different possible excitations (Figure 12) [223]. For example, β-$NaGdF_4:Nd^{3+}@NaGdF_4:Tm^{3+}$, Yb^{3+} NPs have been used for *in vitro*

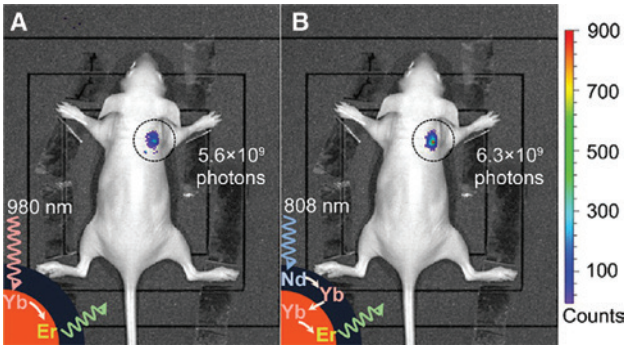

Figure 12: *In vivo* UC imaging of a nude mouse subcutaneously injected with $NaGdF_4:Yb, Er@NaGdF_4:Nd, Yb$ NPs.
The images were obtained with 980 nm laser (A) and 808 nm laser (B) irradiation. Taken from [223]. Reproduced with permission of American Chemical Society. Copyright © 2013.

two-modal imaging techniques and UC and NIR to NIR DC imaging of biological tissues [240], and peptide-functionalized $NaGdF_4:Yb^{3+}$, $Tm^{3+}@NaGdF_4:Nd^{3+}$ NPs with targeting moieties have also been used *in vivo* for both the UC and NIR to NIR DC imaging of cancer cells [241].

3.5 Persistent luminescent nanophosphors

3.5.1 Luminescent properties

Persistent luminescent materials are able to emit light for minutes, hours or even days after ceasing the excitation

irradiation. In some cases, they can be excited again to recover their luminescence, which has important implications in luminescent bioimaging. In general, such materials are based on an inorganic matrix doped with an activator metal, in which special traps or defects are formed. After excitation, charged carriers (i.e. electrons or holes) are promoted to excited states, and later they are captured in the trapping or metastable states, from where transitions to lower energy states (i.e. relaxation) are forbidden. Once in a trap, the carriers can be slowly released (i.e. escape from the traps) in a process that can be optimized and controlled, finally yielding the long-lasting luminescence [279, 280]. Traps are normally associated with defects in the structure, which can be intrinsic to the material or intentionally produced, after treatments at high temperature, by bombarding the material with electron beams, high-energy rays, nuclear particles or high-intensity lasers, or after the introduction of impurities or dopants. The nature, concentration, and depth of the traps can be characterized and optimized. For some persistent luminescent materials, Ln cations play the role of activators. Depending on the proposed mechanism, they play an active role in the persistent luminescent process (i.e. they participate in the mechanism with changes in their number of oxidation), or they just emit light through a controlled and slow ET from the host material [281, 282]. The most common matrices used for persistent luminescent materials are based on silicate, aluminate, gallogermanate and gallates [47, 118, 119, 123, 283, 284].

Some proposed mechanisms of persistent luminescence are shown in Figure 13. The hole model mechanism (Figure 13A) was proposed for $SrAl_2O_4$:Eu^{2+}, Dy^{3+}. After the excitation of Eu^{2+}, a hole is formed, and it is subsequently transferred to the valence band (VB), later to Dy^{3+}, then back to the VB and finally to Eu^{+}, which is oxidized to Eu^{2+} and then emits light [281]. The electron mechanism (Figure 13B) suggested for $CaAl_2O_4$:Eu^{2+}, Dy^{3+} implies an excitation of an electron from the matrix from the VB to traps of unspecified origin. After relaxation, the energy is transferred to Eu^{2+}, which then emits light. In this case, codoping with RE^{3+} cations is supposed to increase the number of traps in the matrix [282]. The energy band engineering model (Figure 13C), used to describe the PL in aluminate and silicate compounds, suggests an excitation of Eu^{2+} and a subsequent electron transfer to the conduction band (CB), codoping RE^{3+} cations, back to the CB and a final return to the Eu^{3+}, which is reduced to Eu^{2+} and finally emits light [285]. In $Ca_{0.2}Zn_{0.9}Mg_{0.9}Si_2O_6$:$Eu^{2+}$, Mn^{2+}, Dy^{3+} NPs, Ln cations have been suggested to act as

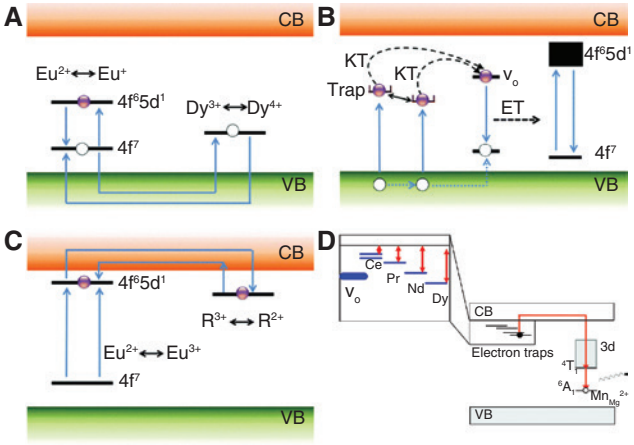

Figure 13: Proposed mechanism for some persistent luminescent materials.
(A) Hole model: Afterglow mechanism proposed by Yamamoto et al. for $SrAl_2O_4$:Eu^{2+}, Dy^{3+} [281]. (B) Electron model: afterglow mechanism proposed by Aitasalo et al. for $CaAl_2O_4$:Eu^{2+}, Dy^{3+} [282]. KT represents a thermally assisted transition. (C) Persistent phosphorescence mechanism proposed by Dorenbos et al. for aluminate and silicate compounds [285]. Images A to C have been taken from [257]. Reproduced with permission of The Royal Society of Chemistry. Copyright © 2016. (D) Schematic energy level diagram of Mn^{2+} and Ln^{3+} in $Ca_{0.2}Zn_{0.9}Mg_{0.9}Si_2O_6$ PLNPs. The main hole traps are Mn^{2+} ions in the Mg^{2+} site, while electrons are trapped by oxygen vacancies (V_o) and Ln^{3+} ions. Taken from [283]. Reproduced with permission of the American Chemical Society. Copyright © 2011.

electron traps [286], Mn being the emitter. During irradiation, holes are mainly trapped by Mn^{2+} ions giving Mn^{3+}, while electrons are trapped by oxygen vacancies and Ln^{3+} ions. Upon thermal activation, electrons are released from their traps and captured by Mn^{3+}, giving rise to the Mn^{2+} emission (Figure 13D) [283]. However, it should be taken into account that there is no universal mechanism that explains the persistent luminescence and this is still an open topic in the scientific community [257, 283, 287].

Eu^{2+} is the lanthanide cation most commonly used for persistent luminescence [288]. Its emission can be tuned from yellow to red by adjusting its chemical environment, since the electronic transitions of these cations are not *f-f* and are thus strongly affected by the crystal field [166]. Most of the time, UV radiation is required as excitation source, but some nitride- and sulfide-based phosphors can be excited with visible light [289, 290]. Eu^{2+} is often accompanied by trivalent Ln cations such as Dy^{3+} and Nd^{3+}, which, as previously mentioned, induce more defects in the host structure

and thus enhance the final luminescence [291]. Ce^{3+} is also frequently used as activator, mostly in aluminate-based matrices such as $CaAl_2Si_2O_8$ [292] and $Sr_3Al_2O_5Cl_2$ [293]. Examples of materials based on other Ln such as Eu^{3+}, Sm^{3+}, Pr^{3+}, Nd^{3+}, Tb^{3+}, Dy^{3+} Tm^{3+}, Yb^{2+} and Yb^{3+} are not so abundant in the literature, although because of their interesting properties they deserve to be mentioned. Thus, some RE-based persistent luminescent materials able to emit NIR radiation have been recently developed, either through DC ($Gd_2O_2CO_3$:Yb^{3+} [294], Sr_2SnO_4:Nd^{3+} [295] and some gallates, germanates and gallo-germanate host materials doped with Nd^{3+} [296] and Yb^{3+} [297, 298]) or UC (gallo-germanate phosphors doped with Cr^{3+}, Yb^{3+} and Er^{3+} [299]) processes. However, NPs have been obtained only for the $Gd_2O_2CO_3$:Yb^{3+} case.

Finally, it should me mentioned that not only RE cations are used to produce persistent luminescent materials but also transition metal cations such as Cr^{3+}, Mn^{2+}, Mn^{4+}, Ti^{4+} and main group elements such as Bi^{3+} have been also reported as activators [20].

3.5.2 Luminescent bioimaging with PLNPs

In vivo imaging of small animals has been carried out with RE-based PLNPs. Variables to be taken into account are the time during which the luminescence is observed after stopping the excitation and the possibility of reactivation to restore the persistent luminescence signal.

Different observation times have been reported in the literature. For example, $Ca_{0.2}Zn_{0.9}Mg_{0.9}Si_2O_6$:$Eu^{2+}$, Mn^{2+}, Pr^{3+} NPs, previously irradiated with UV light (254 nm), can be observed *in vivo* for at least 15 min after systemic injection in mice. In this case the NPs were mostly located in the liver [283]. PEG-functionalized SiO_2@$SrMgSi_2O_6$:Eu^{2+}, Dy^{3+} previously irradiated with near UV light (365 nm) was still observable after more than 1 h after peritoneal injection in mice [122]. H22 tumor bearing mice have been imaged *in vivo* with folic acid and peptide functionalized $ZnGa_2O_4$:Cr^{3+}, Eu^{3+} PLNPs. The NPs were irradiated in advance with UV light (254 nm) and kept their luminescence for 1 h after intravenous injection. Interestingly, the PLNPs could be re-excited at the tumor site with 650 and 805 nm lasers, which permitted extra observation for at least 5 min more [47]. NIR emitting PEG-functionalized $Zn_{2.94}Ga_{1.96}Ge_2O_{10}$:$Cr^{3+}$, Pr^{3+} PLNPs showing luminescence for more than 15 days have been used for *in vivo* bioimaging (Figure 14) and have also been used for cancer cell targeting after conjugation with arginylglycylaspartic acid [119].

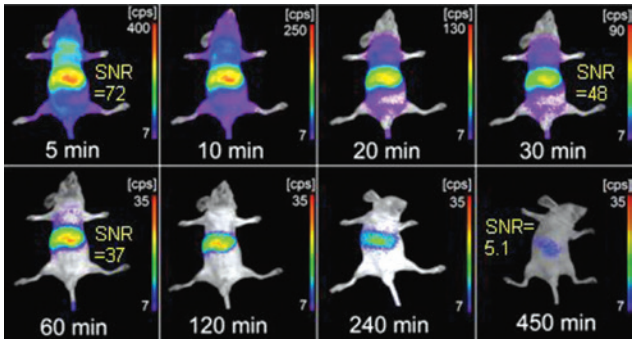

Figure 14: *In vivo* NIR luminescence images for increasing times of a normal mouse after intravenous injection of $Zn_{2.94}Ga_{1.96}Ge_2O_{10}$:$Cr^{3+}$, Pr^{3+} PLNPs (0.6 mg, 10 min irradiation with a 254 nm UV lamp before injection).
Taken from [119]. Reproduced with permission of the American Chemical Society. Copyright © 2013.

4 Magnetic resonance imaging applications

4.1 Magnetic resonance principles

MRI is a non-invasive diagnostic technique that produces 3D tomographic images of organs and tissues with high spatial resolution and soft tissue contrast. An important advantage of MRI is that no ionizing radiation or radioactive agents are necessary to record the images. MRI is based on the response of proton magnetic moments when submitted to a radiofrequency (RF) pulse in the presence of an external magnetic field (B_0). When exposed to B_0 the magnetic moments of the protons produce a net magnetization in the longitudinal z axis (Figure 15). The RF pulse flips the net magnetization away from its original axis. After the RF pulse disappears, the magnetization returns to its original state (relaxation) through two different and independent relaxation processes: longitudinal (T1) and transverse (T2) relaxation. The sensitivity of MRI is relatively low because the difference between normal and abnormal regions is usually subtle and the use of CAs is necessary to induce additional contrast. CAs are substances that shorten the relaxation times of protons, and their ability to do so is called relaxivity. Longitudinal relaxivity ($r1$) is the ability of the CA to shorten T1, while transverse relaxivity ($r2$) is the ability of the CA to shorten T2. MRI CAs are classified on the basis of their $r2/r1$ value. CAs that produce $r2/r1$ ratios close to 1 are known as T1 or positive CAs, and they produce an increase in signal intensity (bright images). T2 or negative CAs cause a reduction

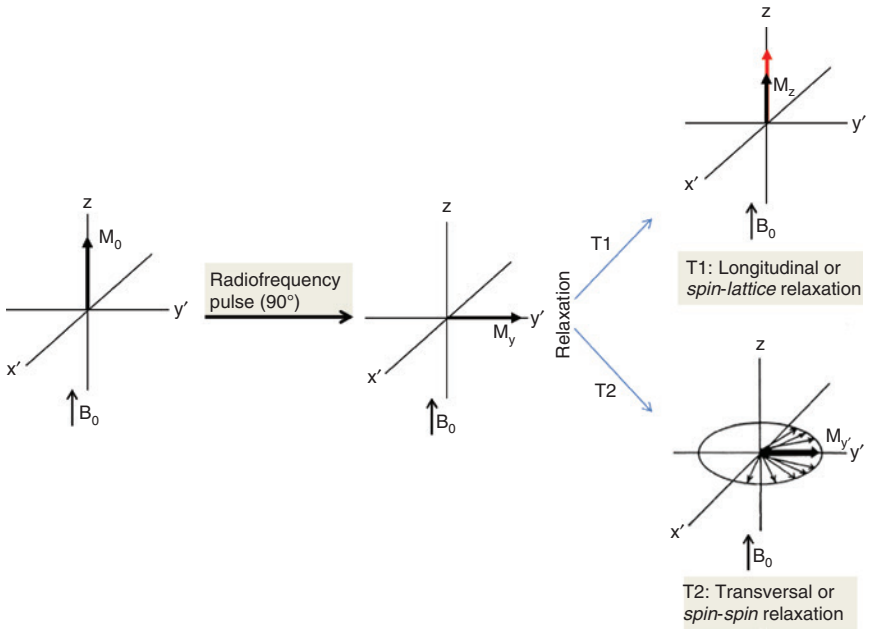

Figure 15: Magnetization vector M at thermal equilibrium, followed by a 90° RF excitation pulse and relaxation via spin-lattice and spin-spin interactions.

in signal intensity (dark images) and produce higher $r2/r1$ values (Figure 16).

4.2 Classical MRI contrast agents

Classical T2 CAs are the well-known superparamagnetic iron oxide (SPIO) nanoparticles, which have been frequently used owing to their freedom from strong magnetic interactions in dispersion and high stability under physiological conditions [300]. However, the dark image that the T2 CAs produce can be confused with blood or metallic deposits. Therefore, although iron oxide is more biocompatible than Gd- or Mn-based materials, which are the base of T1 CAs, the latter are preferred to avoid false results. An ideal T1 CA substance should be constituted by paramagnetic ions with long electronic relaxation times. Among the paramagnetic ions with a large number of unpaired electrons such as Gd^{3+} and Mn^{2+}, the former is preferred as T1 CA because it has the highest number of unpaired electrons and a long electronic relaxation time, much longer than that of other lanthanide ions, which favors relaxivity. The ionic radius of Gd^{3+} (108 pm) is very close to that of Ca^{2+} (114 pm). Free Gd^{3+} is therefore a competitive inhibitor of physiologic processes that depend on Ca^{2+} influx, including voltage-gated calcium channels and the activity of some enzymes. Different chelating agents have therefore been used to confine the free ion. At present, nine Gd-containing CAs are commercially marketed, all of them being Gd^{3+} chelates [301]. However, these relatively small molecules generally have a short circulation time in the vascular system, which is an obstacle for capturing long MRI scans.

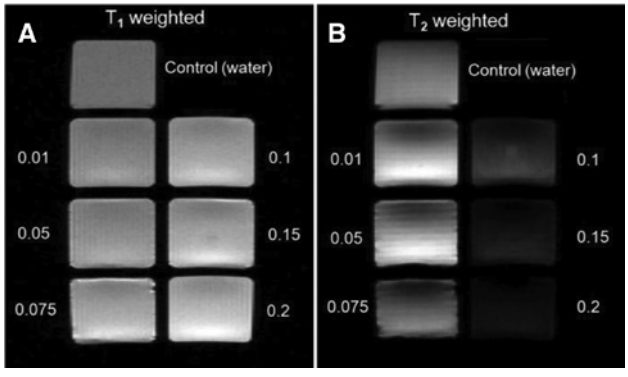

Figure 16: MR images of T1-weighted (A) and T2-weighted (B) $NaGd(MoO_4)_2$ NP suspensions at concentrations ranging from 0.01 mM (top left) to 0.2 mM (bottom right).
Taken from [89]. Published by The Royal Society of Chemistry.

4.3 Ln-based NPs as MRI CAs

Although not yet commercialized, Gd-based inorganic NPs constitute an important research focus in the MRI field. In addition to an excellent contrast enhancement, Ln-based NPs present long circulating times and are

easy to functionalize, which make them an interesting alternative to the traditionally used Gd chelate CAs commented on above. A large variety of them, ranging from oxides [302] to fluorides [303, 304] and sulfides [305], as well as Gd oxysalts [44, 64, 180, 306], have been synthesized and demonstrated good ability as T1 CAs. In many cases, an even higher level of image resolution was shown with the use of Ln-based NPs than with Gd chelates. For example, $NaGdF_4$ nanodots exhibit an $r1$ value which is 2.4-fold that of clinically used T1 CA Magnevist. Attractively, these nanodots can be used for magnetic resonance (MR) angiography with a vascular signal much stronger than that using clinical MR CAs at the same dose (Figure 17) [303].

The relationship between NP size and relaxivity properties has been widely analyzed in the literature with different conclusions. Although the mechanism of proton relaxation has mainly been described for Gd chelates [307], it is accepted that Gd^{3+} ions at the NP surface should contribute more to relaxivity than ions in the core of the particle, as water molecules have direct access to the former [308]. This hypothesis explains the general observation consisting in the increase of $r1$ value with increasing the surface/volume (S/V) ratio [308–310]. For example, increasing relaxivity $r1$ values from 2.34 mM^{-1} s^{-1} to 6.13 mM^{-1} s^{-1} have been found for $Eu_{0.2}Gd_{0.8}PO_4$ NPs with decreasing particle size from 145 nm to 40 nm [311]. However, in some cases, a non-monotonic behavior of $r1$ versus particle size has been reported. For instance, 5, 15 and 20 nm diameter $NaGdF_4$ spherical NPs showed, respectively, 6.20, 5.70 and 8.78 mM^{-1} s^{-1} [312]. This result has been explained by the contribution of the tumbling time of the NP, which increases as the NP size increases, counteracting the effect of the S/V ratio on the relaxivity [304].

Although the aforementioned NPs have been shown to increase the contrast in single-modal MRI images, they respond only in a single imaging mode and frequently encounter ambiguities in the MR images. Consequently, the research on inorganic NPs that serve as both T1 and T2 CAs for dual-modal MRI has recently attracted considerable interest because they reduce the potential false negative results, providing an unambiguous diagnostic. Interestingly, while $BaGdF_5$ NPs were shown to be potential positive CAs in T1-weighted MRI [98], doping $BaGdF_5$ NPs with 50% Er produced a binary CA for T1/T2 dual-weighted MRI (Figure 18) thanks to the negative contrast effects exhibited by Er^{3+}, which are due to the large magnetic moment of this lanthanide ion (μ_{eff} = 9.58 μ) compared to that of Gd^{3+} (μ_{eff} = 7.94 μ) [313].

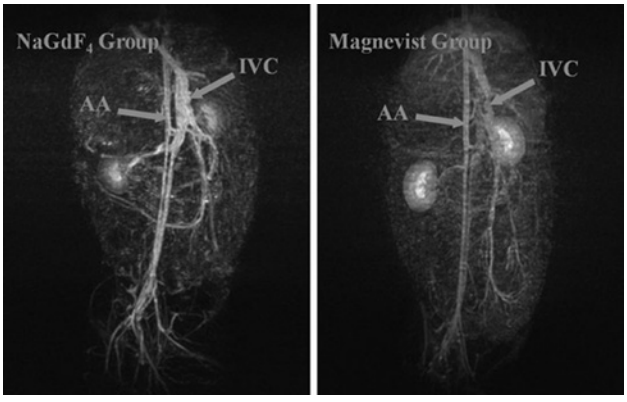

Figure 17: MR angiography of rabbits within 3 min after injecting with the $NaGdF_4$ nanodots (left) or Magnevist (right) at the same dosage (13 mg Gd/kg): abdominal aorta (AA) and inferior vena cava (IVC).
Taken from [303]. Reproduced with permission of John Wiley and Sons. Copyright © 2014.

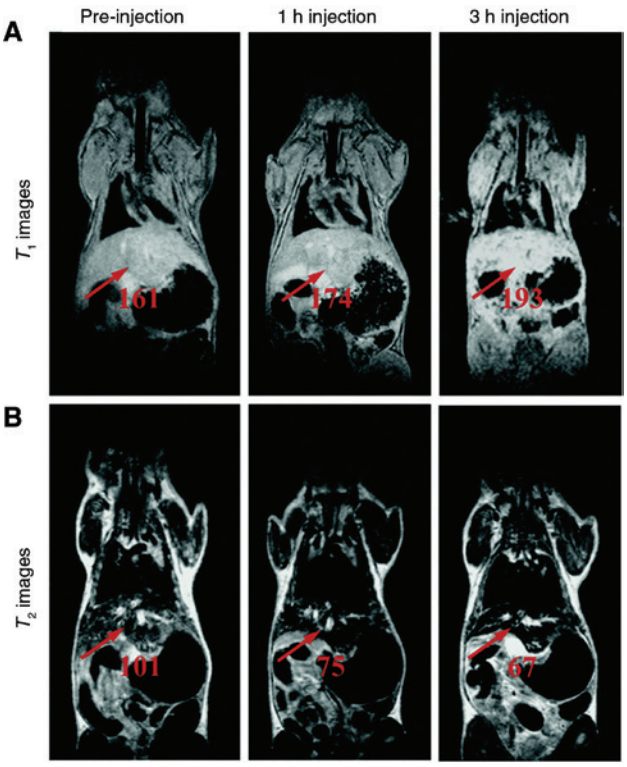

Figure 18: (A) T1-weighted and (B) T2-weighted *in vivo* coronal MRI images of a healthy mouse before injection as well as at 1 and 3 h after the intravenous injection of $BaGdF_5$:50 mol % Er NPs into the tail vein.
The arrows indicate the liver locations with contrast-enhancing effects, and the numbers below are the corresponding average signal intensities. These *in vivo* MRI images were acquired by a 1.0 T MRI system. Taken from [313]. Reproduced with permission of The Royal Society of Chemistry. Copyright © 2016.

4.4 MRI CAs for high magnetic fields

MRI CAs have been traditionally used in MRI scans recorded at low magnetic fields (<3 T). Higher magnetic fields would provide higher MRI spatial resolution, better signal-to-noise ratio and shorter imaging acquisition times [314, 315]. Current clinical CAs are less effective at ultra-high magnetic fields than at lower fields [315]. For example, the optimum magnetic field strength for Gd^{3+} chelates is <1 T, while their $r1$ value is reduced to $r1/3$ at 3 T. The clinically used T2 CA SPIO suffers magnetization saturation at 1.5 T, and increasing the magnetic field will not therefore increase the $r2$. Based on the fact that the magnetization of lanthanide-based NPs does not saturate at clinic field strength, and that their magnetic moment increases with the field strength before saturation, Zhang et al. [316] have recently reported *in vivo* studies that demonstrate that both $NaDyF_4$ and $NaHoF_4$ NPs with modulated sizes (9–40 nm) and shapes (spherical-like, hexagonal prism and rod-like) are good candidates for T2 CA for high-field (9.4 T) MRI.

5 X-ray computed tomography imaging

5.1 Basics of X-ray computed tomography

CT is a tissue-imaging technique based on the X-ray attenuation by the tissues. The ability of matter to attenuate X-rays is measured in Hounsfield units (HU). The name of this unit is in honor of Sir Godfrey Hounsfield (1919–2004) – one of the pioneers of CT. Water is assigned, by definition, a value of 0 HU and air a value of –1000 HU. For a material with a linear X-ray attenuation coefficient μ, the corresponding HU value is calculated using the following equation:

$$\mathrm{HU} = \frac{(\mu - \mu_{\mathrm{water}})}{\mu_{\mathrm{water}}} \times 1000$$

CT allows for higher resolution 3D details of tissues than other tomography techniques like positron emission tomography, which also uses an ionizing radiation (gamma-rays). Likewise, the temporal resolution of CT is much higher than that of MRI, which can take several minutes to record a scan. These advantages make this imaging technique one of the most used diagnostic techniques in hospitals nowadays, in spite of the concerns about the ionizing X-ray radiation.

5.2 Classical CT contrast agents

Although the contrast resolution of CT is much higher than that of conventional radiography, it is convenient to use CAs with a high capacity to absorb X-rays for a better delineation of regions of interest. The interested readers can refer to two recent reviews on this subject by Liu et al. [317] and Lusic and Grinstaff [36]. CT CAs are substances containing high Z elements because of the Z^4 dependence of the X-ray absorption coefficient of an atom ($\mu = \rho Z^4/AE^3$, where ρ = density of the material, Z = atomic number, A = atomic mass and E = energy of the X-ray beam). Iodine-based chelates ($Z_{\mathrm{Iodine}} = 53$) and barium sulfate ($Z_{\mathrm{Barium}} = 56$) suspensions are classical CT CAs approved for human use. Both of them present, however, several inconveniences such as the inherent toxicity of Ba^{2+} ions, which hinders use other than in gastrointestinal imaging, and the short circulation time and high osmolality of iodinated compounds, which prevent wider application. These disadvantages are strengthened by the fact that CT imaging requires high dosages of CAs.

5.3 Ln-based NPs as CT CAs

Ln-based NPs have recently become a research focus in CT imaging due to their prolonged circulation times, reduced toxicity, targeting capacity, which decreases the dosage, and possibility of multimodal imaging plus sensing and theranostic [21, 22]. Most of the lanthanide-based NPs synthesized as CT CAs are, in fact, multimodal agents, and they are mainly fluorides, due to the above commented advantages of this chemistry for UC luminescence. For example, Zhai et al. demonstrated [318] the good X-ray CT imaging ability of $LiLuF_4$@$LiGdF_4$:Yb^{3+}, Tm^{3+}@$LiGdF_4$ NPs. The authors evaluated the *in vitro* contrast efficacy by comparing the X-ray absorption of the core-shell-shell NPs with that of iobitridol (an iodinated chelate widely used as CT CA). It was found that, at equivalent concentrations, the X-ray absorption of the NPs was higher than that of iobitridol. To assess the potential of the NPs for *in vivo* CT imaging, the authors injected a solution of the core-shell-shell NPs intratumorally. A clear contrast enhancement could be detected from the tumor site after injection (Figure 19). The NPs also showed bright upconversion luminescence and good T1-weighted MRI contrast images. Another interesting example of multimodal (CT, MRI and drug delivery) Ln fluoride-based NPs with potential utility as CT CA is that published by Yang et al. [77]. In this case, the *in vitro* CT contrast images were compared with those of iopromide, another CA widely used in clinic CT, at

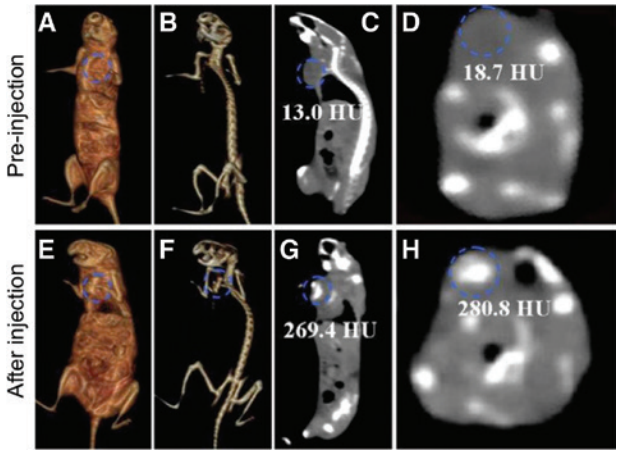

Figure 19: *In vivo* CT images of a tumor-bearing mouse before (A–D) and after (E–H) injection of $LiLuF_4$@$LiGdF_4$:Yb^{3+}, Tm^{3+}@$LiGdF_4$ NPs at the tumor site.
The position of tumor is marked by blue circles. Adapted from [318]. Reproduced with permission of Elsevier. Copyright © 2015.

different concentrations of lanthanides and of iodinated chelate. Significantly, the X-ray absorption of the NPs was higher than that of iopromide at equivalent concentrations (Figure 20), indicating that the NPs can provide an equivalent contrast at a lower dose compared with the iopromide.

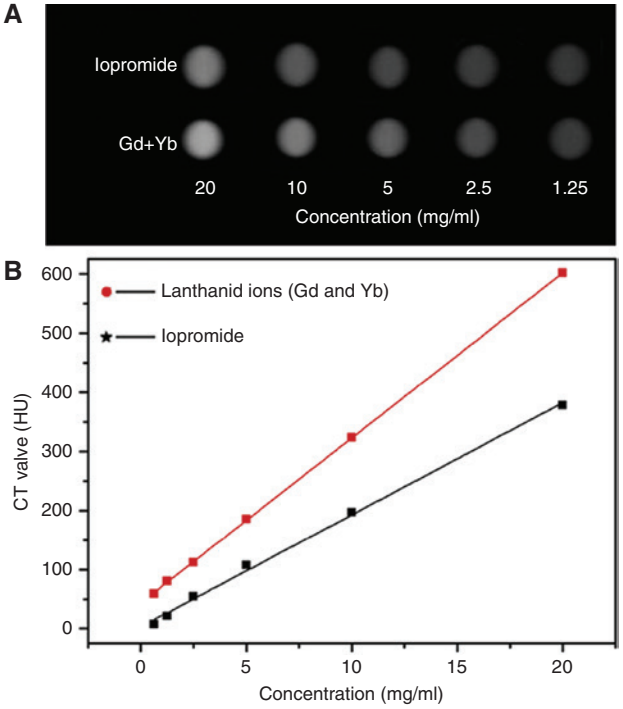

Figure 20: *In vitro* CT images of UCNPs with different lanthanide ion concentrations (A), and CT value (HU) of samples as a function of lanthanide ions (Gd and Yb) concentrations (B).
Taken from [77]. Reproduced with permission of Elsevier. Copyright © 2013.

6 Multimodal imaging

One of the main advantages of RE-based nanostructures is the possibility of combining different RE in the same nanostructure. NPs showing different luminescent, magnetic and X-ray absorption properties attract currently high research interest, since they give rise to multimodal imaging nanomaterials. Some examples of RE-based NPs for multimodal imaging have been already mentioned in the previous sections, which were focused on the description of the different imaging techniques. Luminescent NPs doped with different and appropriate RE (including core/shell structures) can show downconversion and upconversion dual-modal emission. Of special interest are NIR to NIR and NIR to visible (vis) emissions. For example, both downconversion and upconversion NIR to NIR and NIR to vis emission have been reported for β-$NaGdF_4$:Nd^{3+}@$NaGdF_4$:Tm^{3+}, Yb^{3+} core-shell NPs [240]. In these NPs, a careful control and optimization of the RE distribution was carried out. Similar features were reported for $NaGdF_4$:Yb^{3+}, Er^{3+}, Nd^{3+}@$NaGdF_4$:Nd^{3+} core-shell NPs, which emit both visible and NIR light after laser excitation at 793 nm through different ET mechanisms between the RE [239]. Due to the presence of Gd, the NPs were also suitable as CA for MRI. Moreover, $NaGdF_4$:Tm^{3+}, Er^{3+}, Yb^{3+} NPs are used as NIR to NIR emitters and also as CA for *in vivo* MRI [277]. Other examples are $BaLaF_5$:Mn^{2+}:Yb^{3+}:Er^{3+}NPs, which have been used for both *in vitro* and *in vivo* upconverting luminescence and CT bioimaging [319]. In other cases, the doping with other elements such as Co provides magnetic properties, as it occurs in $NaYF_4$:Yb^{3+}, Tm^{3+}:Co^{2+} nanorods, which are used for both *in vitro* and *in vivo* luminescent and T2-weighted MRI imaging [320]. Some systems with three- and even four-modal imaging have been reported in the literature. For example, $NaGdF_4$:Yb^{3+}/Er^{3+}@$NaGdF_4$:Nd@sodium-gluconate have been used for upconverting luminescent and MRI as well as for CT [321]; $BaYbF_5$:Tm@$BaGdF_5$:Yb, Tm NPs have been used for both *in vitro* and *in vivo* UC, MRI and CT imaging [322]; and $NaLuF_4$:Yb, Tm@$NaGdF_4$(^{153}Sm) NPs have been employed for *in vivo* UC luminescence and magnetic resonance bioimaging and CT tomography. Interestingly, the doping with the radioactive ^{153}Sm made the NPs also suitable for single-photon emission computed tomography imaging [323].

7 Biosensing applications

Ln-based sensing systems are considered a new generation of fluorophores and have also raised a lot of interest in the bioanalytical sensing field. As in the previous applications, such potential is owing to their unique properties, i.e. high quantum yield, narrow emission peaks, large stoke shifts, upconversion emission potential, good chemical stability and low toxicity [17, 19], which make them superior in some aspects in comparison to organic fluorophores and other fluorescent NPs. Although the research on Ln-doped NPs is still in its infancy, very diverse types of these NPs have been reported as sensing probes, such as lanthanide doped nanoparticles (Ln-doped NPs), lanthanide coordination polymers (Ln-CPs) [324] and lanthanide-containing metal-organic frameworks (Ln-MOFs) [325].

Depending on their surface chemistry and/or structure, and therefore the mechanism involved in the sensing response, three main types of sensing systems can be distinguished: (i) ligand-free Ln-doped NPs, that is NPs without any recognition ligand on their surface, (ii) functionalized Ln-doped NPs, where specific ligands, groups or motifs have a recognition capability of the target analyte, and (iii) Ln ions are embedded in an organic framework (MOFs) or polymer. In the former case the response of the system is mainly governed by a physical mechanism, whereas in the second case there is a combination of chemical (i.e. analyte-recognition ligand interaction) and physical processes. In the last case physico-chemical processes (i.e. analyte-metal/analyte-ligand interactions and porosity) together with physical mechanisms provoke the response. Concerning the physical mechanisms behind the optical response, they can be roughly divided into three classes: (i) luminescence resonance energy transfer (LRET), (ii) ET mediated by a ligand and (iii) emission-reabsorption (inner filter effect, IFE), see Figure 21. The differences and pros/cons of each type of system will be explained by means of selected examples.

An interesting example of using ligand-free Ln-doped NPs for sensing purposes was reported recently by Guo et al. [327]. They proposed the detection of water molecules based on the intrinsically nonlinear upconversion amplification process of $NaYF_4$:Yb^{3+}, Er^{3+} NPs, being able to reach a detection limit as low as 0.008 vol % (80 ppm) in an organic solvent. The presence of water causes the quenching of the upconversion emission process, which is mainly attributed to efficient ET between upconversion NPs and water molecules as well as water-absorption-induced excitation energy attenuation. Thanks to the high photostability of the upconversion emission, an important advantage of this sensing system is its potential to be used for long-term and real-time monitoring of water content. However, owing to the fact that several quenching effects are involved in the response of this system (i.e. ET and direct water absorption of excitation energy) and the contribution of each one is still not well understood, a deeper understanding is required before opening the door to the development of other optical sensors relying on leveraging nonlinear upconversion process of Ln-doped NPs.

Luminescent Ln-doped NPs have also been suggested as nanothermometers [328]. For example, Eu^{3+} and Tb^{3+} emissions in ligand-free $NaGdF_4$:Yb^{3+}, Tm^{3+}@$NaGdF_4$:Tb^{3+}, Eu^{3+} core-shell NPs exhibit higher sensitivity in a wide range from 125 to 300 K (Figure 22A) [329]. The temperature dependence of many of the lanthanides' photophysical properties, including the emission intensity and the excited-state lifetime or rise time, is exploited in these systems. In particular, the dependence of the fluorescence intensities from two emitting levels of lanthanides [332] has been exploited for monitoring temperature changes in different cell models such as HeLa cervical cancer cells [333] and human embryo kidney cells [334], which allows the investigation of how thermal processes develop at cellular level, e.g. enzymatic reactions, cellular death and other physiological processes. The main drawbacks of these nanothermometers are related with their sensitivity and precision. The quantum yield of the upconversion process is low, and consequently, the maximum relative sensitivity values are around ~0.5% K^{-1} at the physiological temperature range. Moreover, resolving temperature with a precision lower than 0.1° is still to be demonstrated [334]. Thus, further improvements are needed.

Regarding the sensing applications involving functionalized Ln-doped NPs, it must first be noted that they are far more numerous because playing with diverse functionalization and different mechanisms enables wider possibilities. As Ln-doped NPs do not show an intrinsic or specific luminescence response to most of the analytes (e.g. pH, oxygen, metal ions and biomolecules), the functionalization of their surface with suitable indicator dyes or recognition elements imparts to the NP the selectivity or specific recognition required for most of the sensing applications, especially for biosensing [335]. A huge diversity of recognition elements have been reported, the most commonly used being antibodies [336], DNA [337], aptamers [338–340], avidin/biotin pair [341] and polypeptides [342].

The most promising systems in this direction are those which use upconverting Ln-doped NPs (UCNPs) as donors in FRET (Förster resonance energy transfer)-based sensing configurations, resulting then in UCNP-based

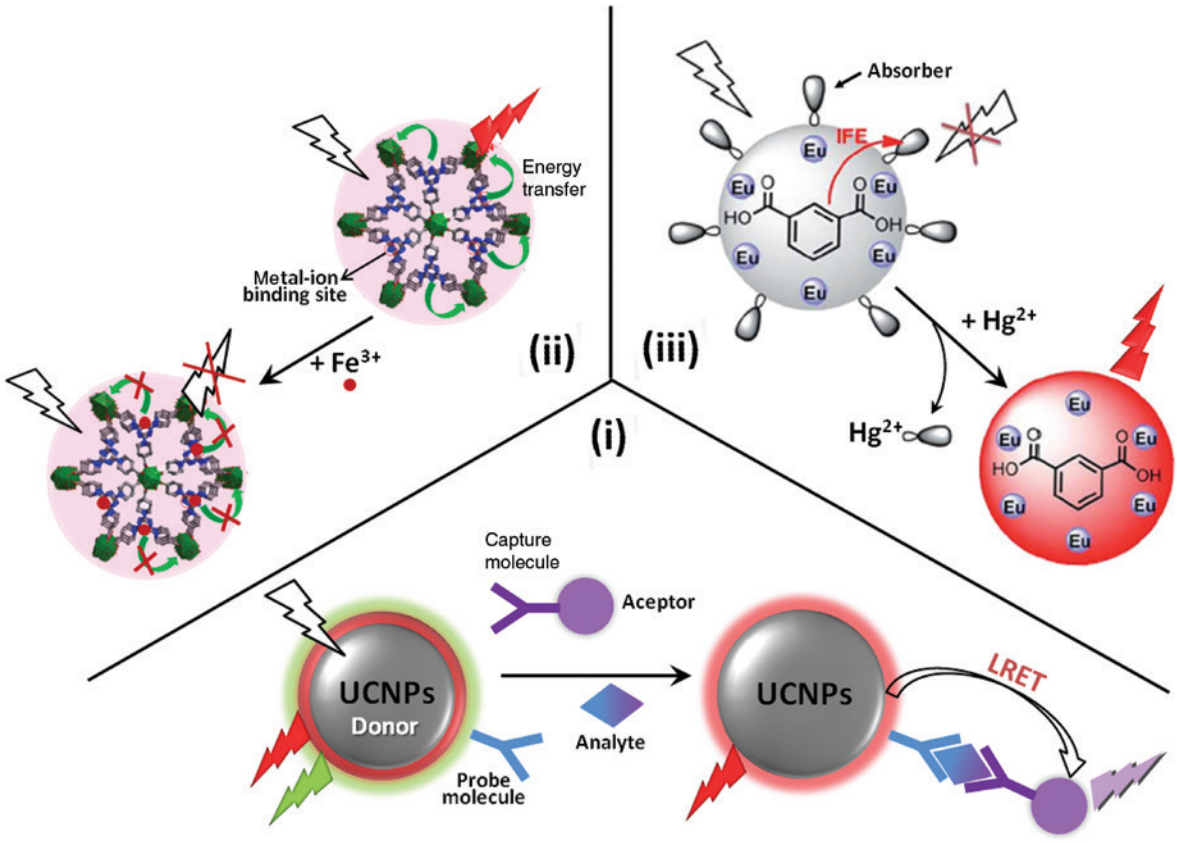

Figure 21: Different mechanisms involved in the optical response of the Ln-based sensing systems.
(i) LRET. A UCNP donor produces anti-Stokes emission upon excitation. Consequently, it can excite the attached acceptors via FRET process. The intensity of the sensitized emission from the acceptor is proportional to the analyte concentration in the reaction. (ii) ET mediated by a ligand. After excitation of the ligand, there is an ET to the emissive states of the Eu^{3+} ion. Complexation following the introduction of metal-ion guests into the MOF channels perturbs the electronic structure of the ligand. These changes, in turn, affect the efficiency of the ET process, and hence the observed changes in the luminescence intensity (adapted from [326]. Reproduced with permission of the American Chemical Society. Copyright © 2013). (iii) Emission-reabsorption (IFE). After excitation of the ligand, there is an ET to the emissive states of the Eu^{3+} ion. When an absorber molecule is present, this absorbs the light emitted by the Eu^{3+} ion, and consequently there is a quenching of the fluorescence. If the analyte forms a complex with the absorber molecule, the fluorescence is recovered due to the suppression of the IFE process (adapted from [324]. Reproduced with permission of The Royal Society of Chemistry. Copyright © 2016).

LRET assays [343]. UCNPs are conjugated with energy acceptors, whose excitation spectra has to overlap with the emission spectra of the NPs. The acceptor can be organic fluorophores [111, 144, 344, 345], fluorescent proteins [346], metallic NPs [341], graphene oxide (GO) [338, 339, 347, 348], carbon NPs [342] and semiconductor QDs [345, 349, 350]. The working principle of upconversion LRET [depicted in Figure 21(i)] has demonstrated its huge potential through the development of sensing systems for the determination of 17β-estradiol [336], enzymatic activity [351], matrix metalloproteinase [342], mycotoxins [338], ATP [339], IgG [352], glucose [347] and pesticides [353], among others. We discuss here just four selected examples in order to describe the mechanism responsible for the sensing response.

Liu et al. were able to measure cyanide concentrations in water with a very low detection limit of 0.18 μM CN^-. $NaYF_4$:Yb^{3+}, Er^{3+}; Tm^{3+} were conjugated with a chromophoric iridium complex. The absorption of this complex overlaps with one of the emissions of the UCNPs (around 540 nm), giving rise to a FRET process. The absorption of the complex is affected by the presence of CN^- anions, which is highly reduced. FRET is thus also suppressed, and the analysis of the absorption of the complex with respect to the 800 nm emission of the UCNPs, which is taken as internal reference, can be used to measure CN^- species (Figure 22B) [330].

Wu et al. developed a UCNPs-GO-based LRET immunoassay for sensitive detection of different mycotoxins, including ochratoxin A (OTA) and fumonisin B1 (FB1) [338].

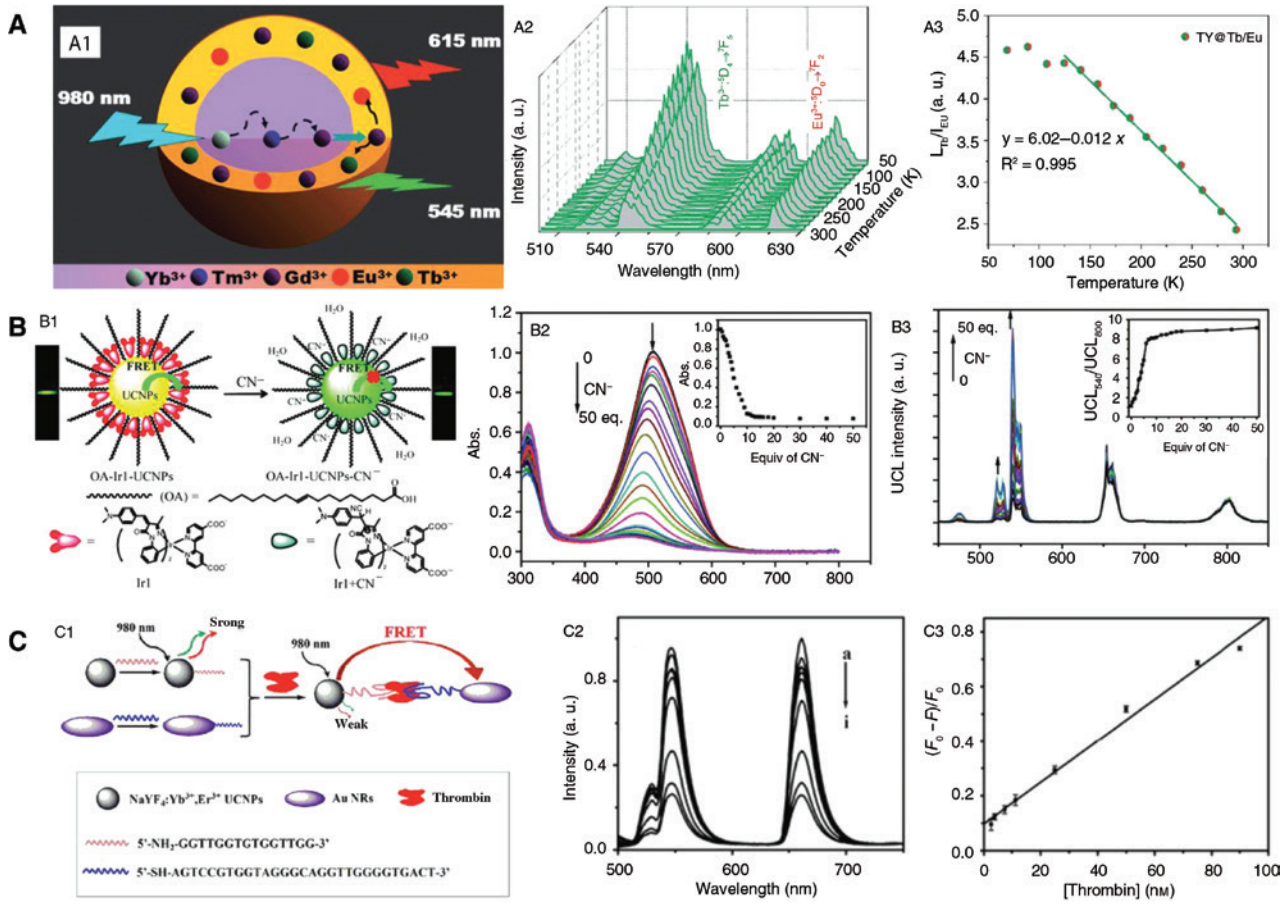

Figure 22: (A) Sensing of temperature: (A1) Schematic design of $NaGdF_4$:Yb^{3+}, Tm^{3+}@$NaGdF_4$:Tb^{3+}, Eu^{3+} core-shell NPs for nanothermometers; (A2) Upconversion emission spectra of $NaGdF_4$:Tm^{3+}, Yb^{3+}(1/49%)@$NaGdF_4$:Tb^{3+}, Eu^{3+}(15/1.5%) core-shell NPs recorded between 50 and 300 K; (A3) Temperature-dependence of the intensity ratio of Tb^{3+} (545 nm) to Eu^{3+} (615 nm) and the linear fitting curve. Adapted from [329]. Reproduced with permission of The Royal Society of Chemistry. Copyright © 2014. (B) Sensing of inorganic ions: (B1) Proposed recognition mechanism and FRET process of iridium(III) complex-coated $NaYF_4$:20%Yb^{3+}, 1.6%Er^{3+}, 0.4%Tm^{3+} NPs (OA-Ir1-UCNPs) towards cyanide anion (CN^-); (B2) changes in absorption spectra of OA-Ir1-UCNPs upon addition of CN^-. Inset: absorbance at 505 nm as a function of CN^- concentration; B3) changes in UCL spectra of OA-Ir1-UCNPs upon addition of CN^-. Inset: ratio (I_{540}/I_{800}) of UCL intensities as a function of CN^- concentration. Adapted from [330]. Reproduced with permission of the American Chemical Society. Copyright © 2011. (C) Sensing of biomolecules: (C1) Proposed recognition mechanism and FRET process between $NaYF_4$:Yb^{3+}, Er^{3+} UCNPs-TBA_{15} and AuNRs-TBA_{29} (TBA_{15} and TBA_{29} are aptamers) for the detection of thrombin; (C2) changes in UCL spectra of UCNPs-TBA_{15} after addition of various concentrations of thrombin from 0 to 90 nM; (C3) the relationship between the fluorescence quenching efficiency and the concentration of thrombin. Adapted from [331]. Reproduced with permission of Elsevier. Copyright © 2013.

BaYF:Yb^{3+}, Er^{3+} and BaYF:Yb^{3+}, Tm^{3+} UCNPs conjugated with specific mycotoxin aptamers were used as donors, while GO acted as acceptor quenching completely the luminescence of aptamer UCNPs due to the close intermolecular distance caused by π-π stacking interaction. In the presence of mycotoxins, the aptamers prefer to bind to their corresponding mycotoxins, and therefore the π-π coupling of GO-aptamer is lost, resulting in negligible luminescence quenching. Changes in the fluorescence intensity of BaYF:Yb^{3+}, Er^{3+} and BaYF:Yb^{3+}, Tm^{3+} were related to the concentration of OTA and FB1 respectively, leading to detection limits of 0.02 ng ml^{-1} (OTA) and 0.1 ng ml^{-1} (FB1). Importantly, this is the first example of multiplexed UCNP-based LRET system for the simultaneous detection of two target analytes.

Another example using Au NPs as acceptor has allowed the detection of short genes of H7 subtypes [354]. PEI-modified $BaGdF_5$:Yb^{3+}, Er^{3+} UCNPs were chemically conjugated with capture oligonucleotide probes, while AuNPs were linked to hemagglutinin H7 oligonucleotide sequence. The hybridization process between complementary strands brought the energy donor and acceptor into close proximity, leading to the quenching of fluorescence of UCNPs. The extremely low detection limit achieved, as

low as 7 pM, should be noted. A similar idea was applied to the sensing of thrombin with $NaYF_4$:Yb^{3+}, Er^{3+} NPs and gold nanorods both conjugated with thrombin aptamers. In the presence of thrombin both NPs were in close proximity and a FRET process between the UCNPs and the Au nanorods takes place, giving rise to attenuation of the emission of the UCNPs (Figure 22C) [331].

These examples showed that typical drawbacks associated to traditional FRET systems using downconversion organic dyes could be overcome by using UCNPs as donors because of their large anti-Stokes shifted, narrow-band emission and high signal-to-noise ratio (i.e. no problems associated with autofluorescence of biological material as NIR light is used for excitation of UCNPs), and as a result they would lead to a higher accuracy and selectivity in diagnostic applications and also in high-throughput screening approaches. However, one principal drawback of using UCNPs for biomedical applications is that the strong absorption of water molecules at 980 nm (one of the commonly used excitation wavelengths) causes an overheating of the surrounding medium and subsequent cell death. The development of UCNPs which can be excited at around 800 nm could minimize this side effect [355]. Other sensing assays based on different resonance ETs, and consisting of nanostructured systems containing REs have been reported in the literature, especially those involving lanthanide complexes [356]. For example, cadmium selenide QDs conjugated with europium complexes and biotin have been used for the detection and quantification of streptavidin [357]; a similar strategy was employed with the conjugation of biotin-terbium complexes with streptavidin-functionalized QDs [358]; semiconductor nanorods (quantum rods) conjugated with terbium complexes with long photoluminescence lifetimes have been suggested to be a powerful tool for homogeneous optical biosensing [359]; QDs conjugated with terbium-labeled monoclonal primary antibodies against prostate specific antigen have been employed for FRET immunoassays for prostate specific antigen [360]; polystyrene NPs labeled with Eu^{3+} chelates and coated with Alexa Fluor 680 labeled γ-globulin can be used for the analysis of nucleic acid samples [361]; and transfers between terbium complexes, organic dyes and QDs (multistep FRET) have also been reported [362]. Eu chelates can also be conjugated with peptides for monitoring kinase catalyzed tyrosine phosphorylation through a quenching resonance energy transfer (QRET) between the Eu chelate and a soluble quencher molecule. A specific antibody binds to the phosphorylated form of the Eu^{3+} peptide protecting the chelate from the quencher, while the luminescence of the unphosphorylated form is efficiently quenched allowing thus determination of kinase inhibitors [363]. The potential of similar approaches based on QRET for the screening of enzyme inhibitors has recently been reviewed [364], which emphasizes the simplicity and rapidity of this technique that make it ideal for high-throughput screening analyses.

The third type of system with relevance in the sensing field involves the use of Ln-MOFs and Ln-CPs. The beneficial property of these structures, microporosity, can be used together with luminescence to create sensing for very different analytes on the basis of a dependence of the analyte on the luminescence properties of the host lattice. In these systems the luminescent intensity of Ln-MOFs and Ln-CPs is typically altered depending upon the identity of analytes through analyte-metal or analyte-ligand interactions.

Most of the Ln-MOFs systems are responsive due to an ET process mediated by the ligand. Depending on the nature of the interaction and the resulting perturbation to the electronic structure of the ligand, the efficiency of ligand-to-Ln ET is affected, leading to compromised or enhanced population of the Ln emissive states and, ultimately, the quenching or enhancement of its luminescence. To date, several examples for sensing a variety of species (i.e. gases, metal ions and organic molecules) have been reported [326, 365–367]. As an example, ion sensing of Fe^{3+} and Zn^{+2} has been achieved utilizing Eu-BTPCA MOFs ($BTPCA^{3-}$ = 1,1′,1″-(benzene-1,3,5-triyl)tripiperidine-4-carboxylate) [326]. Such metal ions have an affinity to N-donor sites that remain available upon framework construction as the Eu^{3+} ions selectively only bind to the carboxylate groups due to their high oxophilicity. When Fe^{3+} ions were present and bound to the Eu-BTPCA MOFs, the luminescence is quenched owing to the reduction of the ET efficiency of the BTPCA linkers to excited 4f states of Eu^{3+}. A study of the selectivity showed that only Fe^{3+} led to complete quenching of the luminescence, whereas most ions give a somewhat non-specific quenching. In contrast, binding to Zn^{2+} led to a remarkable increase of the Eu^{3+} emission intensity. Both observations can be explained by a change of the energy of the relevant excited ligand triplet states by their donor sites binding to the 3d metal ions, which diminishes or increases the match in energy with the 4f states [368]. Thus, it is demonstrated that the antenna effect is vital for this kind of sensing systems based on Ln-doped MOFs. Organic molecules which are good electron donors or acceptors can also influence the ET efficiency and thus the intensity of lanthanide luminescence. Based on that, 10 different nitroaromatic compounds have been detected by measuring the luminescence quenching percentage of Eu-MOFs $[Eu_3(MFDA)_4(NO_3)(DMF)_3]$, ($H_2MFDA$ = 9,9-imethylfluorene-2,7-dicarboxylic acid) [365].

Variable responses were obtained for each nitroaromatic molecule, concluding that the different electron affinities together with the competition in light absorption between the MOF antenna ligand and the nitro compound were the key aspects responsible for the sensing response.

On the other hand, in systems consisting of Ln-CPs the sensing response is usually through IFE. The IFE refers to the absorption of the excitation and/or emission light of a fluorophore by an absorber in the detection system. A significant advantage of this mechanism is its simplicity as it does not require a complicated chemical linkage between the absorber and fluorophore for getting a response. Li et al. developed a method for the detection of Hg^{2+} in biological fluids by using Eu/IPA-CPs, where isophthalic acid (IPA) acted as bridging ligand that could sensitize the fluorescence of Eu^{3+} [324]. Because the excitation spectrum of Eu/IPA CPs strongly overlaps with the absorption band of imidazole-4,5-dicarboxylic acid (Im), the IFE process is very efficient, leading to a significant quenching of the fluorescence of Eu/IPA-CPs. Upon the addition of Hg^{2+}, however, the fluorescence was recovered due to the suppression of the IFE of Im through the formation of a Hg/Im complex. Following this strategy, the detection limit was of 2 nM, which is lower than the maximum allowable Hg^{2+} level in drinking water (10 nM) permitted by the US Environmental Protection Agency.

Unfortunately, a common problem of this third class of systems is the poor selectivity towards a specific target analyte, and therefore this is a challenging task for future development.

8 Perspectives and evolution

Despite the great advance achieved in the last years in the development of RE-based nanostructures for biotechnological applications, which is reflected in the huge amount of available MOFs and NPs (with or without surface functionalization) having many different compositions, morphology, size, properties and applications, some challenges and improvements still have to be addressed before these systems can be clinically used. Thus, from the synthetic point of view, efficient, large-scale and cost-effective methods have to be developed. Regarding the persistent nanophosphors, suitable methods for the synthesis of uniform NPs are strongly demanded, and new routes for the synthesis of MOFs at milder reaction conditions that are quicker and with a better control of the particle sizes should be developed. For both luminescent DCNPs and UCNPs, many efforts have to be made to enhance their global luminescence. In particular, the design of new transfer strategies that allow the excitation of DCNPs by NUV or visible light would increase the number of their applications, especially bioimaging, since they could be easily excited by standard fluorescence and cLSMs. The design of new DC NIR emitting NPs working in the biological windows (600–950 nm and 1000–1320 nm) is also of high priority. Development of multifunctional systems is undoubtedly one of the most important research focuses in the design of RE-based nanostructures for biotechnological applications. In fact, many of the luminescent RE-based NPs are designed to provide, at least, one additional functionality, either as MRI or as CT CA, thus providing an unambiguous diagnostic by combining the advantages of each modality. Among the main challenges in MRI CAs research is the optimization of both dual T1-T2 MRI CAs which help to reduce potential false negative results and MRI CAs able to work properly under high field magnets, which are the basis for the present trend in clinical MRI equipment. In addition, the study of the lifetime characteristics of UCNPs has started to attract greater attention and holds promise in the sensing field to further reduce the background noise associated with detection and to increase the potential of multiplexed methodologies. Exploiting the multiplexing capacities of these NPs for sensing applications is clearly a key issue for future prospects.

Finally, a deeper investigation on the biocompatibility of RE-based NPs, especially long-term toxicity studies, is still required.

Acknowledgments: This work was supported by a Junta de Andalucía (Spain) Talentia Postdoc Fellowship, co-financed by the European Union's Seventh Framework Programme, grant agreement no 267226, by the Spanish Ministerio de Economía y Competitividad (project MAT2014-54852-R to MO) and by the European Commission (grant FutureNanoNeeds to W.J.P.). C.C.C. acknowledges the Spanish Ministerio de Economía y Competitividad for a Juan de la Cierva – Incorporación contract.

References

[1] Zepf V. Chapter 1 – An overview of the usefulness and strategic value of rare earth metals A2 – Lima, Ismar Borges De. In: Filho WL, ed. Rare earths industry. Boston, Elsevier, 2016, 3–17.
[2] Du X, Graedel TE. Global in-use stocks of the rare earth elements: a first estimate. Environ Sci Technol 2011;45:4096–101.
[3] Chakhmouradian AR, Wall F. Rare earth elements: minerals, mines, magnets (and more). Elements 2012;8:333–40.

[4] Weller M, Overton T, Rourke J, Armstrong F. Inorganic chemistry. Oxford, Oxford University Press, 2014.
[5] Hötzer B, Medintz IL, Hildebrandt N. Fluorescence in nanobiotechnology: sophisticated fluorophores for novel applications. Small 2012;8:2297–326.
[6] Mout R, Moyano DF, Rana S, Rotello VM. Surface functionalization of nanoparticles for nanomedicine. Chem Soc Rev 2012;41:2539–44.
[7] Taeho K, Taeghwan H. Applications of inorganic nanoparticles as therapeutic agents. Nanotechnology 2014;25:012001.
[8] Murthy SK. Nanoparticles in modern medicine: state of the art and future challenges. Int J Nanomedicine 2007;2:129–41.
[9] Xia YN. Nanomaterials at work in biomedical research. Nat Mater 2008;7:758–60.
[10] Piana S, Reyhani M, Gale JD. Simulating micrometre-scale crystal growth from solution. Nature 2005;438:70–3.
[11] Alivisatos AP. Semiconductor clusters, nanocrystals, and quantum dots. Science 1996;271:933–7.
[12] Park J, Joo J, Kwon SG, Jang Y, Hyeon T. Synthesis of monodisperse spherical nanocrystals. Angew Chem Int Edit 2007;46:4630–60.
[13] Mai H-X, Zhang Y-W, Si R, et al. High-quality sodium rare-earth fluoride nanocrystals: controlled synthesis and optical properties. J Am Chem Soc 2006;128:6426–36.
[14] Huang XL, Teng X, Chen D, Tang FQ, He JQ. The effect of the shape of mesoporous silica nanoparticles on cellular uptake and cell function. Biomaterials 2010;31:438–48.
[15] Feliu N, Hühn J, Zyuzin MV, et al. Quantitative uptake of colloidal particles by cell cultures. Sci Total Environ 2016;568:819–28.
[16] Altınoğlu EI, Russin TJ, Kaiser JM, et al. Near-infrared emitting fluorophore-doped calcium phosphate nanoparticles for *in vivo* imaging of human breast cancer. ACS Nano 2008;2:2075–84.
[17] Wang G, Peng Q, Li Y. Lanthanide-doped nanocrystals: synthesis, optical-magnetic properties, and applications. Acc Chem Res 2011;44:322–32.
[18] Chen D, Wang Y. Impurity doping: a novel strategy for controllable synthesis of functional lanthanide nanomaterials. Nanoscale 2013;5:4621–37.
[19] Haase M, Schäfer H. Upconverting nanoparticles. Angew Chem Int Edit 2011;50:5808–29.
[20] Van den Eeckhout K, Poelman D, Smet P. Persistent luminescence in non-Eu^{2+}-doped compounds: a review. Materials 2013;6:2789.
[21] Park YI, Lee KT, Suh YD, Hyeon T. Upconverting nanoparticles: a versatile platform for wide-field two-photon microscopy and multi-modal *in vivo* imaging. Chem Soc Rev 2015;44:1302–17.
[22] Tu D, Liu Y, Zhu H, Chen X. Optical/magnetic multimodal bioprobes based on lanthanide-doped inorganic nanocrystals. Chem Eur J 2013;19:5516–27.
[23] Pellegrino T, Kudera S, Liedl T, Muñoz Javier A, Manna L, Parak WJ. On the development of colloidal nanoparticles towards multifunctional structures and their possible use for biological applications. Small 2005;1:48–63.
[24] Zyuzin MV, Honold T, Carregal-Romero S, Kantner K, Karg M, Parak WJ. Influence of temperature on the colloidal stability of polymer-coated gold nanoparticles in cell culture media. Small 2016;12:1723–31.
[25] Thanh NTK, Green LAW. Functionalisation of nanoparticles for biomedical applications. Nano Today 2010;5:213–30.
[26] Meyer LV, Schonfeld F, Muller-Buschbaum K. Lanthanide based tuning of luminescence in MOFs and dense frameworks – from mono- and multimetal systems to sensors and films. Chem Commun 2014;50:8093–108.
[27] Chen Y, Ma S. Microporous lanthanide metal-organic frameworks. Rev Inorg Chem 2012;32:81.
[28] He C, Liu D, Lin W. Nanomedicine applications of hybrid nanomaterials built from metal–ligand coordination bonds: nanoscale metal–organic frameworks and nanoscale coordination polymers. Chem Rev 2015;115:11079–108.
[29] Gnach A, Bednarkiewicz A. Lanthanide-doped up-converting nanoparticles: merits and challenges. Nano Today 2012;7:532–63.
[30] Liu Y, Tu D, Zhu H, Chen X. Lanthanide-doped luminescent nanoprobes: controlled synthesis, optical spectroscopy, and bioapplications. Chem Soc Rev 2013;42:6924–58.
[31] Liu Y, Tu D, Zhu H, Ma E, Chen X. Lanthanide-doped luminescent nano-bioprobes: from fundamentals to biodetection. Nanoscale 2013;5:1369–84.
[32] Dong H, Du S-R, Zheng X-Y, et al. Lanthanide nanoparticles: from design toward bioimaging and therapy. Chem Rev 2015;115:10725–815.
[33] Sedlmeier A, Gorris HH. Surface modification and characterization of photon-upconverting nanoparticles for bioanalytical applications. Chem Soc Rev 2015;44:1526–60.
[34] Zheng W, Huang P, Tu D, Ma E, Zhu H, Chen X. Lanthanide-doped upconversion nano-bioprobes: electronic structures, optical properties, and biodetection. Chem Soc Rev 2015;44:1379–415.
[35] Zhou J, Liu Q, Feng W, Sun Y, Li F. Upconversion luminescent materials: advances and applications. Chem Rev 2015;115:395–465.
[36] Lusic H, Grinstaff MW. X-ray-computed tomography contrast agents. Chem Rev 2013;113:1641–66.
[37] Lee N, Choi SH, Hyeon T. Nano-sized CT contrast agents. Adv Mater 2013;25:2641–60.
[38] Hu F, Zhao YS. Inorganic nanoparticle-based T1 and T1/T2 magnetic resonance contrast probes. Nanoscale 2012;4:6235–43.
[39] Singh SK. Red and near infrared persistent luminescence nanoprobes for bioimaging and targeting applications. RSC Adv 2014;4:58674–98.
[40] Maldiney T, Bessière A, Seguin J, et al. The *in vivo* activation of persistent nanophosphors for optical imaging of vascularization, tumours and grafted cells. Nat Mater 2014;13:418–26.
[41] Matijevic E. Preparation and properties of uniform size colloids. Chem Mat 1993;5:412–26.
[42] Jiang X, Cao C, Feng W, Li F. Nd^{3+}-doped $LiYF_4$ nanocrystals for bio-imaging in the second near-infrared window. J Mater Chem B 2016;4:87–95.
[43] Zhengquan L, Yong Z. An efficient and user-friendly method for the synthesis of hexagonal-phase $NaYF_4$:Yb, Er/Tm nanocrystals with controllable shape and upconversion fluorescence. Nanotechnology 2008;19:345606.
[44] Rodríguez-Liviano S, Becerro AI, Alcántara D, Grazú V, de la Fuente JM, Ocaña M. Synthesis and properties of multifunctional tetragonal Eu:$GdPO_4$ nanocubes for optical and magnetic resonance imaging applications. Inorg Chem 2013;52:647–54.
[45] Núñez NO, Ocaña M. An ionic liquid based synthesis method for uniform luminescent lanthanide fluoride nanoparticles. Nanotechnology 2007;18:455606.

[46] Escudero A, Calvo ME, Rivera-Fernández S, de la Fuente JM, Ocaña M. Microwave-assisted synthesis of biocompatible europium-doped calcium hydroxyapatite and fluoroapatite luminescent nanospindles functionalized with poly(acrylic acid). Langmuir 2013;29:1985–94.
[47] Shi J, Sun X, Zhu J, Li J, Zhang H. One-step synthesis of amino-functionalized ultrasmall near infrared-emitting persistent luminescent nanoparticles for *in vitro* and *in vivo* bioimaging. Nanoscale 2016;8:9798–804.
[48] Wu Y, Li C, Yang D, Lin J. Rare earth β-$NaGdF_4$ fluorides with multiform morphologies: hydrothermal synthesis and luminescent properties. J Colloid Interface Sci 2011;354:429–36.
[49] Yang D, Kang X, Shang M, et al. Size and shape controllable synthesis and luminescent properties of $BaGdF_5:Ce^{3+}/Ln^{3+}$ (Ln = Sm, Dy, Eu, Tb) nano/submicrocrystals by a facile hydrothermal process. Nanoscale 2011;3:2589–95.
[50] Wang X, Zhuang J, Peng Q, Li Y. Hydrothermal synthesis of rare-earth fluoride nanocrystals. Inorg Chem 2006;45:6661–5.
[51] Becerro AI, Criado J, Gontard LC, et al. Bifunctional, monodisperse $BiPO_4$-based nanostars: photocatalytic activity and luminescent applications. Cryst Growth Des 2014;14:3319–26.
[52] Escudero A, Carrillo-Carrión C, Zyuzin MV, et al. Synthesis and functionalization of monodisperse near-ultraviolet and visible excitable multifunctional Eu^{3+}, Bi^{3+}:$REVO_4$ nanophosphors for bioimaging and biosensing applications. Nanoscale 2016;8:12221–36.
[53] Zeng S, Tsang M-K, Chan C-F, Wong K-L, Fei B, Hao J. Dual-modal fluorescent/magnetic bioprobes based on small sized upconversion nanoparticles of amine-functionalized $BaGdF_5$:Yb/Er. Nanoscale 2012;4:5118–24.
[54] Rodríguez-Liviano S, Núñez NO, Rivera-Fernández S, de la Fuente JM, Ocaña M. Ionic liquid mediated synthesis and surface modification of multifunctional mesoporous Eu:GdF_3 nanoparticles for biomedical applications. Langmuir 2013;29:3411–8.
[55] Li Q, Yam VW-W. Redox luminescence switch based on energy transfer in $CePO_4:Tb^{3+}$ nanowires. Angew Chem Int Edit 2007;46:3486–9.
[56] Feng W, Yong Z, Xianping F, Minquan W. One-pot synthesis of chitosan/$LaF_3:Eu^{3+}$ nanocrystals for bio-applications. Nanotechnology 2006;17:1527.
[57] Stouwdam JW, van Veggel FCJM. Near-infrared emission of redispersible Er^{3+}, Nd^{3+}, and Ho^{3+} doped LaF_3 nanoparticles. Nano Lett 2002;2:733–7.
[58] Yuebin L, Zhong S, Lun M, et al. Synthesis and luminescence of $CePO_4$:Tb/$LaPO_4$ core/sheath nanowires. Nanotechnology 2010;21:125604.
[59] Buissette V, Moreau M, Gacoin T, Boilot J-P, Chane-Ching J-Y, Le Mercier T. Colloidal synthesis of luminescent rhabdophane $LaPO_4:Ln^{3+} \cdot xH_2O$ (Ln = Ce, Tb, Eu; x≈0.7) nanocrystals. Chem Mat 2004;16:3767–73.
[60] Yan Z-G, Yan C-H. Controlled synthesis of rare earth nanostructures. J Mater Chem 2008;18:5046–59.
[61] Mai H-X, Zhang Y-W, Sun L-D, Yan C-H. Orderly aligned and highly luminescent monodisperse rare-earth orthophosphate nanocrystals synthesized by a limited anion-exchange reaction. Chem Mat 2007;19:4514–22.
[62] Li J, Bu W, Guo L, Chen Z, Chen F, Shi J. Facile synthesis of size-tunable lanthanum phosphate nanocrystals monodispersible in both organic and aqueous solutions. J Mater Res 2011;23:2796–803.
[63] Wong H-T, Vetrone F, Naccache R, Chan HLW, Hao J, Capobianco JA. Water dispersible ultra-small multifunctional $KGdF_4:Tm^{3+}$, Yb^{3+} nanoparticles with near-infrared to near-infrared upconversion. J Mater Chem 2011;21:16589–96.
[64] Núñez NO, Rivera S, Alcántara D, de la Fuente JM, García-Sevillano J, Ocaña M. Surface modified Eu:$GdVO_4$ nanocrystals for optical and MRI imaging. Dalton Trans 2013;42:10725–34.
[65] Wang X, Zhuang J, Peng Q, Li Y. A general strategy for nanocrystal synthesis. Nature 2005;437:121–4.
[66] Wang Z, Ananias D, Carné-Sánchez A, et al. Lanthanide–organic framework nanothermometers prepared by spray-drying. Adv Funct Mater 2015;25:2824–30.
[67] Wilhelm S, Kaiser M, Wurth C, et al. Water dispersible upconverting nanoparticles: effects of surface modification on their luminescence and colloidal stability. Nanoscale 2015;7:1403–10.
[68] Ouyang J, Yin D, Cao X, et al. Synthesis of $NaLuF_4$-based nanocrystals and large enhancement of upconversion luminescence of $NaLuF_4$:Gd, Yb, Er by coating an active shell for bioimaging. Dalton Trans 2014;43:14001–8.
[69] Murali G, Lee BH, Mishra RK, et al. Synthesis, luminescence properties, and growth mechanisms of $YF_3:Yb^{3+}/Er^{3+}$ nanoplates. J Mater Chem C 2015;3:10107–13.
[70] Zheng K, He G, Song W, Bi X, Qin W. A strategy for enhancing the sensitivity of optical thermometers in β-$NaLuF_4:Yb^{3+}/Er^{3+}$ nanocrystals. J Mater Chem C 2015;3:11589–94.
[71] Dühnen S, Rinkel T, Haase M. Size control of nearly monodisperse β-$NaGdF_4$ particles prepared from small α-$NaGdF_4$ nanocrystals. Chem Mat 2015;27:4033–9.
[72] Zhang Y, Liu X, Lang Y, et al. Synthesis of ultra-small $BaLuF_5:Yb^{3+}$, Er^{3+}@$BaLuF_5:Yb^{3+}$ active-core-active-shell nanoparticles with enhanced up-conversion and down-conversion luminescence by a layer-by-layer strategy. J Mater Chem C 2015;3:2045–53.
[73] Zhang Y-W, Sun X, Si R, You L-P, Yan C-H. Single-crystalline and monodisperse LaF_3 triangular nanoplates from a single-source precursor. J Am Chem Soc 2005;127:3260–1.
[74] Naccache R, Vetrone F, Mahalingam V, Cuccia LA, Capobianco JA. Controlled synthesis and water dispersibility of hexagonal phase $NaGdF_4:Ho^{3+}/Yb^{3+}$ nanoparticles. Chem Mat 2009;21:717–23.
[75] Boyer J-C, Vetrone F, Cuccia LA, Capobianco JA. Synthesis of colloidal upconverting $NaYF_4$ nanocrystals doped with Er^{3+}, Yb^{3+} and Tm^{3+}, Yb^{3+} via thermal decomposition of lanthanide trifluoroacetate precursors. J Am Chem Soc 2006;128:7444–5.
[76] Sarkar S, Meesaragandla B, Hazra C, Mahalingam V. Sub-5 nm Ln^{3+}-doped $BaLuF_5$ nanocrystals: a platform to realize upconversion via interparticle energy transfer (IPET). Adv Mater 2013;25:856–60.
[77] Yang D, Dai Y, Liu J, et al. Ultra-small $BaGdF_5$-based upconversion nanoparticles as drug carriers and multimodal imaging probes. Biomaterials 2014;35:2011–23.
[78] Banski M, Podhorodecki A, Misiewicz J. $NaYF_4$ nanocrystals with TOPO ligands: synthesis-dependent structural and luminescent properties. Phys Chem Chem Phys 2013;15:19232–41.
[79] Shan J, Qin X, Yao N, Ju Y. Synthesis of monodisperse hexagonal $NaYF_4$:Yb, Ln (Ln = Er, Ho and Tm) upconversion nanocrystals in TOPO. Nanotechnology 2007;18:445607.

[80] Yi GS, Chow GM. Synthesis of hexagonal-phase $NaYF_4$:Yb, Er and $NaYF_4$:Yb, Tm nanocrystals with efficient up-conversion fluorescence. Adv Funct Mater 2006;16:2324–9.
[81] Liu Q, Sun Y, Yang T, Feng W, Li C, Li F. Sub-10 nm hexagonal lanthanide-doped $NaLuF_4$ upconversion nanocrystals for sensitive bioimaging *in vivo*. J Am Chem Soc 2011;133:17122–5.
[82] Mimun LC, Ajithkumar G, Pokhrel M, et al. Bimodal imaging using neodymium doped gadolinium fluoride nanocrystals with near-infrared to near-infrared downconversion luminescence and magnetic resonance properties. J Mater Chem B 2013;1:5702–10.
[83] Muhr V, Wilhelm S, Hirsch T, Wolfbeis OS. Upconversion nanoparticles: from hydrophobic to hydrophilic surfaces. Acc Chem Res 2014;47:3481–93.
[84] Feldmann C. Polyol-mediated synthesis of nanoscale functional materials. Adv Funct Mater 2003;13:101–7.
[85] Núñez NO, Míguez H, Quintanilla M, Cantelar E, Cussó F, Ocaña M. Synthesis of spherical down- and up-conversion $NaYF_4$-based nanophosphors with tunable size in ethylene glycol without surfactants or capping additives. Eur J Inorg Chem 2008;2008:4517–24.
[86] Núñez N, Sabek J, García-Sevillano J, Cantelar E, Escudero A, Ocaña M. Solvent-controlled synthesis and luminescence properties of uniform Eu:YVO_4 nanophosphors with different morphologies. Eur J Inorg Chem 2013;2013:1301–9.
[87] Rodríguez-Liviano S, Aparicio FJ, Rojas TC, Hungría AB, Chinchilla LE, Ocaña M. Microwave-assisted synthesis and luminescence of mesoporous RE-doped YPO_4 (RE = Eu, Ce, Tb, and Ce + Tb) nanophosphors with lenticular shape. Cryst Growth Des 2012;12:635–45.
[88] Becerro AI, Ocana M. Quick synthesis, functionalization and properties of uniform, luminescent $LuPO_4$-based nanoparticles. RSC Adv 2015;5:34517–24.
[89] Laguna M, Núñez NO, Rodríguez V, et al. Multifunctional Eu-doped $NaGd(MoO_4)_2$ nanoparticles functionalized with poly(l-lysine) for optical and MRI imaging. Dalton Trans 2016;45:16354–65.
[90] Núñez NO, Zambrano P, García-Sevillano J, et al. Uniform poly(acrylic acid)-functionalized lanthanide-doped $LaVO_4$ nanophosphors with high colloidal stability and biocompatibility. Eur J Inorg Chem 2015;2015:4546–54.
[91] Wu X, Zhang Q, Wang X, Yang H, Zhu Y. One-pot synthesis of carboxyl-functionalized rare earth fluoride nanocrystals with monodispersity, ultrasmall size and very bright luminescence. Eur J Inorg Chem 2011;2011:2158–63.
[92] Escudero A, Moretti E, Ocaña M. Synthesis and luminescence of uniform europium-doped bismuth fluoride and bismuth oxyfluoride particles with different morphologies. CrystEngComm 2014;16:3274–83.
[93] Jacob DS, Bitton L, Grinblat J, Felner I, Koltypin Y, Gedanken A. Are ionic liquids really a boon for the synthesis of inorganic materials? A general method for the fabrication of nanosized metal fluorides. Chem Mat 2006;18:3162–8.
[94] Antonietti M, Kuang D, Smarsly B, Zhou Y. Ionic liquids for the convenient synthesis of functional nanoparticles and other inorganic nanostructures. Angew Chem Int Edit 2004;43:4988–92.
[95] Klingshirn MA, Spear SK, Holbrey JD, Rogers RD. Ionic liquids as solvent and solvent additives for the synthesis of sol-gel materials. J Mater Chem 2005;15:5174–80.
[96] Lorbeer C, Cybińska J, Mudring A-V. Europium(III) fluoride nanoparticles from ionic liquids: structural, morphological, and luminescent properties. Cryst Growth Des 2011;11:1040–8.
[97] Liu L, Li R, Deng Y, et al. Solvothermal synthesis and luminescent properties of highly uniform LuF_3:Ln^{3+} (Ln = Eu, Tb, Dy) nanocrystals from ionic liquids. Appl Surf Sci 2014;307:393–400.
[98] Becerro AI, González-Mancebo D, Cantelar E, et al. Ligand-free synthesis of tunable size Ln:$BaGdF_5$ (Ln = Eu^{3+} and Nd^{3+}) nanoparticles: luminescence, magnetic properties, and biocompatibility. Langmuir 2016;32:411–20.
[99] Rabenau A. The role of hydrothermal synthesis in preparative chemistry. Angew Chem Int Ed Engl 1985;24:1026–40.
[100] Schäf O, Ghobarkar H, Knauth P. Hydrothermal synthesis of nanomaterials. In: Knauth P, Schoonman J, eds. Nanostructured materials: selected synthesis methods properties and applications. Boston, MA, Springer US, 2002, 23–41.
[101] Zhang F, Zhao D. Synthesis of uniform rare earth fluoride ($NaMF_4$) nanotubes by in situ ion exchange from their hydroxide [$M(OH)_3$] parents. ACS Nano 2009;3:159–64.
[102] Xu P, Yu R, Zong L, et al. Phase evolution and photoluminescence enhancement of $CePO_4$ nanowires from a low phosphate concentration system. J Nanopart Res 2013;15:1–8.
[103] Fang Y-P, Xu A-W, Song R-Q, et al. Systematic synthesis and characterization of single-crystal lanthanide orthophosphate nanowires. J Am Chem Soc 2003;125:16025–34.
[104] Komban R, Beckmann R, Rode S, et al. Surface modification of luminescent lanthanide phosphate nanorods with cationic "quat-primer" polymers. Langmuir 2011;27:10174–83.
[105] Lin H, Xu D, Li A, Teng D, Yang S, Zhang Y. Simultaneous realization of structure manipulation and emission enhancement in $NaLuF_4$ upconversion crystals. J Mater Chem C 2015;3:11754–65.
[106] Zhao Q, Lei Z, Huang S, et al. Facile fabrication of single-phase multifunctional $BaGdF_5$ nanospheres as drug carriers. ACS Appl Mater Interfaces 2014;6:12761–70.
[107] Li C, Hou Z, Zhang C, et al. Controlled synthesis of Ln^{3+} (Ln = Tb, Eu, Dy) and V^{5+} ion-doped YPO_4 nano-/microstructures with tunable luminescent colors. Chem Mat 2009;21:4598–607.
[108] Zhang L, Fu L, Yang X, Fu Z, Qi X, Wu Z. Controlled synthesis and tunable luminescence of uniform $YPO_4 \cdot 0.8H_2O$ and $YPO_4 \cdot 0.8H_2O$:Tb^{3+}/Eu^{3+} nanocrystals by a facile approach. J Mater Chem C 2014;2:9149–58.
[109] Rao L, Lu W, Zeng T, et al. One-pot synthesis of PEG modified $BaLuF_5$:Gd/Yb/Er nanoprobes for dual-modal *in vivo* upconversion luminescence and X-ray bioimaging. Dalton Trans 2014;43:13343–8.
[110] Li F, Li C, Liu X, et al. Hydrophilic, upconverting, multicolor, lanthanide-doped $NaGdF_4$ nanocrystals as potential multifunctional bioprobes. Chem Eur J 2012;18:11641–6.
[111] Ju Q, Tu D, Liu Y, et al. Amine-functionalized lanthanide-doped $KGdF_4$ nanocrystals as potential optical/magnetic multimodal bioprobes. J Am Chem Soc 2012;134:1323–30.
[112] Ren W, Tian G, Zhou L, et al. Lanthanide ion-doped $GdPO_4$ nanorods with dual-modal bio-optical and magnetic resonance imaging properties. Nanoscale 2012;4:3754–60.
[113] Wang L, Li P, Li Y. Down- and up-conversion luminescent nanorods. Adv Mater 2007;19:3304–7.

[114] Chen D, Yu Y, Huang F, Yang A, Wang Y. Lanthanide activator doped $NaYb_{1-x}Gd_xF_4$nanocrystals with tunable down-, up-conversion luminescence and paramagnetic properties. J Mater Chem 2011;21:6186–92.
[115] Tian Y, Yang H-Y, Li K, Jin X. Monodispersed ultrathin GdF_3 nanowires: oriented attachment, luminescence, and relaxivity for MRI contrast agents. J Mater Chem 2012;22:22510–6.
[116] Huo Z, Chen C, Li Y. Self-assembly of uniform hexagonal yttrium phosphate nanocrystals. Chem Commun 2006:3522–4.
[117] Huo Z, Chen C, Chu D, Li H, Li Y. Systematic synthesis of lanthanide phosphate nanocrystals. Chem-Eur J 2007;13:7708–14.
[118] Maldiney T, Richard C, Seguin J, Wattier N, Bessodes M, Scherman D. Effect of core diameter, surface coating, and PEG chain length on the biodistribution of persistent luminescence nanoparticles in mice. ACS Nano 2011;5:854–62.
[119] Abdukayum A, Chen J-T, Zhao Q, Yan X-P. Functional near infrared-emitting Cr^{3+}/Pr^{3+} Co-doped zinc gallogermanate persistent luminescent nanoparticles with superlong afterglow for *in vivo* targeted bioimaging. J Am Chem Soc 2013;135:14125–33.
[120] Cheng B, Fang L, Zhang Z, Xiao Y, Lei S. $BaAl_2O_4:Eu^{2+}$, Dy^{3+} nanotube synthesis by heating conversion of homogeneous coprecipitates and afterglow characteristics. J Phys Chem C 2011;115:1708–13.
[121] Cheng B, Liu H, Fang M, Xiao Y, Lei S, Zhang L. Long-persistent phosphorescent $SrAl_2O_4:Eu^{2+}$, Dy^{3+} nanotubes. Chem Commun 2009:944–6.
[122] Zhan-Jun L, Hong-Wu Z, Meng S, Jiang-Shan S, Hai-Xia F. A facile and effective method to prepare long-persistent phosphorescent nanospheres and its potential application for *in vivo* imaging. J Mater Chem 2012;22:24713–20.
[123] Shi J, Sun X, Li J, et al. Multifunctional near infrared-emitting long-persistence luminescent nanoprobes for drug delivery and targeted tumor imaging. Biomaterials 2015;37:260–70.
[124] Amendola V, Meneghetti M. What controls the composition and the structure of nanomaterials generated by laser ablation in liquid solution? Phys Chem Chem Phys 2013;15:3027–46.
[125] Yoshimura F, Nakamura K, Wakai F, et al. Preparation of long-afterglow colloidal solution of $Sr_2MgSi_2O_7$: Eu^{2+}, Dy^{3+} by laser ablation in liquid. Appl Surf Sci 2011;257:2170–5.
[126] Maldiney T, Sraiki G, Viana B, et al. *In vivo* optical imaging with rare earth doped $Ca_2Si_5N_8$ persistent luminescence nanoparticles. Opt Mater Express 2012;2:261–8.
[127] Wu J, Zhang H, Du S. Tunable luminescence and white light emission of mixed lanthanide-organic frameworks based on polycarboxylate ligands. J Mater Chem C 2016;4:3364–74.
[128] Stock N, Biswas S. Synthesis of metal-organic frameworks (MOFs): routes to various MOF topologies, morphologies, and composites. Chem Rev 2012;112:933–69.
[129] Devic T, Serre C, Audebrand N, Marrot J, Férey G. MIL-103, A 3-D lanthanide-based metal organic framework with large one-dimensional tunnels and a high surface area. J Am Chem Soc 2005;127:12788–9.
[130] Yao Q, Bermejo Gómez A, Su J, et al. Series of highly stable isoreticular lanthanide metal–organic frameworks with expanding pore size and tunable luminescent properties. Chem Mat 2015;27:5332–9.
[131] Xu H, Hu H-C, Cao C-S, Zhao B. Lanthanide organic framework as a regenerable luminescent probe for Fe^{3+}. Inorg Chem 2015;54:4585–7.
[132] Fang W-H, Yang G-Y. Syntheses and structures of three heterometallic coordination polymers derived from 4-pyridin-3-yl-benzoic acid. J Solid State Chem 2014;212:249–57.
[133] Zurawski A, Mai M, Baumann D, Feldmann C, Muller-Buschbaum K. Homoleptic imidazolate frameworks $3\,{}^{\infty}[Sr_{1-x}Eu_x(Im)_2]$-hybrid materials with efficient and tuneable luminescence. Chem Commun 2011;47:496–8.
[134] Bag PP, Wang X-S, Cao R. Microwave-assisted large scale synthesis of lanthanide metal-organic frameworks (Ln-MOFs), having a preferred conformation and photoluminescence properties. Dalton Trans 2015;44:11954–62.
[135] de Lill DT, Gunning NS, Cahill CL. Toward templated metal-organic frameworks: synthesis, structures, thermal properties, and luminescence of three novel lanthanide-adipate frameworks. Inorg Chem 2005;44:258–66.
[136] Bang JH, Suslick KS. Applications of ultrasound to the synthesis of nanostructured materials. Adv Mater 2010;22:1039–59.
[137] Khan NA, Haque MM, Jhung SH. Accelerated syntheses of porous isostructural lanthanide–benzenetricarboxylates (Ln–BTC) under ultrasound at room temperature. Eur J Inorg Chem 2010;2010:4975–81.
[138] Yuan W, O'Connor J, James SL. Mechanochemical synthesis of homo- and hetero-rare-earth(III) metal-organic frameworks by ball milling. CrystEngComm 2010;12:3515–7.
[139] Lan Y-Q, Jiang H-L, Li S-L, Xu Q. Mesoporous metal-organic frameworks with size-tunable cages: selective CO_2 uptake, encapsulation of Ln^{3+} cations for luminescence, and column-chromatographic dye separation. Adv Mater 2011;23:5015–20.
[140] Liu Y, Ai K, Liu J, Yuan Q, He Y, Lu L. A high-performance ytterbium-based nanoparticulate contrast agent for *in vivo* X-ray computed tomography imaging. Angew Chem-Int Edit 2012;51:1437–42.
[141] Escudero A, Carrillo-Carrión C, Zyuzin MV, Parak WJ. Luminescent rare-earth-based nanoparticles: a summarized overview of their synthesis, functionalization, and applications. Top Curr Chem 2016;374:48.
[142] Bogdan N, Vetrone F, Ozin GA, Capobianco JA. Synthesis of ligand-free colloidally stable water dispersible brightly luminescent lanthanide-doped upconverting nanoparticles. Nano Lett 2011;11:835–40.
[143] Wang M, Liu J-L, Zhang Y-X, Hou W, Wu X-L, Xu S-K. Two-phase solvothermal synthesis of rare-earth doped $NaYF_4$ upconversion fluorescent nanocrystals. Mater Lett 2009;63:325–7.
[144] Chen Z, Chen H, Hu H, et al. Versatile synthesis strategy for carboxylic acid-functionalized upconverting nanophosphors as biological labels. J Am Chem Soc 2008;130:3023–9.
[145] Dong A, Ye X, Chen J, et al. A generalized ligand-exchange strategy enabling sequential surface functionalization of colloidal nanocrystals. J Am Chem Soc 2011;133:998–1006.
[146] Li L-L, Zhang R, Yin L, et al. Biomimetic surface engineering of lanthanide-doped upconversion nanoparticles as versatile bioprobes. Angew Chem-Int Edit 2012;51:6121–5.
[147] Jiang G, Pichaandi J, Johnson NJJ, Burke RD, van Veggel FCJM. An effective polymer cross-linking strategy to obtain stable dispersions of upconverting $NaYF_4$ nanoparticles in buffers and biological growth media for biolabeling applications. Langmuir 2012;28:3239–47.
[148] Deng M, Tu N, Bai F, Wang L. Surface functionalization of hydrophobic nanocrystals with one particle per micelle for bioapplications. Chem Mat 2012;24:2592–7.

[149] Carrillo-Carrión C, Parak WJ. Design of pyridyl-modified amphiphilic polymeric ligands: towards better passivation of water-soluble colloidal quantum dots for improved optical performance. J Colloid Interface Sci 2016;478:88–96.
[150] Zhang F, Lees E, Amin F, et al. Polymer-coated nanoparticles: a universal tool for biolabelling experiments. Small 2011;7:3113–27.
[151] Nuñez NO, García M, García-Sevillano J, Rivera-Fernández S, de la Fuente JM, Ocaña M. One-step synthesis and polyacrylic acid functionalization of multifunctional europium-doped $NaGdF_4$ nanoparticles with selected size for optical and MRI imaging. Eur J Inorg Chem 2014;2014:6075–84.
[152] Schneider G, Decher G. Functional core/shell nanoparticles via layer-by-layer assembly. investigation of the experimental parameters for controlling particle aggregation and for enhancing dispersion stability. Langmuir 2008;24:1778–89.
[153] Wang L, Yan R, Huo Z, et al. Fluorescence resonant energy transfer biosensor based on upconversion-luminescent nanoparticles. Angew Chem-Int Edit 2005;44:6054–7.
[154] Guerrero-Martínez A, Pérez-Juste J, Liz-Marzán LM. Recent progress on silica coating of nanoparticles and related nanomaterials. Adv Mater 2010;22:1182–95.
[155] Liu J-N, Bu W-B, Shi J-L. Silica coated upconversion nanoparticles: a versatile platform for the development of efficient theranostics. Acc Chem Res 2015;48:1797–805.
[156] Knopp D, Tang D, Niessner R. Review: bioanalytical applications of biomolecule-functionalized nanometer-sized doped silica particles. Anal Chim Acta 2009;647:14–30.
[157] Stöber W, Fink A, Bohn E. Controlled growth of monodisperse silica spheres in the micron size range. J Colloid Interface Sci 1968;26:62–9.
[158] Gai S, Yang P, Li C, et al. Synthesis of magnetic, up-conversion luminescent, and mesoporous core–shell-structured nanocomposites as drug carriers. Adv Funct Mater 2010;20:1166–72.
[159] Mader HS, Link M, Achatz DE, Uhlmann K, Li X, Wolfbeis OS. Surface-modified upconverting microparticles and nanoparticles for use in click chemistries. Chem-Eur J 2010;16:5416–24.
[160] Maldiney T, Viana B, Bessière A, et al. *In vivo* imaging with persistent luminescence silicate-based nanoparticles. Opt Mater 2013;35:1852–8.
[161] Hu H, Xiong L, Zhou J, Li F, Cao T, Huang C. Multimodal-luminescence core–shell nanocomposites for targeted imaging of tumor cells. Chem-Eur J 2009;15:3577–84.
[162] Darbandi M, Nann T. One-pot synthesis of YF_3@silica core/shell nanoparticles. Chem Commun 2006:776–8.
[163] Ehlert O, Thomann R, Darbandi M, Nann T. A four-color colloidal multiplexing nanoparticle system. ACS Nano 2008;2:120–4.
[164] Li C, Yang D, Ma Pa, et al. Multifunctional upconversion mesoporous silica nanostructures for dual modal imaging and *in vivo* drug delivery. Small 2013;9:4150–9.
[165] Li C, Hou Z, Dai Y, et al. A facile fabrication of upconversion luminescent and mesoporous core-shell structured β-$NaYF_4$:Yb^{3+}, Er^{3+}@$mSiO_2$ nanocomposite spheres for anti-cancer drug delivery and cell imaging. Biomater Sci 2013;1:213–23.
[166] Liu G, Jacquier BJ, Eds. Spectroscopic properties of rare earths in optical materials. Springer Berlin Heidelberg, 2005.
[167] Richardson FS. Terbium(III) and europium(III) ions as luminescent probes and stains for biomolecular systems. Chem Rev 1982;82:541–52.
[168] Liping L, Minglei Z, Wenming T, Xiangfeng G, Guangshe L, Liusai Y. Preparation of cereal-like YVO_4:$Ln3^+$ (Ln = Sm, Eu, Tb, Dy) for high quantum efficiency photoluminescence. Nanotechnology 2010;21:195601.
[169] Eliseeva SV, Bunzli J-CG. Lanthanide luminescence for functional materials and bio-sciences. Chem Soc Rev 2010;39:189–227.
[170] Riedinger A, Zhang F, Dommershausen F, et al. Ratiometric optical sensing of chloride ions with organic fluorophore-gold nanoparticle hybrids: a systematic study of design parameters and surface charge effects. Small 2010;6:2590–7.
[171] Pandey A, Roy MK, Pandey A, et al. Chloroform- and water-soluble sol-gel derived Eu^{3+}/Y_2O_3 (red) and Tb^{3+}/Y_2O_3 (green) nanophosphors: synthesis, characterisation and surface modification. IEEE Trans Nanobiosci 2009;8:43–50.
[172] Bunzli J-CG, Piguet C. Taking advantage of luminescent lanthanide ions. Chem Soc Rev 2005;34:1048–77.
[173] Zhou B, Shi B, Jin D, Liu X. Controlling upconversion nanocrystals for emerging applications. Nat Nanotechnol 2015;10:924–36.
[174] Auzel F. Upconversion and anti-Stokes processes with f and d ions in solids. Chem Rev 2004;104:139–74.
[175] Chen G, Qiu H, Prasad PN, Chen X. Upconversion nanoparticles: design, nanochemistry, and applications in theranostics. Chem Rev 2014;114:5161–214.
[176] Krämer KW, Biner D, Frei G, Güdel HU, Hehlen MP, Lüthi SR. Hexagonal sodium yttrium fluoride based green and blue emitting upconversion phosphors. Chem Mat 2004;16:1244–51.
[177] Zheng W, Zhou S, Chen Z, et al. Sub-10 nm lanthanide-doped CaF_2 nanoprobes for time-resolved luminescent biodetection. Angew Chem-Int Edit 2013;52:6671–6.
[178] Wang Z-L, Chan HLW, Li H-L, Hao JH. Highly efficient low-voltage cathodoluminescence of LaF_3:Ln^{3+} (Ln = Eu^{3+}, Ce^{3+}, Tb^{3+}) spherical particles. Appl Phys Lett 2008;93:141106–3.
[179] Epple M, Ganesan K, Heumann R, et al. Application of calcium phosphate nanoparticles in biomedicine. J Mater Chem 2010;20:18–23.
[180] Abdesselem M, Schoeffel M, Maurin I, et al. Multifunctional rare-earth vanadate nanoparticles: luminescent labels, oxidant sensors, and MRI contrast agents. ACS Nano 2014;8:11126–37.
[181] Zeng Y, Li Z, Wang L, Xiong Y. Controlled synthesis of $Gd_2(WO_4)_3$ microstructures and their tunable photoluminescent properties after Eu^{3+}/Tb^{3+} doping. CrystEngComm 2012;14:7043–8.
[182] Zhou Y, Yan B, He X-H. Controlled synthesis and up/down-conversion luminescence of self-assembled hierarchical architectures of monoclinic $AgRE(WO_4)_2$:Ln^{3+} (RE = Y, La, Gd, Lu; Ln = Eu, Tb, Sm, Dy, Yb/Er, Yb/Tm). J Mater Chem C 2014;2:848–55.
[183] Goncalves RF, Cavalcante LS, Nogueira IC, et al. Rietveld refinement, cluster modelling, growth mechanism and photoluminescence properties of $CaWO_4$:Eu^{3+} microcrystals. CrystEngComm 2015;17:1654–66.
[184] Kaczmarek AM, Van Deun R. Rare earth tungstate and molybdate compounds – from 0D to 3D architectures. Chem Soc Rev 2013;42:8835–48.

[185] Liu X, Li L, Noh HM, Jeong JH, Jang K, Shin DS. Controllable synthesis of uniform $CaMoO_4$:Eu^{3+}, M^+ (M = Li, Na, K) microspheres and optimum luminescence properties. RSC Adv 2015;5:9441–54.
[186] Lü Q, Guo F, Sun L, Li A, Zhao L. Silica-/titania-coated Y_2O_3:Tm^{3+}, Yb^{3+} nanoparticles with improvement in upconversion luminescence induced by different thickness shells. J Appl Phys 2008;103:123533.
[187] Kumar R, Nyk M, Ohulchanskyy TY, Flask CA, Prasad PN. Combined optical and MR bioimaging using rare earth ion doped $NaYF_4$ nanocrystals. Adv Funct Mater 2009;19:853–9.
[188] Boyer J-C, Manseau M-P, Murray JI, van Veggel FCJM. Surface modification of upconverting $NaYF_4$ nanoparticles with PEG-phosphate ligands for NIR (800 nm) biolabeling within the biological window. Langmuir 2010;26:1157–64.
[189] Wang F, Wang JA, Liu XG. Direct evidence of a surface quenching effect on size-dependent luminescence of upconversion nanoparticles. Angew Chem-Int Edit 2010;49:7456–60.
[190] Boyer J-C, van Veggel FCJM. Absolute quantum yield measurements of colloidal $NaYF_4$: Er^{3+}, Yb^{3+} upconverting nanoparticles. Nanoscale 2010;2:1417–9.
[191] Griesbeck AG. Essentials of molecular photochemistry. Von A. Gilbert und J. Baggott. Blackwell Scientific Publications, Oxford 1991. XII, 538 ISBN 0-632-02429-1. Angew Chem 1991;103:1554–5.
[192] Li C, Lin J. Rare earth fluoride nano-/microcrystals: synthesis, surface modification and application. J Mater Chem 2010;20:6831–47.
[193] Ostrowski AD, Chan EM, Gargas DJ, et al. Controlled synthesis and single-particle imaging of bright, sub-10 nm lanthanide-doped upconverting nanocrystals. ACS Nano 2012;6:2686–92.
[194] Ren J, Jia G, Guo Y, Wang A, Xu S. Unraveling morphology and phase control of $NaLnF_4$ upconverting nanocrystals. J Phys Chem C 2016;120:1342–51.
[195] Dong NN, Pedroni M, Piccinelli F, et al. NIR-to-NIR two-photon excited CaF_2: Tm^{3+}, Yb^{3+} nanoparticles: multifunctional nanoprobes for highly penetrating fluorescence bio-imaging. ACS Nano 2011;5:8665–71.
[196] Singh NS, Ningthoujam RS, Luwang MN, Singh SD, Vatsa RK. Luminescence, lifetime and quantum yield studies of YVO_4:Ln^{3+} (Ln^{3+} = Dy^{3+}, Eu^{3+}) nanoparticles: concentration and annealing effects. Chem Phys Lett 2009;480:237–42.
[197] Wawrzynczyk D, Nyk M, Bednarkiewicz A, Strek W, Samoc M. Morphology- and size-dependent spectroscopic properties of Eu^{3+}-doped Gd_2O_3 colloidal nanocrystals. J Nanopart Res 2014;16:1–13.
[198] Wisser MD, Chea M, Lin Y, et al. Strain-induced modification of optical selection rules in lanthanide-based upconverting nanoparticles. Nano Lett 2015;15:1891–7.
[199] Han S, Deng R, Xie X, Liu X. Enhancing luminescence in lanthanide-doped upconversion nanoparticles. Angew Chem-Int Edit 2014;53:11702–15.
[200] Li K, Shang M, Lian H, Lin J. Recent development in phosphors with different emitting colors via energy transfer. J Mater Chem C 2016;4:5507–30.
[201] Wang F, Xue X, Liu X. Multicolor tuning of (Ln, P)-doped YVO_4 nanoparticles by single-wavelength excitation. Angew Chem-Int Edit 2008;47:906–9.
[202] Lei F, Yan B. Hydrothermal synthesis and luminescence of $CaMO_4$:RE^{3+} (M = W, Mo; RE = Eu, Tb) submicro-phosphors. J Solid State Chem 2008;181:855–62.
[203] Su Y, Li L, Li G. Synthesis and optimum luminescence of $CaWO_4$-based red phosphors with codoping of Eu^{3+} and Na^+. Chem Mat 2008;20:6060–7.
[204] Gupta SK, Sahu M, Ghosh PS, Tyagi D, Saxena MK, Kadam RM. Energy transfer dynamics and luminescence properties of Eu^{3+} in $CaMoO_4$ and $SrMoO_4$. Dalton Trans 2015;44:18957–69.
[205] Becerro AI, Rodríguez-Liviano S, Fernández-Carrión AJ, Ocaña M. A novel 3D architecture of $GdPO_4$ nanophosphors: multicolored and white light emission. Cryst Growth Design 2013;13:526–35.
[206] Blasse G, Grabmaier BC. Luminescent materials. Berlin, Heidelberg, Springer, 1994.
[207] Blasse G, Bril A. Investigations on Bi^{3+}-activated phosphors. J Chem Phys 1968;48:217–22.
[208] Wang ZL, Quan ZW, Jia PY, et al. A facile synthesis and photoluminescent properties of redispersible CeF_3, CeF_3:Tb^{3+}, and CeF_3:Tb^{3+}/LaF_3 (core/shell) nanoparticles. Chem Mat 2006;18:2030–7.
[209] Shang M, Li C, Lin J. How to produce white light in a single-phase host? Chem Soc Rev 2014;43:1372–86.
[210] Xia Z, Liu R-S. Tunable blue-green color emission and energy transfer of $Ca_2Al_3O_6F$:Ce^{3+}, Tb^{3+} phosphors for near-UV white LEDs. J Phys Chem C 2012;116:15604–9.
[211] Huang C-H, Chen T-M. A novel single-composition trichromatic white-light $Ca_3Y(GaO)_3(BO_3)_4$:Ce^{3+}, Mn^{2+}, Tb^{3+} phosphor for UV-light emitting diodes. J Phys Chem C 2011;115:2349–55.
[212] Zhou H, Jin Y, Jiang M, Wang Q, Jiang X. A single-phased tunable emission phosphor $MgY_2Si_3O_{10}$: Eu^{3+}, Bi^{3+} with efficient energy transfer for white LEDs. Dalton Trans 2015;44:1102–9.
[213] Li K, Lian H, Shang M, Lin J. A novel greenish yellow-orange red $Ba_3Y_4O_9$:Bi^{3+}, Eu^{3+} phosphor with efficient energy transfer for UV-LEDs. Dalton Trans 2015;44:20542–50.
[214] Kang F, Zhang Y, Peng M. Controlling the energy transfer via multi luminescent centers to achieve white light/tunable emissions in a single-phased X2-type Y_2SiO_5:Eu^{3+}, Bi^{3+} phosphor for ultraviolet converted LEDs. Inorg Chem 2015;54:1462–73.
[215] Orihashi T, Nakamura T, Adachi S. Resonant energy transfer in (Eu^{3+}, Bi^{3+})-codoped $CaZrO_3$ red-emitting phosphor. RSC Adv 2016;6:66130–9.
[216] Parchur AK, Ningthoujam RS. Behaviour of electric and magnetic dipole transitions of Eu^{3+}, $^5D_0 \rightarrow {}^7F_0$ and Eu-O charge transfer band in Li^+ co-doped YPO_4:Eu^{3+}. RSC Adv 2012;2:10859–68.
[217] Gavrilović TV, Jovanović DJ, Smits K, Dramićanin MD. Multicolor upconversion luminescence of $GdVO_4$:Ln^{3+}/Yb^{3+} (Ln^{3+} = Ho^{3+}, Er^{3+}, Tm^{3+}, Ho^{3+}/Er^{3+}/Tm^{3+}) nanorods. Dyes Pigments 2016;126:1–7.
[218] Liu Q, Feng W, Yang T, Yi T, Li F. Upconversion luminescence imaging of cells and small animals. Nat Protoc 2013;8:2033–44.
[219] Weissleder R. A clearer vision for *in vivo* imaging. Nat Biotechnol 2001;19:316–7.
[220] Shen J, Chen G, Vu A-M, et al. Engineering the upconversion nanoparticle excitation wavelength: cascade sensitization of tri-doped upconversion colloidal nanoparticles at 800 nm. Adv Opt Mater 2013;1:644–50.

[221] Zhong Y, Tian G, Gu Z, et al. Elimination of photon quenching by a transition layer to fabricate a quenching-shield sandwich structure for 800 nm excited upconversion luminescence of Nd^{3+}-sensitized nanoparticles. Adv Mater 2014;26:2831–7.
[222] Xie X, Gao N, Deng R, Sun Q, Xu Q-H, Liu X. Mechanistic investigation of photon upconversion in Nd^{3+}-sensitized core–shell nanoparticles. J Am Chem Soc 2013;135:12608–11.
[223] Wang Y-F, Liu G-Y, Sun L-D, Xiao J-W, Zhou J-C, Yan C-H. Nd^{3+}-sensitized upconversion nanophosphors: efficient *in vivo* bioimaging probes with minimized heating effect. ACS Nano 2013;7:7200–6.
[224] Jia Z, Arcangeli A, Tao X, et al. Efficient $Nd^{3+} \rightarrow Yb^{3+}$ energy transfer in Nd^{3+}, Yb^{3+}:$Gd_3Ga_5O_{12}$ multicenter garnet crystal. J Appl Phys 2009;105:083113.
[225] Agbo P, Xu T, Sturzbecher-Hoehne M, Abergel RJ. Enhanced ultraviolet photon capture in ligand-sensitized nanocrystals. ACS Photonics 2016;3:547–52.
[226] Goetz J, Nonat A, Diallo A, et al. Ultrabright lanthanide nanoparticles. ChemPlusChem 2016;81:526–34.
[227] Zou W, Visser C, Maduro JA, Pshenichnikov MS, Hummelen JC. Broadband dye-sensitized upconversion of near-infrared light. Nat Photonics 2012;6:560–4.
[228] Chen G, Damasco J, Qiu H, et al. Energy-cascaded upconversion in an organic dye-sensitized core/shell fluoride nanocrystal. Nano Lett 2015;15:7400–7.
[229] Höller CJ, Matthes PR, Adlung M, Wickleder C, Müller-Buschbaum K. Antenna- and metal-triggered luminescence in dense 1,3-benzodinitrile metal–organic frameworks $\infty 3[LnCl_3(1,3\text{-}Ph(CN)_2)]$, Ln = Eu, Tb. Eur J Inorg Chem 2012;2012:5479–84.
[230] Zhang X, Ballem MA, Ahrén M, Suska A, Bergman P, Uvdal K. Nanoscale Ln(III)-carboxylate coordination polymers (Ln = Gd, Eu, Yb): temperature-controlled guest encapsulation and light harvesting. J Am Chem Soc 2010;132:10391–7.
[231] Zhang H, Li Y, Ivanov IA, Qu Y, Huang Y, Duan X. Plasmonic modulation of the upconversion fluorescence in $NaYF_4$:Yb/Tm hexaplate nanocrystals using gold nanoparticles or nanoshells. Angew Chem-Int Edit 2010;49:2865–8.
[232] Wang M, Mi C-C, Wang W-X, et al. Immunolabeling and NIR-excited fluorescent imaging of HeLa cells by using $NaYF_4$:Yb, Er upconversion nanoparticles. ACS Nano 2009;3:1580–6.
[233] Chen G, Ohulchanskyy TY, Liu S, et al. Core/shell $NaGdF_4$:Nd^{3+}/$NaGdF_4$ nanocrystals with efficient near-infrared to near-infrared downconversion photoluminescence for bioimaging applications. ACS Nano 2012;6:2969–77.
[234] Vetrone F, Naccache R, Mahalingam V, Morgan CG, Capobianco JA. The active-core/active-shell approach: a strategy to enhance the upconversion luminescence in lanthanide-doped nanoparticles. Adv Funct Mater 2009;19:2924–9.
[235] Dühnen S, Haase M. Study on the intermixing of core and shell in $NaEuF_4$/$NaGdF_4$ core/shell nanocrystals. Chem Mat 2015;27:8375–86.
[236] Chen G, Shen J, Ohulchanskyy TY, et al. (α-$NaYbF_4$:Tm^{3+})/CaF_2 core/shell nanoparticles with efficient near-infrared to near-infrared upconversion for high-contrast deep tissue bioimaging. ACS Nano 2012;6:8280–7.
[237] Zhang Y, Wang F, Lang Y, et al. $KMnF_3$:Yb^{3+}, Er^{3+}@$KMnF_3$:Yb^{3+} active-core-active-shell nanoparticles with enhanced red upconversion fluorescence for polymer-based waveguide amplifiers operating at 650 nm. J Mater Chem C 2015;3:9827–32.
[238] Li X, Wang R, Zhang F, Zhao D. Engineering homogeneous doping in single nanoparticle to enhance upconversion efficiency. Nano Lett 2014;14:3634–9.
[239] Ma D, Xu X, Hu M, et al. Rare-earth-based nanoparticles with simultaneously enhanced near-infrared (NIR)-visible (Vis) and NIR-NIR dual-conversion luminescence for multimodal imaging. Chem Asian J 2016;11:1050–8.
[240] Zhou J, Shirahata N, Sun H-T, et al. Efficient dual-modal NIR-to-NIR emission of rare earth ions co-doped nanocrystals for biological fluorescence imaging. J Phys Chem Lett 2013;4:402–8.
[241] Yao C, Wang P, Wang R, et al. Facile peptides functionalization of lanthanide-based nanocrystals through phosphorylation tethering for efficient *in vivo* NIR-to-NIR bioimaging. Anal Chem 2016;88:1930–6.
[242] Wu DM, García-Etxarri A, Salleo A, Dionne JA. Plasmon-enhanced upconversion. J Phys Chem Lett 2014;5:4020–31.
[243] Aslan K, Geddes CD. Metal-enhanced fluorescence: progress towards a unified plasmon-fluorophore description metal-enhanced fluorescence. John Wiley & Sons, Inc., 2010, 1–23.
[244] Ru ECL, Grand J, Félidj N, et al. Spectral profile modifications in metal-enhanced fluorescence metal-enhanced fluorescence. John Wiley & Sons, Inc., 2010, 25–65.
[245] Ross DJ, Pieczonka NPW, Aroca RF. The role of plasmonic engineering in potential surface-enhanced fluorescence metal-enhanced fluorescence. John Wiley & Sons, Inc., 2010, 67–90.
[246] Munechika K, Chen Y, Smith JM, Ginger DS. Importance of spectral overlap: fluorescence enhancement by single metal nanoparticles metal-enhanced fluorescence. John Wiley & Sons, Inc., 2010, 91–118.
[247] Sudheendra L, Ortalan V, Dey S, Browning ND, Kennedy IM. Plasmonic enhanced emissions from cubic $NaYF_4$:Yb:Er/Tm nanophosphors. Chem Mat 2011;23:2987–93.
[248] Kannan P, Abdul Rahim F, Chen R, et al. Au nanorod decoration on $NaYF_4$:Yb/Tm nanoparticles for enhanced emission and wavelength-dependent biomolecular sensing. ACS Appl Mater Interfaces 2013;5:3508–13.
[249] Rai M, Singh SK, Singh AK, et al. Enhanced red upconversion emission, magnetoluminescent behavior, and bioimaging application of $NaSc_{0.75}Er_{0.02}Yb_{0.18}Gd_{0.05}F_4$@AuNPs nanoparticles. ACS Appl Mater Interfaces 2015;7:15339–50.
[250] Saboktakin M, Ye X, Oh SJ, et al. Metal-enhanced upconversion luminescence tunable through metal nanoparticle–nanophosphor separation. ACS Nano 2012;6:8758–66.
[251] Dong B, Xu S, Sun J, et al. Multifunctional $NaYF_4$:Yb^{3+}, Er^{3+}@Ag core/shell nanocomposites: integration of upconversion imaging and photothermal therapy. J Mater Chem 2011;21:6193–200.
[252] Wang J, Huang H, Zhang D, et al. Synthesis of gold/rare-earth-vanadate core/shell nanorods for integrating plasmon resonance and fluorescence. Nano Res 2015;8:2548–61.
[253] Liu N, Qin W, Qin G, Jiang T, Zhao D. Highly plasmon-enhanced upconversion emissions from Au@β-$NaYF_4$:Yb, Tm hybrid nanostructures. Chem Commun 2011;47:7671–3.
[254] Fujii M, Nakano T, Imakita K, Hayashi S. Upconversion luminescence of Er and Yb codoped $NaYF_4$ nanoparticles with metal shells. J Phys Chem C 2013;117:1113–20.
[255] Zhang X, Li B, Jiang M, Zhang L, Ma H. Core-spacer-shell structured $NaGdF_4$:Yb^{3+}/Er^{3+}@$NaGdF_4$@Ag nanoparticles for plasmon-enhanced upconversion luminescence. RSC Adv 2016;6:36528–33.

[256] Qian LP, Zhou LH, Too H-P, Chow G-M. Gold decorated $NaYF_4$:Yb, Er/$NaYF_4$/silica (core/shell/shell) upconversion nanoparticles for photothermal destruction of BE(2)-C neuroblastoma cells. J Nanopart Res 2011;13:499–510.
[257] Li Y, Gecevicius M, Qiu J. Long persistent phosphors-from fundamentals to applications. Chem Soc Rev 2016;45:2090–136.
[258] Hemmer E, Benayas A, Legare F, Vetrone F. Exploiting the biological windows: current perspectives on fluorescent bioprobes emitting above 1000 nm. Nanoscale Horizons 2016;1:168–84.
[259] del Rosal B, Pérez-Delgado A, Carrasco E, et al. Neodymium-based stoichiometric ultrasmall nanoparticles for multifunctional deep-tissue photothermal therapy. Adv Opt Mater 2016;4:782–9.
[260] Abdul Jalil R, Zhang Y. Biocompatibility of silica coated $NaYF_4$ upconversion fluorescent nanocrystals. Biomaterials 2008;29:4122–8.
[261] Hu H, Yu M, Li F, et al. Facile epoxidation strategy for producing amphiphilic up-converting rare-earth nanophosphors as biological labels. Chem Mat 2008;20:7003–9.
[262] Chen Z, Wu X, Hu S, et al. Multicolor upconversion $NaLuF_4$ fluorescent nanoprobe for plant cell imaging and detection of sodium fluorescein. J Mater Chem C 2015;3:153–61.
[263] Chan C-F, Tsang M-K, Li H, et al. Bifunctional up-converting lanthanide nanoparticles for selective *in vitro* imaging and inhibition of cyclin D as anti-cancer agents. J Mater Chem B 2014;2:84–91.
[264] Bogdan N, Rodriguez EM, Sanz-Rodriguez F, et al. Bio-functionalization of ligand-free upconverting lanthanide doped nanoparticles for bio-imaging and cell targeting. Nanoscale 2012;4:3647–50.
[265] Grebenik EA, Nadort A, Generalova AN, et al. Feasibility study of the optical imaging of a breast cancer lesion labeled with upconversion nanoparticle biocomplexes. J Biomed Opt 2013;18:076004.
[266] Ong LC, Ang LY, Alonso S, Zhang Y. Bacterial imaging with photostable upconversion fluorescent nanoparticles. Biomaterials 2014;35:2987–98.
[267] Zhou J-C, Yang Z-L, Dong W, Tang R-J, Sun L-D, Yan C-H. Bioimaging and toxicity assessments of near-infrared upconversion luminescent $NaYF_4$:Yb, Tm nanocrystals. Biomaterials 2011;32:9059–67.
[268] Chatterjee DK, Rufaihah AJ, Zhang Y. Upconversion fluorescence imaging of cells and small animals using lanthanide doped nanocrystals. Biomaterials 2008;29:937–43.
[269] Yang T, Sun Y, Liu Q, Feng W, Yang P, Li F. Cubic sub-20 nm $NaLuF_4$-based upconversion nanophosphors for high-contrast bioimaging in different animal species. Biomaterials 2012;33:3733–42.
[270] Nordmann J, Buczka S, Voss B, Haase M, Mummenhoff K. *In vivo* analysis of the size- and time-dependent uptake of $NaYF_4$:Yb, Er upconversion nanocrystals by pumpkin seedlings. J Mater Chem B 2015;3:144–50.
[271] Xiong L, Yang T, Yang Y, Xu C, Li F. Long-term *in vivo* biodistribution imaging and toxicity of polyacrylic acid-coated upconversion nanophosphors. Biomaterials 2010;31:7078–85.
[272] Xiong L-Q, Chen Z-G, Yu M-X, Li F-Y, Liu C, Huang C-H. Synthesis, characterization, and *in vivo* targeted imaging of amine-functionalized rare-earth up-converting nanophosphors. Biomaterials 2009;30:5592–600.
[273] Yu X-F, Sun Z, Li M, et al. Neurotoxin-conjugated upconversion nanoprobes for direct visualization of tumors under near-infrared irradiation. Biomaterials 2010;31:8724–31.
[274] Cao T, Yang Y, Gao Y, Zhou J, Li Z, Li F. High-quality water-soluble and surface-functionalized upconversion nanocrystals as luminescent probes for bioimaging. Biomaterials 2011;32:2959–68.
[275] Ni D, Zhang J, Bu W, et al. Dual-targeting upconversion nanoprobes across the blood–brain barrier for magnetic resonance/fluorescence imaging of intracranial glioblastoma. ACS Nano 2014;8:1231–42.
[276] Xia A, Gao Y, Zhou J, et al. Core–shell $NaYF_4$:Yb^{3+}, Tm^{3+}@Fe_xO_y nanocrystals for dual-modality T2-enhanced magnetic resonance and NIR-to-NIR upconversion luminescent imaging of small-animal lymphatic node. Biomaterials 2011;32:7200–8.
[277] Zhou J, Sun Y, Du X, Xiong L, Hu H, Li F. Dual-modality *in vivo* imaging using rare-earth nanocrystals with near-infrared to near-infrared (NIR-to-NIR) upconversion luminescence and magnetic resonance properties. Biomaterials 2010;31:3287–95.
[278] Zhan Q, Qian J, Liang H, et al. Using 915 nm laser excited Tm^{3+}/Er^{3+}/Ho^{3+}-doped $NaYbF_4$ upconversion nanoparticles for *in vitro* and deeper *in vivo* bioimaging without overheating irradiation. ACS Nano 2011;5:3744–57.
[279] Brito HF, Hölsä J, Laamanen T, Lastusaari M, Malkamäki M, Rodrigues LCV. Persistent luminescence mechanisms: human imagination at work. Opt Mater Express 2012;2:371–81.
[280] Smet PF, Poelman D, Hehlen MP. Focus issue introduction: persistent phosphors. Opt Mater Express 2012;2:452–4.
[281] Yamamoto H, Matsuzawa T. Luminescence and optical spectroscopy of condensed mattermechanism of long phosphorescence of $SrAl_2O_4$:Eu^{2+}, Dy^{3+} and $CaAl_2O_4$:Eu^{2+}, Nd^{3+}. J Lumin 1997;72:287–9.
[282] Aitasalo T, Dereń P, Hölsä J, et al. Persistent luminescence phenomena in materials doped with rare earth ions. J Solid State Chem 171:114–22.
[283] Maldiney T, Lecointre A, Viana B, et al. Controlling electron trap depth to enhance optical properties of persistent luminescence nanoparticles for *in vivo* imaging. J Am Chem Soc 2011;133;11810–5.
[284] Paterson AS, Raja B, Garvey G, et al. Persistent luminescence strontium aluminate nanoparticles as reporters in lateral flow assays. Anal Chem 2014;86:9481–8.
[285] Dorenbos P. Energy of the first $4f^7 \rightarrow 4f^6 5d$ transition of Eu^{2+} in inorganic compounds. J Lumin 2003;104:239–60.
[286] Rosticher C, Viana B, Laurent G, Le Griel P, Chanéac C. Insight into $CaMgSi_2O_6$:Eu^{2+}, Mn^{2+}, Dy^{3+} nanoprobes: influence of chemical composition and crystallinity on persistent red luminescence. Eur J Inorg Chem 2015;2015:3681–7.
[287] Maldiney T, Scherman D, Richard C. Persistent luminescence nanoparticles for diagnostics and imaging. In: Functional Nanoparticles for Bioanalysis, Nanomedicine, and Bioelectronic Devices, Volume 2. ACS Symposium Series 2012; 1113:1–25, Washington DC.
[288] Van den Eeckhout K, Smet PF, Poelman D. Persistent luminescence in Eu^{2+}-doped compounds: a review. Materials 2010;3:2536.
[289] Smet PF, Botterman J, Van den Eeckhout K, Korthout K, Poelman D. Persistent luminescence in nitride and oxynitride phosphors: a review. Opt Mater 2014;36:1913–9.

[290] Smet PF, Moreels I, Hens Z, Poelman D. Luminescence in sulfides: a rich history and a bright future. Materials 2010;3:2834.
[291] Rodrigues LCV, Hölsä J, Carvalho JM, et al. Co-dopant influence on the persistent luminescence of $BaAl_2O_4:Eu^{2+}$, R^{3+}. Physica B 2014;439:67–71.
[292] Dai WB. Investigation of the luminescent properties of Ce^{3+} doped and Ce^{3+}/Mn^{2+} co-doped $CaAl_2Si_2O_8$ phosphors. RSC Adv 2014;4:11206–15.
[293] Ning L, Zhou C, Chen W, et al. Electronic properties of Ce^{3+}-Doped $Sr_3Al_2O_5Cl_2$: a combined spectroscopic and theoretical study. J Phys Chem C 2015;119:6785–92.
[294] Caratto V, Locardi F, Costa GA, et al. NIR persistent luminescence of lanthanide ion-doped rare-earth oxycarbonates: the effect of dopants. ACS Appl Mater Interfaces 2014;6:17346–51.
[295] Sunao K, Chao-Nan X, Hiroshi Y, Nao T, Masayoshi F. Long-persistent luminescence in the near-infrared from Nd^{3+}-doped Sr_2SnO_4 for *in vivo* optical imaging. Jpn J Appl Phys 2014;53:092403.
[296] Qin X, Li Y, Zhang R, et al. Hybrid coordination-network-engineering for bridging cascaded channels to activate long persistent phosphorescence in the second biological window. Sci Rep 2016;6:20275.
[297] Zou Z, Feng L, Cao C, Zhang J, Wang Y. Near-infrared quantum cutting long persistent luminescence. Sci Rep 2016;6:24884.
[298] Liang Y-J, Liu F, Chen Y-F, Wang X-J, Sun K-N, Pan Z. New function of the Yb^{3+} ion as an efficient emitter of persistent luminescence in the short-wave infrared. Light Sci Appl 2016;5:e16124.
[299] Liu F, Liang Y, Pan Z. Detection of up-converted persistent luminescence in the near infrared emitted by the $Zn_3Ga_2GeO_8:Cr^{3+}$, Yb^{3+}, Er^{3+} phosphor. Phys Rev Lett 2014;113:177401.
[300] Bashir MR, Bhatti L, Marin D, Nelson RC. Emerging applications for ferumoxytol as a contrast agent in MRI. J Magn Reson Imaging 2015;41:884–98.
[301] Rogosnitzky M, Branch S. Gadolinium-based contrast agent toxicity: a review of known and proposed mechanisms. BioMetals 2016;29:365–76.
[302] Li J, You J, Dai Y, Shi M, Han C, Xu K. Gadolinium oxide nanoparticles and aptamer-functionalized silver nanoclusters-based multimodal molecular imaging nanoprobe for optical/magnetic resonance cancer cell imaging. Anal Chem 2014;86:11306–11.
[303] Xing H, Zhang S, Bu W, et al. Ultrasmall $NaGdF_4$ nanodots for efficient MR angiography and atherosclerotic plaque imaging. Adv Mater 2014;26:3867–72.
[304] Johnson NJJ, Oakden W, Stanisz GJ, Scott Prosser R, van Veggel FCJM. Size-tunable, ultrasmall $NaGdF_4$ nanoparticles: insights into their T1 MRI contrast enhancement. Chem Mat 2011;23:3714–22.
[305] Wei X, Wang W, Chen K. Preparation and characterization of ZnS:Tb, Gd and ZnS:Er, Yb, Gd nanoparticles for bimodal magnetic-fluorescent imaging. Dalton Trans 2013;42:1752–9.
[306] Kang X, Yang D, Ma Pa, et al. Fabrication of hollow and porous structured $GdVO_4:Dy^{3+}$ nanospheres as anticancer drug carrier and MRI contrast agent. Langmuir 2013;29:1286–94.
[307] Caravan P, Ellison JJ, McMurry TJ, Lauffer RB. Gadolinium(III) chelates as MRI contrast agents: structure, dynamics, and applications. Chem Rev 1999;99:2293–352.
[308] Park JY, Baek MJ, Choi ES, et al. Paramagnetic ultrasmall gadolinium oxide nanoparticles as advanced T1 MRI contrast agent: account for large longitudinal relaxivity, optimal particle diameter, and *in vivo* T1 MR images. ACS Nano 2009;3:3663–9.
[309] Bridot J-L, Faure A-C, Laurent S, et al. Hybrid gadolinium oxide nanoparticles: multimodal contrast agents for *in vivo* imaging. J Am Chem Soc 2007;129:5076–84.
[310] Marc-André F, Rodrigo MP Jr, Fredrik S, et al. Polyethylene glycol-covered ultra-small Gd_2O_3 nanoparticles for positive contrast at 1.5 T magnetic resonance clinical scanning. Nanotechnology 2007;18:395501.
[311] Li Y, Chen T, Tan W, Talham DR. Size-dependent mri relaxivity and dual imaging with $Eu_{0.2}Gd_{0.8}PO_4 \cdot H_2O$ nanoparticles. Langmuir 2014;30:5873–9.
[312] Hou Y, Qiao R, Fang F, et al. $NaGdF_4$ nanoparticle-based molecular probes for magnetic resonance imaging of intraperitoneal tumor xenografts *in vivo*. ACS Nano 2013;7:330–8.
[313] Yi Z, Li X, Lu W, Liu H, Zeng S, Hao J. Hybrid lanthanide nanoparticles as a new class of binary contrast agents for *in vivo* T1/T2 dual-weighted MRI and synergistic tumor diagnosis. J Mater Chem B 2016;4:2715–22.
[314] Blasiak B, Volotovskyy V, Deng C, Foniok T, Tomanek B. A comparison of MR imaging of a mouse model of glioma at 0.2 T and 9.4 T. J Neurosci Methods 2012;204:118–23.
[315] Duyn JH, van Gelderen P, Li T-Q, de Zwart JA, Koretsky AP, Fukunaga M. High-field MRI of brain cortical substructure based on signal phase. Proc Natl Acad Sci 2007;104:11796–801.
[316] Zhang X, Blasiak B, Marenco AJ, Trudel S, Tomanek B, van Veggel FCJM. Design and regulation of $NaHoF_4$ and $NaDyF_4$ nanoparticles for high-field magnetic resonance imaging. Chem Mat 2016;28:3060–72.
[317] Liu Y, Ai K, Lu L. Nanoparticulate X-ray computed tomography contrast agents: from design validation to *in vivo* applications. Acc Chem Res 2012;45:1817–27.
[318] Zhai X, Lei P, Zhang P, et al. Growth of lanthanide-doped $LiGdF_4$ nanoparticles induced by $LiLuF_4$ core as tri-modal imaging bioprobes. Biomaterials 2015;65:115–23.
[319] Rao L, Lu W, Zeng T, et al. Sub-10 nm $BaLaF_5$:Mn/Yb/Er nanoprobes for dual-modal synergistic *in vivo* upconversion luminescence and X-ray bioimaging. J Mater Chem B 2014;2:6527–33.
[320] Xia A, Zhang X, Zhang J, et al. Enhanced dual contrast agent, Co^{2+}-doped NaYF4:Yb^{3+}, Tm^{3+} nanorods, for near infrared-to-near infrared upconversion luminescence and magnetic resonance imaging. Biomaterials 2014;35:9167–76.
[321] Ma D, Meng L, Chen Y, et al. $NaGdF_4$:Yb^{3+}/Er^{3+}@$NaGdF_4$:Nd^{3+}@sodium-gluconate: multifunctional and biocompatible ultrasmall core–shell nanohybrids for UCL/MR/CT multimodal imaging. ACS Appl Mater Interfaces 2015;7:16257–65.
[322] Zhang P, He Y, Liu J, et al. Core-shell $BaYbF_5$:Tm@$BaGdF_5$:Yb, Tm nanocrystals for *in vivo* trimodal UCL/CT/MR imaging. RSC Adv 2016;6:14283–9.
[323] Sun Y, Zhu X, Peng J, Li F. Core–shell lanthanide upconversion nanophosphors as four-modal probes for tumor angiogenesis imaging. ACS Nano 2013;7:11290–300.
[324] Li Q, Wang C, Tan H, Tang G, Gao J, Chen C-H. A turn on fluorescent sensor based on lanthanide coordination polymer nanoparticles for the detection of mercury(II) in biological fluids. RSC Adv 2016;6:17811–7.

[325] Rocha J, Carlos LD, Paz FAA, Ananias D. Luminescent multifunctional lanthanides-based metal-organic frameworks. Chem Soc Rev 2011;40:926–40.
[326] Tang Q, Liu S, Liu Y, et al. Cation sensing by a luminescent metal–organic framework with multiple Lewis basic sites. Inorg Chem 2013;52:2799–801.
[327] Guo S, Xie X, Huang L, Huang W. Sensitive water probing through nonlinear photon upconversion of lanthanide-doped nanoparticles. ACS Appl Mater Interfaces 2016;8:847–53.
[328] Brites CDS, Lima PP, Silva NJO, et al. Thermometry at the nanoscale. Nanoscale 2012;4:4799–829.
[329] Zheng S, Chen W, Tan D, et al. Lanthanide-doped $NaGdF_4$ core-shell nanoparticles for non-contact self-referencing temperature sensors. Nanoscale 2014;6:5675–9.
[330] Liu J, Liu Y, Liu Q, Li C, Sun L, Li F. Iridium(III) Complex-coated nanosystem for ratiometric upconversion luminescence bioimaging of cyanide anions. J Am Chem Soc 2011;133:15276–9.
[331] Chen H, Yuan F, Wang S, Xu J, Zhang Y, Wang L. Aptamer-based sensing for thrombin in red region via fluorescence resonant energy transfer between $NaYF_4$:Yb, Er upconversion nanoparticles and gold nanorods. Biosens Bioelectron 2013;48:19–25.
[332] Sedlmeier A, Achatz DE, Fischer LH, Gorris HH, Wolfbeis OS. Photon upconverting nanoparticles for luminescent sensing of temperature. Nanoscale 2012;4:7090–6.
[333] Vetrone F, Naccache R, Zamarrón A, et al. Temperature sensing using fluorescent nanothermometers. ACS Nano 2010;4:3254–8.
[334] Fischer LH, Harms GS, Wolfbeis OS. Upconverting nanoparticles for nanoscale thermometry. Angew Chem-Int Edit 2011;50:4546–51.
[335] Carrillo-Carrión C, Escudero A, Parak WJ. Optical sensing by integration of analyte-sensitive fluorophore to particles. Trends Anal Chem 2016;84:84–96.
[336] Kuningas K, Ukonaho T, Päkkilä H, et al. Upconversion fluorescence resonance energy transfer in a homogeneous immunoassay for estradiol. Anal Chem 2006;78:4690–6.
[337] Kumar M, Zhang P. Highly sensitive and selective label-free optical detection of mercuric ions using photon upconverting nanoparticles. Biosens Bioelectron 2010;25:2431–5.
[338] Wu S, Duan N, Ma X, et al. Multiplexed fluorescence resonance energy transfer aptasensor between upconversion nanoparticles and graphene oxide for the simultaneous determination of mycotoxins. Anal Chem 2012;84:6263–70.
[339] Liu C, Wang Z, Jia H, Li Z. Efficient fluorescence resonance energy transfer between upconversion nanophosphors and graphene oxide: a highly sensitive biosensing platform. Chem Commun 2011; 47:4661–3.
[340] Duan N, Wu S, Zhu C, et al. Dual-color upconversion fluorescence and aptamer-functionalized magnetic nanoparticles-based bioassay for the simultaneous detection of *Salmonella typhimurium* and *Staphylococcus aureus*. Anal Chim Acta 2012;723:1–6.
[341] Saleh SM, Ali R, Hirsch T, Wolfbeis OS. Detection of biotin–avidin affinity binding by exploiting a self-referenced system composed of upconverting luminescent nanoparticles and gold nanoparticles. J Nanopart Res 2011;13:4603–11.
[342] Wang Y, Shen P, Li C, Wang Y, Liu Z. Upconversion fluorescence resonance energy transfer based biosensor for ultrasensitive detection of matrix metalloproteinase-2 in blood. Anal Chem 2012;84:1466–73.
[343] Cardoso Dos Santos M, Hildebrandt N. Recent developments in lanthanide-to-quantum dot FRET using time-gated fluorescence detection and photon upconversion. Trends Anal Chem 2016:84(Part A):60–71.
[344] Tu D, Liu L, Ju Q, et al. Time-resolved FRET biosensor based on amine-functionalized lanthanide-doped $NaYF_4$ nanocrystals. Angew Chem-Int Edit 2011;50:6306–10.
[345] Geißler D, Linden S, Liermann K, Wegner KD, Charbonnière LJ, Hildebrandt N. Lanthanides and quantum dots as Förster resonance energy transfer agents for diagnostics and cellular imaging. Inorg Chem 2014;53:1824–38.
[346] Kuningas K, Rantanen T, Karhunen U, Lövgren T, Soukka T. Simultaneous use of time-resolved fluorescence and anti-Stokes photoluminescence in a bioaffinity assay. Anal Chem 2005;77:2826–34.
[347] Zhang C, Yuan Y, Zhang S, Wang Y, Liu Z. Biosensing platform based on fluorescence resonance energy transfer from upconverting nanocrystals to graphene oxide. Angew Chem-Int Edit 2011;50:6851–4.
[348] Alonso-Cristobal P, Vilela P, El-Sagheer A, et al. Highly sensitive DNA sensor based on upconversion nanoparticles and graphene oxide. ACS Appl Mater Interfaces 2015;7:12422–9.
[349] Xu S, Xu S, Zhu Y, et al. A novel upconversion, fluorescence resonance energy transfer biosensor (FRET) for sensitive detection of lead ions in human serum. Nanoscale 2014;6:12573–9.
[350] Mattsson L, Wegner KD, Hildebrandt N, Soukka T. Upconverting nanoparticle to quantum dot FRET for homogeneous double-nano biosensors. RSC Adv 2015;5:13270–7.
[351] Rantanen T, Järvenpää M-L, Vuojola J, Kuningas K, Soukka T. Fluorescence-quenching-based enzyme-activity assay by using photon upconversion. Angew Chem-Int Edit 2008;47:3811–3.
[352] Wang M, Hou W, Mi C-C, et al. Immunoassay of goat antihuman immunoglobulin g antibody based on luminescence resonance energy transfer between near-infrared responsive $NaYF_4$:Yb, Er upconversion fluorescent nanoparticles and gold nanoparticles. Anal Chem 2009;81:8783–9.
[353] Long Q, Li H, Zhang Y, Yao S. Upconversion nanoparticle-based fluorescence resonance energy transfer assay for organophosphorus pesticides. Biosens Bioelectron 2015;68:168–74.
[354] Ye WW, Tsang M-K, Liu X, Yang M, Hao J. Upconversion luminescence resonance energy transfer (LRET)-based biosensor for rapid and ultrasensitive detection of avian influenza virus H7 subtype. Small 2014;10:2390–7.
[355] Ai FJ, Ju Q, Zhang XM, Chen X, Wang F, Zhu GY. A core-shell-shell nanoplatform upconverting near-infrared light at 808 nm for luminescence imaging and photodynamic therapy of cancer. Sci Rep 2015;5:10785.
[356] Sy M, Nonat A, Hildebrandt N, Charbonniere LJ. Lanthanide-based luminescence biolabelling. Chem Commun 2016;52:5080–95.
[357] Cywiński PJ, Hammann T, Hühn D, Parak WJ, Hildebrandt N, Löhmannsröben H-G. Europium-quantum dot nanobioconjugates as luminescent probes for time-gated biosensing. J Biomed Opt 2014;19:101506.
[358] Cywinski PJ, Nchimi Nono K, Charbonniere LJ, Hammann T, Lohmannsroben H-G. Photophysical evaluation of a

new functional terbium complex in FRET-based time-resolved homogenous fluoroassays. Phys Chem Chem Phys 2014;16:6060–7.
[359] Tagit O, Annio G, Hildebrandt N. Terbium to quantum rod Förster resonance energy transfer for homogeneous bioassays with picomolar detection limits. Microchimica Acta 2015;182:1693–700.
[360] Bhuckory S, Lefebvre O, Qiu X, Wegner K, Hildebrandt N. Evaluating quantum dot performance in homogeneous FRET immunoassays for prostate specific antigen. Sensors 2016;16:197.
[361] Pihlasalo S, Mariani L, Harma H. Quantitative and discriminative analysis of nucleic acid samples using luminometric non-specific nanoparticle methods. Nanoscale 2016;8:5902–11.
[362] Hildebrandt N, Wegner KD, Algar WR. Luminescent terbium complexes: superior Förster resonance energy transfer donors for flexible and sensitive multiplexed biosensing. Coord Chem Rev 2014;273–274:125–38.
[363] Tong-Ochoa N, Kopra K, Syrjänpää M, Legrand N, Härmä H. Homogeneous single-label tyrosine kinase activity assay for high throughput screening. Anal Chim Acta 2015;897:96–101.
[364] Kopra K, Härmä H. Quenching resonance energy transfer (QRET): a single-label technique for inhibitor screening and interaction studies. N Biotechnol 2015;32:575–80.
[365] Zhou X, Li H, Xiao H, et al. A microporous luminescent europium metal-organic framework for nitro explosive sensing. Dalton Trans 2013;42:5718–23.
[366] Li Y, Zhang S, Song D. A luminescent metal–organic framework as a turn-on sensor for DMF vapor. Angew Chem-Int Edit 2013;52:710–3.
[367] Weber IT, Terra IAA, Melo AJGd, et al. Up-conversion properties of lanthanide-organic frameworks and how to track ammunitions using these materials. RSC Adv 2012;2:3083–7.
[368] Liu Z, He W, Guo Z. Metal coordination in photoluminescent sensing. Chem Soc Rev 2013;42:1568–600.